

**OPTICAL PROPERTIES OF
COMPOUNDS AND
DISORDERED ALLOYS**

**THESIS SUBMITTED FOR THE DEGREE OF
DOCTOR OF PHILOSOPHY (SCIENCE)
OF THE
UNIVERSITY OF JADAVPUR**

**KAMAL KRISHNA SAHA
SATYENDRANATH BOSE NATIONAL CENTRE
FOR BASIC SCIENCES
JD BLOCK, SECTOR 3, SALT LAKE CITY
KOLKATA 700 098, INDIA**

DECEMBER, 2004

OPTICAL PROPERTIES OF COMPOUNDS AND DISORDERED ALLOYS

**THESIS SUBMITTED FOR THE DEGREE OF
DOCTOR OF PHILOSOPHY (SCIENCE)
OF THE
UNIVERSITY OF JADAVPUR**

**KAMAL KRISHNA SAHA
SATYENDRANATH BOSE NATIONAL CENTRE
FOR BASIC SCIENCES
JD BLOCK, SECTOR 3, SALT LAKE CITY
KOLKATA 700 098, INDIA**

DECEMBER, 2004

☎ : + 91 33 2335 5706 - 8 (Extn. 100)
FAX : + 91 33 2335 3477
e-mail : abhijit@bose.res.in



सत्येन्द्र नाथ बसु राष्ट्रीय मौलिक विज्ञान केन्द्र

SATYENDRA NATH BOSE NATIONAL CENTRE FOR BASIC SCIENCES

(An autonomous body under the Ministry of Science & Technology, Government of India)

BLOCK-JD, SECTOR III, Salt Lake, Kolkata-700 098

अभिजित मुखर्जी

अध्यापक एवं अधिष्ठाता (शैक्षणिक कार्यक्रम)

Abhijit Mookerjee

Professor & Dean (Academic Programmes)

CERTIFICATE FROM THE SUPERVISOR

This is to certify that the thesis entitled **Optical properties of compounds and disordered alloys** submitted by **Kamal Krishna Saha**, who got his name registered on **November 12, 2002** for the award of **Ph.D. (Science)** degree of **Jadavpur University**, is absolutely based upon his own work under the supervision of **Professor Abhijit Mookerjee** at **S. N. Bose National Centre For Basic Sciences, Kolkata, India** and that neither this thesis nor any part of it has been submitted for any degree/diploma or any other academic award anywhere before.

ABHIJIT MOOKERJEE

Senior Professor,

Dean (Academic Programme),

Satyendranath Bose National Centre For Basic Sciences,

JD Block, Sector 3, Salt Lake City, Kolkata 700 098

India

Date : **27. 12. 2004**

Acknowledgments

I am very happy to take this opportunity to express my gratitude to my supervisor Professor Abhijit Mookerjee for introducing and inspiring me to the fascinating field of physics of disordered materials. His constant guidance and encouragement made this work possible.

I am grateful to Dr. Tanusri Saha-Dasgupta for her active collaboration and continued interest in a significant portion of my research work.

I would like to thank Professors O. K. Andersen and Ove Jepsen for their kind help in making the development of generalized k-space integration for random alloys and their kind hospitality during my visit to the Max-Planck Institute, Stuttgart. I would like to acknowledge the use of the Stuttgart TB-LMTO and NMTO packages in this work.

I would like to thank the Department of Science and Technology, Government of India for the research fellowship thus enabling me to pursue my Ph.D. work in India. I would also like to thank Professor S. Dattagupta, Director, S. N. Bose National Centre for Basic Sciences, Kolkata, India for providing me with an opportunity to work at the centre. I am grateful to Dr. Surajit Sengupta for allowing me to work in his Beowulf Cluster system.

I am thankful to my colleagues Mr. Atisdipankar Chakrabarti and Mr. Monodeep Chakraborty for their help and discussions throughout of my research period. My heartiest thanks goes to my friends at the S. N. Bose National Centre for Basic Sciences for making my stay in Kolkata enjoyable. I wish to thank staff members of this centre for their cooperation and help.

My sincere thank goes to IIT, Kanpur, India, International Centre for Theoretical Physics, Italy, Department of Physics, Dhaka University, Bangladesh, and the National Institute of Advanced Industrial Science and Technology (AIST), Japan, for inviting me to present talks, attend schools and conferences hosted by them.

This acknowledgment cannot end without mentioning the constant support from my parents, brothers and sisters.

List of Publications

- 1. Optical properties of perovskite alkaline-earth titanates : A formulation**
Kamal Krishna Saha, Tanusri Saha-Dasgupta, Abhijit Mookerjee, Sonali Saha and T P Sinha
J. Phys.: Condens. Matter **14** (2002) 3849-3863.
- 2. Symmetry reduction in the augmented space recursion formalism for random binary alloys**
Kamal Krishna Saha, Tanusri Saha-Dasgupta, Abhijit Mookerjee and Indra Dasgupta
J. Phys.: Condens. Matter **16** (2004) 1409-1423.
- 3. Electronic and optical properties of ZnIn_2Te_4**
Biplab Ganguli, Kamal Krishna Saha, Tanusri Saha-Dasgupta, Abhijit Mookerjee and A K Bhattacharya
Physica B **348** (2004) 382-390.
- 4. Optical properties of random alloys : A formulation**
Kamal Krishna Saha and Abhijit Mookerjee
Phys. Rev. B **70** (2004) 134205.
- 5. Electronic structure of random binary alloys : an augmented space formulation in reciprocal space**
Kamal Krishna Saha, Abhijit Mookerjee and Ove Jepsen
Phys. Rev. B (2004) (Accepted for publication) ; cond-mat/0405175.
- 6. Electronic structure and response functions in random alloys : an application of block recursion and Green matrices**
Kamal Krishna Saha and Abhijit Mookerjee
J. Phys.: Condens. Matter (2004) (Accepted for publication); cond-mat/0409387.
- 7. Optical properties of random alloys : Application to $\text{Cu}_{50}\text{Au}_{50}$ and $\text{Ni}_{50}\text{Pt}_{50}$**
Kamal Krishna Saha and Abhijit Mookerjee
Phys. Rev. Lett. (2004) (Communicated); cond-mat/0411251.

Contents

1	Overview of electronic structure calculations	1
1.1	Introduction	1
1.2	Linear muffin-tin orbitals method	5
1.2.1	The muffin-tin potential and partial wave solutions	5
1.2.2	Muffin-tin orbitals and tail cancellation	7
1.2.3	Linearization of energy	10
1.3	Beyond linear methods : NMTO	11
1.4	The recursion method	12
1.4.1	Density of states	15
1.4.2	Projected or local density of states	16
1.4.3	Terminating Schemes	17
1.5	Random alloys : Configuration averaging	19
1.6	The augmented space formalism (ASF)	21
1.6.1	The augmented space theorem	23
2	The Augmented space recursion	25
2.1	Augmented space recursion (ASR)	25
2.1.1	The TB-LMTO Hamiltonian for random binary alloys	25
2.1.2	Configuration-averaged Green function	26
2.2	Symmetry reduction of the augmented space rank	28
2.3	Conclusions	40
3	Augmented space recursion in reciprocal space	41
3.1	Introduction	41
3.2	Augmented space recursion in k-space	43
3.3	Spectral density and fuzzy bands	47
3.4	Generalized tetrahedron method integration in k-space	47
3.5	Computational details and results	49
3.6	Parallelization of codes	55

3.7	Conclusion	58
4	Block recursion and Green matrices	59
4.1	Block recursion	59
4.2	Model calculations	64
4.3	Conclusion	68
5	Optical properties of ordered compounds	69
5.1	Introduction	69
5.2	Methodology	70
5.3	Application to perovskite alkaline-earth titanates	77
5.3.1	Electronic structure calculations	78
5.3.2	Optical properties	82
5.4	Application to the defect-chalcopyrite ZnIn_2Te_4	87
5.4.1	Electronic structure calculations	90
5.4.2	Optical properties	93
5.5	Conclusions	96
6	Optical properties of disordered alloys	98
6.1	Introduction	98
6.2	The optical conductivity	99
6.3	Configuration averaging	100
6.4	Averaged Green function in the pseudo-fermion formalism	103
6.5	Averaged optical conductivity in the pseudo-fermion formalism	107
6.5.1	Disorder-induced renormalization of the current terms	107
6.5.2	Corrections to the current term related to the vertex corrections . .	113
6.5.3	The vertex correction	116
6.5.4	Comments and remarks	118
6.6	Applications to CuAu (50-50) and NiPt (50-50) alloys	119
6.7	Conclusion	124
7	An assessment and future plans	126

7.1	Concluding remarks	126
7.2	Future directions	128
7.2.1	Remarks	130

List of Figures

1.1	Comparison between a full- and a muffin-tin potential.	6
1.2	Construction of muffin-tin orbitals.	8
1.3	Three MTOs centered at R , R' and R'' . The tails of the central MTO lie on the other spheres and its head lies in its personal sphere. The MTOs are shown schematically only by their envelope. The tail cancellation theorem also illustrated here.	9
1.4	Transformation to the chain.	14
2.1	Nearest neighbour shells around a central site on a square lattice. The colour coding indicates the symmetry weight of the sites : white represents sites with weight 1, gray with weight 4 and black with weight 8.	30
2.2	sp -orbitals on a cubic lattice. Only projections on the xy plane are shown. The positive parts of the lobes are unshaded, while the negative parts of the lobes are shaded. The values of the symmetry factor for the overlaps ($\beta_{LL'}(\ell m)$, defined in the text) are shown for each direction. The numbering of sites on the cubic lattice is shown in the inset at the bottom right. . . .	31
2.3	Overlaps involving d orbitals in the e_g and t_{2g} symmetries. Only projections in the xy plane are shown. The positive parts of the lobes are unshaded, while the negative parts of the lobes are shaded.	32
2.4	Equivalent configurations on a cubic lattice. Configurations labelled by \uparrow are shown as light spheres, while those labeled by \downarrow are shown as dark spheres. The top twelve configurations are equivalent, while the bottom three are equivalent. The lower right inset shows the numbering scheme used for the lattice sites in the main text.	35
2.5	Convergence of the errors in energy moments of $Ag_{50}Pd_{50}$ as functions of the recursion step.	37

2.6	Showing how the number of lattice sites increase with increasing the number of shells in the real-space map and its reduced version. This is for an ordered fcc lattice.	38
2.7	Showing how the number of lattice sites increase with increasing the number of shells in an augmented space map on a disordered binary alloy on a fcc lattice.	39
2.8	CPU time taken per recursion step for a $\text{Ag}_{50}\text{Pd}_{50}$ disordered binary alloy on a fcc lattice in a spd TB-LMTO minimal basis set. The times with and without symmetry reduction are shown.	40
3.1	Showing how the number of lattice sites increase with increasing the number of shells in the real-space and reciprocal-space map.	50
3.2	Comparison of the average (50-50) density of states for a model fcc alloy calculated using \mathbf{k} -space formulation of ASR (solid curve) and using real-space formulation of ASR (dotted curve). \mathbf{k} -space integration has been performed in two ways : (a) using Tetrahedron Method (right solid curve) (b) multiplying spectral function $A_k(E)$ by k -point weight and then summing up over k (left solid curve). In both figures we note that the oscillations shown by the brute force technique is smoothened by the TM.	51
3.3	The spectral function of $\text{Ni}_{50}\text{Pt}_{50}$ alloy plotted as a function of energy at several \mathbf{k} -points along the $\Gamma - X$ direction.	52
3.4	(Right) Ni (dashed lines) and Pt (bold lines) energy bands on a lattice appropriate to the $\text{Ni}_{50}\text{Pt}_{50}$ alloy, in the $\Gamma - X$ direction. Average lattice parameter $a_0 = 7.127au$ was fixed after minimizing the energy. (Left) The fuzzy band of the disordered $\text{Ni}_{50}\text{Pt}_{50}$ system plotted along the same direction.	53
3.5	Comparison of the partial density of states of $\text{Ni}_{50}\text{Pt}_{50}$ alloy calculated using augmented space recursion in (a) real-space formulation (left panel). (b) \mathbf{k} -space formulation (right panel).	54
3.6	Comparison of the density of states of the $\text{Ni}_{50}\text{Pt}_{50}$ alloy calculated using augmented space recursion in (a) \mathbf{k} -space formulation. (b) real-space formulation. (c) Density of states of Ni (solid line) and Pt (dotted line) on a lattice appropriate to the $\text{Ni}_{50}\text{Pt}_{50}$ alloy. (d) Valence-band photo-emission spectra of $\text{Ni}_{50}\text{Pt}_{50}$ with photon energy $h\nu = 60$ (Nahm <i>et al</i> 1996).	55
3.7	Flowchart of the augmented space recursion method (left) and schematic flowchart for parallelization of the same code (right).	57

4.1	Systematic discrete numbering of the nearest-neighbour map on a square lattice.	61
4.2	The real and imaginary parts of the Green matrix for a 2×2 Hamiltonian model. The full lines refer to \mathbf{G}_{11} , the dashed-dotted line to \mathbf{G}_{22} and dashed lines to \mathbf{G}_{12}	65
4.3	The real and imaginary parts of the Green matrix for the s-d model on a fcc lattice. The calculations were done by a real-space block recursion. The full lines refer to \mathbf{G}_{11} , the dashed-dotted line to \mathbf{G}_{22} and dashed lines to \mathbf{G}_{12}	66
4.4	The matrix elements of $\mathbf{G}(\mathbf{k}, E)$ on a fcc lattice : the 11 element (left), the 22 element (middle), and the 12 element (right) along the Γ to X direction.	67
4.5	The real and imaginary parts of the Green matrix for the s-d model on a fcc lattice. The calculations are done by a k-space block recursion followed by a reciprocal-space integration (Saha <i>et al</i> 2004). The full lines refer to \mathbf{G}_{11} , the dashed-dotted line to \mathbf{G}_{22} and dashed lines to \mathbf{G}_{12}	68
5.1	(a) Cubic unit cell for a perovskite ABC_3 . (b) The Brilluoin zone for the cubic phase.	78
5.2	Band structures of CaTiO_3 , SrTiO_3 and BaTiO_3 (No scissors operation has been carried out in these calculations).	79
5.3	Densities of states for the three perovskite titanates.	81
5.4	Transition rates for the three perovskite titanates shown as functions of initial energies and incident photon energies.	83
5.5	Comparison of the calculated imaginary part of the dielectric function (ϵ_2) (left), for the three perovskite titanates, with the same function calculated considering transition rate is constant (right).	84
5.6	Comparison of calculated and experimental real parts $\epsilon_1(\omega)$ (top) and imaginary parts $\epsilon_2(\omega)$ (bottom) of dielectric function of CaTiO_3 as a function of photon energy: dotted curve is experimental (Ueda <i>et al</i> 1998, 1999); the continuous curve is theoretical.	85
5.7	Comparison of calculated and experimental real parts $\epsilon_1(\omega)$ (top) and imaginary parts $\epsilon_2(\omega)$ (bottom) of dielectric function of SrTiO_3 as a function of photon energy: dotted curve is experimental (Bäuerle <i>et al</i> 1978); the continuous curve is theoretical.	86

5.8	Comparison of calculated and experimental real parts $\epsilon_1(\omega)$ (top) and imaginary parts $\epsilon_2(\omega)$ (bottom) of dielectric function of BaTiO_3 as a function of photon energy: dotted curve is experimental (Bäuerle <i>et al</i> 1978); the continuous curve is theoretical.	87
5.9	Crystal structure of defect-chalcopyrite-type semiconductor ZnIn_2Te_4 . We show the orthorhombic primitive cell with two molecules per cell.	88
5.10	The band structure of ZnIn_2Te_4 calculated from the TB-LMTO (left) and the NMTO (right) with three nodal energies across the energy range.	92
5.11	Density of states for ZnIn_2Te_4 (left) calculated from the TB-LMTO and (right) calculated from NMTO.	93
5.12	(a) Theoretical density of states $N(E)$ and (b) experimental XPS spectrum $I(E)$ taken from Ref. Ozaki and Adachi 2001.	94
5.13	(Top) imaginary part (averaged over all photon polarizations) of the dielectric function of ZnIn_2Te_4 from an LMTO calculation, (Right panel) real and imaginary parts of dielectric function based on NMTO calculation, and (Left panel) the experimental results of Ozaki and Adachi 2001. Photon energy is shown in the unit of eV.	95
5.14	The imaginary parts of the dielectric function with incident photon polarizations perpendicular and parallel to the c-axis. Photon energy is shown in the unit of eV.	96
6.1	The scattering diagrams for (a) the two topologically identical diagrams for $n = 2$ and (b) one of the $3!$ topologically identical diagrams for $n = 3$	104
6.2	The topologically distinct scattering diagrams for $n = 4$. Top and middle are nonseparable, the bottom is separable. The middle diagram is a skeleton one.	105
6.3	Skeleton diagrams for order $n = 5$	106
6.4	The skeleton diagrams for the self-energy $\Sigma(z)$	107
6.5	The scattering vertices associated with the random current terms.	108
6.6	The construction of scattering diagrams for $S_\gamma(z_1, z_2)$	109
6.7	The diagram for $[\ll j \gg \ll \mathbf{G}^v \gg \ll j \gg \ll \mathbf{G}^c \gg]$	110
6.8	Relation between the renormalized currents and the self-energy.	111
6.9	Few more renormalized currents.	112

6.10	The scattering diagrams associated with joint fluctuations of the random current terms and one propagator.	113
6.11	Renormalized currents (left column) derived from vertex corrections (right column).	114
6.12	Some of the scattering diagrams associated with joint fluctuations of the random current terms and two propagators.	115
6.13	The scattering diagrams leading to vertex corrections.	117
6.14	The ladder scattering diagrams for the vertex correction in real-space and reciprocal-space representations.	118
6.15	The configuration-averaged joint density of states and correlation function for CuAu (50-50) alloy shown as a function of the photon energy.	121
6.16	Averaged optical conductivity, $\sigma_0(\omega) = S^{(0)}/\omega$, and the density of states for a CuAu (50-50) alloy (left). The corrections to the optical conductivity have been considered as discussed in section 6.5. Same curve with the Drude fit at low photon energies (right).	122
6.17	Interband contribution to the imaginary part of the dielectric function for CuAu (50-50) alloy.	123
6.18	The configuration-averaged joint density of states and correlation function for NiPt (50-50) alloy shown as a function of photon energy.	123
6.19	Averaged optical conductivity and the density of states for NiPt (50-50) alloy.	124
6.20	Interband contribution to the imaginary part of the dielectric function for NiPt (50-50) alloy.	125

List of Tables

2.1	Table showing the Slater-Koster parameters and the consequent symmetry factors $\beta_{LL'}^{lmn}$. The parameters for which the zero condition have been omitted can be obtained from the last column by permuting the direction cosines.	34
2.2	Comparison between system size and CPU time (in seconds) taken for recursion on a P4/256 machine for a full fcc lattice and the reduced lattice in real-space. The model system consists of s-states with nearest-neighbour hopping integrals and the Hamiltonian for Ag is taken from a TB-LMTO calculation with a minimal spd basis.	38
2.3	Comparison between system size and time (in seconds) taken for recursion (using 15 seed points for $\text{Ag}_{50}\text{Pd}_{50}$) on a P4/256 machine for a full fcc lattice and the reduced lattice in augmented space. The model is that of an alloy whose constituents have only s states and the Hamiltonian for $\text{Ag}_{50}\text{Pd}_{50}$ is taken from a TB-LMTO minimal spd basis for each constituent.	39
4.1	Parameters for our calculation for $\text{A}_{50}\text{B}_{50}$ alloy on a fcc lattice.	66
5.1	Electronic configurations of the alkaline-earth atoms.	79
5.2	The minimal basis sets used in the lower and upper energy panels.	80
5.3	Positions within the unit cell of atomic basis, including the empty spheres to take into account the vacancies within the structure.	90
6.1	Lowest energy and Vegard's Law lattice constants for CuAu and NiPt.	120

Chapter 1

Overview of electronic structure calculations

1.1 Introduction

One of the most powerful tools for studying the properties of solids is the measurement and analysis of their optical properties. These provide much useful information about the electronic energy band structure through the optical response of the mobile electrons to an external oscillating electronic field. The aim of this thesis is to study the electronic band structure as well as optical response of solids. The optical response of the solid material is characterized by the complex refractive index ($n = n_1 - in_2$), which may be expressed in terms of two optical constants, namely, the dielectric constant $n^2 = \epsilon = \epsilon_1 - i\epsilon_2$ and the optical absorption coefficient $\alpha = \omega\epsilon_2/n_1c$ (or the optical conductivity $\sigma = \omega\epsilon_2/4\pi$). An experimentalist measures some observable, such as reflectivity, transmission, absorption, ellipsometry or light scattering; from these experimental quantities we deduce the dielectric function $\epsilon(\omega)$ or the optical conductivity $\sigma(\omega)$ to compare with our theoretical results. These quantities are frequency-dependent complex functions and are directly related to the energy band structure of solids.

There is already an immense literature dedicated to light-solid state interactions, or in other words, the effect of the electromagnetic field on the electronic states of the solids, due to its major role in understanding the physics and properties of the solid state. This literature is continuously growing and flourishing, due also to the paramount importance of solid state devices in the development of any conceivable area of technology. However, this literature is mainly written emphasizing a certain type of materials (metals, semiconductors, ferroelectric materials, etc.) and also a certain type of optical experimental

methods on both compounds and alloys. But if we look at the theoretical studies, we hardly find much literature on dielectric response of random alloys. The object of this thesis is to develop a formulation to study optical response of compounds and disordered alloys.

Throughout our study we shall be dealing with the direct transitions only. So there is no phonon involved in our calculations. The simplest theory of the response of a solid to an oscillating external electromagnetic field is provided by the Drude model. The basic assumption is that the optical conductivity and the dielectric constant can be determined by considering the motion of free electrons. The model is based on classical equations of motion of an electron in an optical electric field, and gives the simplest theory of the optical constants. This free electrons contributions are mostly found in the metallic systems. These systems have no band-gaps and for low photon energies the conductivity arises due to intraband transition between s-p states, which are free electron like and lead to a Drude type of behaviour. As the photon energy increases and becomes comparable to the energy gap for semiconductor or insulator, a new conduction process, called interband transition, can occur. In this process the photon is absorbed, an excited electronic state is formed and a hole is left behind. The intraband transition occurs mostly between the occupied d and the conduction states. The d-states are localized and the electrons are also no more free. So the basic theory for the optical conductivity for localized states are not so simple as free electrons.

Ordered alloys with translational symmetries in their potentials are relatively easier to study. Complexity arises when we encounter the description of disordered alloys. The optical properties change as we move from the domain of ordered to disordered alloys. The disorder in alloys may appear in various forms : topological, substitutional, positional and so on. In this work we shall be concerned only with the substitutional disorder. Such alloys have an underlying lattice but the sites are occupied by either of the constituent atoms randomly with varying degree of statistical correlations. As so specific arrangements of constituents can be assumed for the case of random alloys, we have to consider several realizations of the system and then carry out proper averaging over configurations to obtain meaningful physical quantities.

Our plan is to develop a complete mathematical scheme which will be applicable to

both compounds and random binary alloys to study optical properties. In our development we shall emphasize the computational feasibility of the scheme. To improve the accuracy of the calculation and also to accelerate the computation, we shall carry out symmetry reduction in our formulation and finally write parallel programs compatible to a cluster machine.

Next few sections of this chapter reviews the some of the basic methodologies required for electronic band structure calculations. We shall base our calculations on the tight-binding linear muffin-tin orbitals (TB-LMTO) method. We describe how the improved version of the LMTO method, namely order-N muffin-tin orbitals (NMTO) basis, provides a more consistent formalism, treats the interstitial region accurately, and goes beyond the linear approximation. We also review the recursion method by which elements of the Green function associated with the Hamiltonian are obtained by transforming the Hamiltonian in a tridiagonal form. Finally, we introduce the augmented space formalism (ASF) to deal with the configuration averaging of a random binary alloys.

Chapter 2 is basically the continuation of the previous chapter for development of methodologies. In this chapter we shall describe the diagonal formalism of the augmented space recursion (ASR) within the framework of TB-LMTO method. We find that the main difficulty in the implementation of recursion on the augmented space is its enormous rank. So we present an efficient method which systematically reduces the rank of the augmented space and thereby helps to implement augmented space recursion for any real calculation. The method is based on the symmetry of the Hamiltonian in the augmented space and keeping recursion basis vectors in the irreducible subspace of the Hilbert space.

Chapter 3 presents a reciprocal-space formulation of the ASR which uses the lattice translation symmetry in the full augmented space to produce configuration-averaged quantities, such as spectral functions and complex band structures. Since the real-space part is taken into account *exactly* and there is no truncation of this in the recursion, the results are more accurate than recursions in real-space. We shall also describe the Brillouin zone integration procedure to obtain the configuration-averaged density of states. In order to carry out a calculation on a real alloy system, a serial program requires a very long time. We have, therefore, parallelized our codes, leading to faster computation. We apply the technique to $\text{Ni}_{50}\text{Pt}_{50}$ alloy in conjunction with the TB-LMTO basis. These de-

velopments in the theoretical basis is required for our future application to obtain optical conductivity in random systems.

Chapter 4 is dedicated to the generalization of the recursion method of Haydock *et al* 1972 for the calculation of Green matrices (in angular momentum space). Earlier approaches concentrated on the diagonal elements, since the focus was on spectral densities. However, calculations of configuration-averaged response functions or neutron scattering cross-sections require the entire Green matrices and self-energy matrices obtained from them. So we shall generalize the recursion to block recursion and block tridiagonalized the Hamiltonian.

Chapter 5 is focused on deriving a modified expression of the optical conductivity applicable to any solids. In ordered solids electronic states are labelled by the band index j and reciprocal vector \mathbf{k} . Since we eventually want to apply to disordered systems, where the bands are not sharp and electronic states are labelled by energy E and angular momentum L , we recast the Kubo formula as a product between energy-frequency dependent transition matrix and the energy resolved joint density of states (JDOS). Our main motivation is to generalize it to disordered systems, where the traditional reciprocal-space formulation breaks down due to the failure of Bloch's theorem. We shall work within the TB-LMTO minimal basis set and apply the new formula to the three alkaline-earth perovskite titanates in their paraelectric phases. To improve the results in the higher region of frequency we have used the NMTO basis and applied this to ZnIn_2Te_4 .

Chapter 6 presents a formulation for the calculation of the configuration-averaged optical conductivity in random alloys. The formulation is based on the augmented space theorem introduced by Mookerjee 1973. We show that disorder scattering renormalizes the electron and hole propagators as well as the transition amplitude. The corrections to the transition amplitude have been shown to be related to the self-energy of the propagators and vertex corrections. We shall combine our formulation with the TB-LMTO technique to study the optical conductivities of two alloys $\text{Cu}_{50}\text{Au}_{50}$ and $\text{Ni}_{50}\text{Pt}_{50}$.

Chapter 7 is an evaluation of our work. We shall describe our achievements, its limitations and try to prescribe how to overcome or minimize these limitations. We shall also give a brief description of our future plan of work, and finally concluding remarks.

1.2 Linear muffin-tin orbitals method

Muffin-tin orbitals (MTOs) form a basis of localized augmented orbitals introduced by Andersen 1971 and subsequently extended into an entire methodology. The goal of the approach is to provide a satisfying interpretation of the electronic structure of materials in terms of a *minimal basis* of orbitals. Like local orbital methods, the electronic states are described in a small number of meaningful orbitals; however, unlike those approaches the minimal basis can be accurate because the MTOs are generated from the Kohn-Sham Hamiltonian itself.

This section is devoted to the MTO approach, which sets the stage for the linearized LMTO extension that exhibits the real power of the approach.

1.2.1 The muffin-tin potential and partial wave solutions

The density functional theory (DFT), reduces the many-body Hamiltonian of the valence electron cloud in the presence of a ‘frozen’ array of ion-cores to an effective one-electron problem. The potential as seen by an electron within the LDA is :

$$V(\mathbf{r}) = \sum_{\mathbf{R}} v(\mathbf{r} - \mathbf{R})$$

where \mathbf{R} are the positions of the ion-cores and \mathbf{r} is the position of the electron. In the neighbourhood of an ion-core the potential seen by the electron in a solid is not very different from that in the atom whose ion-core we are focusing on. We shall define a radius s_R around \mathbf{R} within which we shall assume that the potential is spherically symmetric. These spheres will be called the *muffin-tin spheres*. In the *interstitial*, that is the rest of the space from which the muffin-tin spheres are carved out, the potential varies very slowly. We shall replace the potential in this region by a constant average. The resulting potential is called a *muffin-tin potential*. An illustration comparing a full potential with a muffin-tin one, is shown in figure 1.1.

Before we attempt to solve the full problem of an electron in a solid, let us first examine the problem of an electron in a single muffin-tin potential. This potential is given by :

$$v(\mathbf{r} - \mathbf{R}) = \begin{cases} v(r_R) & \text{for } r_R \leq s_R \\ -v_0 & \text{for } r_R > s_R \end{cases} \quad r_R = |\mathbf{r} - \mathbf{R}|$$

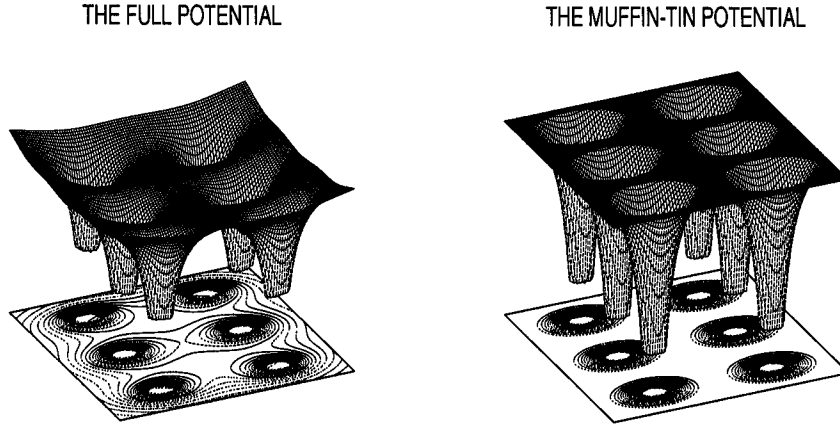


Figure 1.1: Comparison between a full- and a muffin-tin potential.

and the Schrödinger-like Kohn-Sham equation for the single electron, within the DFT, is given by :

$$\left[-\frac{\hbar^2}{2m} \nabla^2 + v(\mathbf{r} - \mathbf{R}) \right] \phi(\varepsilon, \mathbf{r} - \mathbf{R}) = \varepsilon \phi(\varepsilon, \mathbf{r} - \mathbf{R}).$$

We may immediately solve the above equation in the region $r_R \leq s_R$, in which the potential is spherically symmetric and

$$\phi(\mathbf{r} - \mathbf{R}) = \varphi_{RL}(\varepsilon, r_R) Y_L(\hat{r}_R) \quad (1.1)$$

Here L denotes the angular momentum labels (ℓ, m) , $Y_L(\hat{r})$ are the spherical harmonic functions and \hat{r}_R are the angular variables associated with the unit vector $(\mathbf{r} - \mathbf{R})/r_R$. $\varphi_{RL}(r_R, \varepsilon)$ are solutions of the radial equation :

$$\left[\frac{d^2}{dr_R^2} - v(r_R) + \frac{\ell(\ell+1)}{r_R^2} - \varepsilon \right] r_R \varphi_{RL}(\varepsilon, r_R) = 0. \quad (1.2)$$

This solution is regular at $\mathbf{r} = \mathbf{R}$ and behaves like r_R^ℓ as $r_R \rightarrow 0$. Outside the muffin-tin sphere the potential is a constant. Again the wave function factorizes as in equation (1.1). The solution of the radial equation with a constant $v(r_R) = -v_0$

$$\left[\frac{d^2}{dr_R^2} + \frac{\ell(\ell+1)}{r_R^2} - \kappa^2 \right] r_R \varphi_{RL}(\varepsilon, r_R) = 0.$$

are the spherical Bessel and Neumann functions and $\kappa^2 = \varepsilon - v_0$. Since $\mathbf{r} = \mathbf{R}$ is not included in this region, both the solutions are allowed and the full solution in this region

is the linear combination :

$$A_{R\ell}(\varepsilon, \kappa) j_{\ell}(\kappa r_R) + B_{R\ell}(\varepsilon, \kappa) n_{\ell}(\kappa r_R)$$

We now invoke the boundary condition that on the muffin-tin sphere both the wave function and its derivative are continuous. The potential function is given in terms of the scattering phase shift as :

$$\begin{aligned} P_{RL}^o(\varepsilon, \kappa) &= -\cot \eta_{R\ell}(\varepsilon, \kappa) \\ &= \frac{n_{\ell}(\kappa r_R) \left[D[n_{\ell}(\kappa r_R)] - D[\varphi_{RL}(\varepsilon, r_R)] \right]}{j_{\ell}(\kappa r_R) \left[D[j_{\ell}(\kappa r_R)] - D[\varphi_{RL}(\varepsilon, r_R)] \right]} \Bigg|_{r_R=s_R} \end{aligned} \quad (1.3)$$

where $D[f(r)]$ is the scaled logarithmic derivative of $f(r)$. It follows immediately from equations (1.2) and (1.3) that the potential functions or the phase shifts are dependent on the muffin-tin potential. The *partial wave* solution in all space is then :

$$\varphi_{RL}(\varepsilon, r_R) = \begin{cases} N_{RL}^o(\varepsilon, \kappa) \varphi_{RL}(\varepsilon, r_R) & \text{if } r_R \leq s_R \\ n_{\ell}(\kappa r_R) - P_{RL}^o(\varepsilon, \kappa) j_{\ell}(\kappa r_R) & \text{if } r_R > s_R \end{cases} \quad (1.4)$$

$N_{RL}^o(\varepsilon)$ is a normalization constant.

1.2.2 Muffin-tin orbitals and tail cancellation

The partial waves are not adequate as a basis for the following reason : we would like a basis to be such that its *head* contains all the information about the potential, while its *tail* contains information only about the constant potential outside the muffin-tin sphere. In addition, we would like the basis not to be a badly behaved function anywhere in space. A way of choosing such a basis is as follows :

$$\chi_{RL}(\varepsilon, r_R) = \begin{cases} N_{RL}^o(\varepsilon, \kappa) \varphi_{RL}(\varepsilon, r_R) + P_{RL}^o(\varepsilon, \kappa) j_{\ell}(\kappa r_R) & \text{if } r_R \leq s_R \\ n_{\ell}(\kappa r_R) & \text{if } r_R > s_R \end{cases} \quad (1.5)$$

The equation (1.3) ensures that the head and the tails of the above function match continuously and differentiably at the muffin-tin boundary at s_R . These functions are

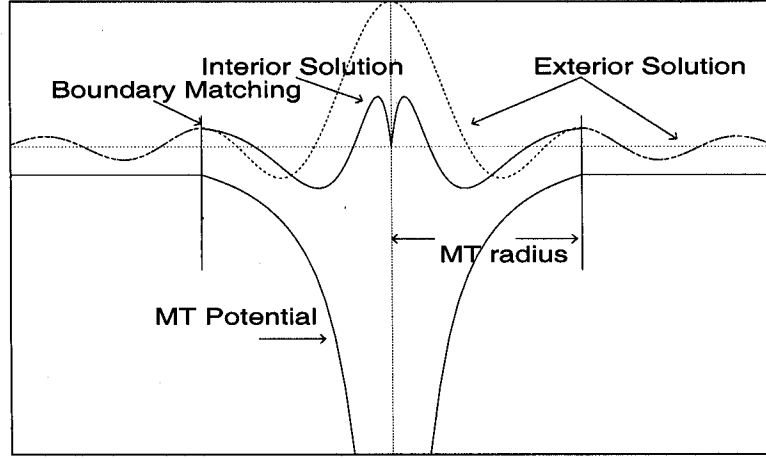


Figure 1.2: Construction of muffin-tin orbitals.

called *Muffin-tin Orbitals* (MTO) and qualify as suitable basis for representation of the wave function in the solid.

We can think about the construction of the muffin-tin orbital as follows : We start from the Neumann function $n_\ell(\kappa r_R)$ defined in all space. We now retain the part in its *tail* and replace the *head* by the function $N_{RL}^o(\varepsilon) \varphi_{RL}(\varepsilon, r_R) + P_{RL}^o(\varepsilon, \kappa) j_\ell(\kappa r_R)$ which joins smoothly and differentiably with the tail. This is illustrated in the figure 1.2.

So far we have been discussing the partial waves and muffin-tin orbitals associated with a single muffin-tin potential. Let us now introduce the wave function solution of the solid muffin-tin potential of the type shown in figure 1.1. We shall expand this wave function as a linear combination of the muffin-tin orbitals associated with individual muffin-tin potentials centered at different sites $\{\mathbf{R}\}$:

$$\Psi(\varepsilon, \mathbf{r}) = \sum_{\mathbf{R}} \sum_L c_{RL}(\varepsilon) \chi_{RL}(\varepsilon, \mathbf{r} - \mathbf{R}) \quad (1.6)$$

In what follows we shall also use the expression for the tail of the Neumann function $n_\ell(\kappa r_R)$ outside its *personal* sphere :

$$n_\ell(\kappa r_R) = - \sum_{L'} S_{RL, R'L'}^o(\kappa) j_{L'}(\kappa r_{R'}) \quad (1.7)$$

Here $S_{RL, R'L'}^o(\kappa)$ are the canonical structure constants which depend upon the relative position of \mathbf{R}' with respect to \mathbf{R} and have nothing to do with the ion-core potentials that

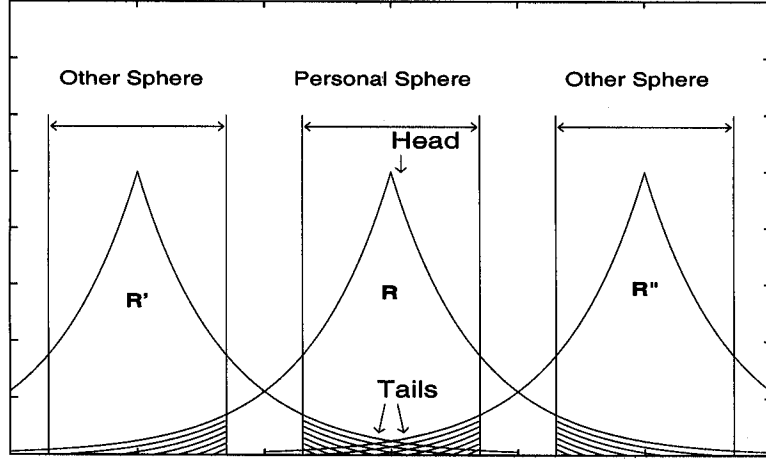


Figure 1.3: Three MTOs centered at R , R' and R'' . The tails of the central MTO lie on the other spheres and its head lies in its personal sphere. The MTOs are shown schematically only by their envelope. The tail cancellation theorem also illustrated here.

sit at those sites.

Now, if we refer to figure 1.3, we note that any muffin-tin sphere (for example, personal sphere) can be written as :

$$\Psi(r_R \leq s_R) = \chi_R^{\text{Head}} + \sum_{R' \neq R} \chi_{R'}^{\text{Tail}} \quad (1.8)$$

which is

$$\Psi(\varepsilon, r_R) = \sum_{RL} \left[\varphi_{RL}(\varepsilon, r_R) + \left\{ P_{RL}^o(\varepsilon, \kappa) \delta_{RR'} \delta_{LL'} - \sum_{L'R'} S_{L'R',LR}^o(\kappa) \right\} j_{L'}(\kappa r_{R'}) \right] Y_L(\hat{r}) c_{RL}$$

But $\sum_{RL} \varphi_{RL} Y_L c_{RL}$ is the solution of wave equation inside any of the sphere and this implies

$$\sum_{RL} \left[P_{RL}^o(\varepsilon, \kappa) \delta_{RR'} \delta_{LL'} - S_{L'R',LR}^o(\kappa) \right] c_{RL} = 0, \text{ for all } R'L' \quad (1.9)$$

This set of coupled linear equations have a solutions c_{RL} for those energies where :

$$\det |\mathbf{P}^o(\varepsilon, \kappa) - \mathbf{S}^o(\kappa)| = 0.$$

This is the **KKR Secular Equation**.

1.2.3 Linearization of energy

The KKR secular equation is an implicit equation for ε . We have no a priori idea how many roots we expect, nor whether all roots are physically permissible. The equation is not of the eigen problem type, so that we have no proof of the reality of the roots. Further, the implicit equation is computationally expensive and the full KKR is difficult to implement for solids with many atoms per unit cell. It is therefore desirable to bypass this energy dependence. Andersen and Jepsen 1984 devised a clever way of achieving just this.

The first step toward linearizing the KKR is to examine the energy dependence of the structure matrix $\mathbf{S}_{RR}^0(\kappa)$. This energy dependence is inessential if the sphere packing is close. The typical wavelength of the partial waves or the muffin-tin orbitals is of the order $2\pi/\kappa$. If this is much larger than the distance between neighbouring muffin-tin spheres, then the structure matrix has a very weak energy dependence. In most of the work using LMTO methods κ is taken to be 0, although non-zero and multiple κ calculations are also available these days.

The next step is to note that the energy dependent solution of the Schödinger equation inside a muffin-tin sphere can be expanded as a Taylor series about some energy $\varepsilon_{\nu RL}$ in our range of interest :

$$\varphi_{RL}(\varepsilon, r_R) = \varphi_{RL}(\varepsilon_{\nu RL}, r_R) + (\varepsilon - \varepsilon_{\nu RL}) \dot{\varphi}_{RL}(\varepsilon_{\nu RL}, r_R) + \mathbf{O}\left((\varepsilon - \varepsilon_{\nu RL})^2\right)$$

So the muffin-tin orbitals can be made continuous and differentiable everywhere and orthogonal to the wave functions of the core electrons.

Because of the replacement of the energy ε by a fixed energy $\varepsilon_{\nu RL}$ in the radial wave function, the LMTO method is no longer exact for the muffin-tin potential but the error in the energy is shown to be only of fourth order in the difference $\varepsilon_{\mathbf{k}j} - \varepsilon_{\nu RL}$. The block wave is constructed by taking the Block sum of the energy-independent muffin-tin orbitals. A trial function is given by the linear combination of muffin-tin orbitals thus obtained. A use of the variational principle in conjunction with the energy-independent muffin-tin orbitals results in a secular equation which is linear in energy of the form :

$$\det | \varepsilon \mathbf{I} - \mathbf{H} | = 0$$

where

$$\mathbf{H} = \mathbf{C} + \mathbf{\Delta}^{1/2} \mathbf{S}^o \mathbf{\Delta}^{1/2}$$

In expanded notation :

$$H_{RL,R'L'} = C_{RL} \delta_{RR'} \delta_{LL'} + \Delta_{RL}^{1/2} S_{RL,R'L'}^o \Delta_{R'L'}^{1/2} \quad (1.10)$$

Here the potential parameters, \mathbf{C} and $\mathbf{\Delta}$ are diagonal matrices in the angular momentum indices. One of the difficulties with the KKR method (or the linearized version of it), is that any attempt to develop a real-space technique for the solution of the secular equation is hampered by the fact that the structure matrix described above, called *canonical* in the literature, is long-ranged. To avoid this, we shall follow the idea given by Andersen *et al* 1984. The method is basically a change of basis from the canonical MTOs to the so-called *screened* MTOs. In this technique one obtain a new representation of basis in which the structure matrix is short-ranged or tight-binding like. The screened potential parameters and the screened structure matrix are obtained from the unscreened ones with the help of transformation parameters described by Andersen 1975.

1.3 Beyond linear methods : NMTO

Recent developments in MTO methods show how approximations that were introduced during development of the LMTO approach can be overcome. The new NMTO approach (Andersen *et al* 1998, Andersen and Saha-Dasgupta 2000) provides a more consistent formalism, treats the interstitial region accurately, and goes beyond the linear approximation.

In the LMTO approach, energy-independent orbitals were generated using the approximation of a fixed κ in the envelop function that describes the interstitial region. This breaks the relation of κ and the eigenvalue that causes non-linearities in the KKR method. However, it also is an approximation that is justified only in close-packed solids. In contrast, the wave function inside the sphere is treated more accurately through linearization. The NMTO method treats the sphere and interstitial equally by working with MTO-type functions $\varphi_L(\varepsilon_n, \mathbf{r} - \mathbf{R})$ localized around site \mathbf{R} and calculated at fixed energies ε_n both inside the sphere and in the interstitial (assumed to have a flat muffin-tin

potential). The NMTO basis function is then defined to be a linear combination of N such functions evaluated at N energies,

$$\chi_{RL}^{\text{NMTO}}(\varepsilon, \mathbf{r}) = \sum_{n=0}^N \sum_{R'L'} \varphi_{L'}(\varepsilon_n, \mathbf{r} - \mathbf{R}') L_{nR'L',RL}^{(N)}(\varepsilon, \mathbf{r}), \quad (1.11)$$

where $L_n^{(N)}$ is the transformation matrix that includes the idea of screening (mixing states on different sites) and a linear combination of states evaluated at N fixed energies.

As it stands, the NMTO function is energy dependent and appears to be merely a way to expand the basis. However, Andersen and coworkers (Andersen *et al* 1998, Andersen and Saha-Dasgupta 2000) have shown a way of generating energy-independent functions $\chi_{RL}^{\text{NMTO}}(\mathbf{r})$ using a polynomial approximation so that the Schrödinger equation is solved exactly at the N chosen energies. The ideas are a generalization of the transformation, which were chosen to give the correct phase shifts at an arbitrary set of energies. In the present case, the transformation is more general, mixing states of different angular momenta on different sites. The result of the transformation is that each eigenfunction is accurate to order $(\varepsilon - \varepsilon_0)(\varepsilon - \varepsilon_1) \cdots (\varepsilon - \varepsilon_N)$ and the eigenvalue to order $(\varepsilon - \varepsilon_0)^2(\varepsilon - \varepsilon_1)^2 \cdots (\varepsilon - \varepsilon_N)^2$.

If the N fixed energies are spread over a part of the spectrum, then the electronic structure is accurately reproduced over that (large) energy range. Using the NMTO we do not have to carry out the multi-panel LMTO calculations required to give accuracy over a large energy range and is essential for our optical response calculations.

1.4 The recursion method

The recursion method introduced by Haydock *et al* 1972 expresses the Hamiltonian in a form which couples an atom to its first nearest-neighbour, then through them to its more distant neighbours and so on. It is real space method by which elements of the Green function associated with a Hamiltonian are obtained by transforming the Hamiltonian in a *tridiagonal* form. The method is as follows :

Given a Hamiltonian matrix H , defined in some basis $\{|\phi_i\rangle\}$, e.g. a lattice representation, shown in figure 1.4, we seek a new set of basis vectors $(|u_0\rangle, |u_1\rangle, \dots, |u_n\rangle, |u_{n+1}\rangle)$ in which the Hamiltonian assumes a tridiagonal form Q . To reiterate, the motivation for

tridiagonalizing the Hamiltonian is due to the computational advantages this technique bears for very large matrices as will become clear in a moment.

We begin by selecting a starting vector $|u_0\rangle$, normalized to unity. We shall see in a later chapter that the choice of $|u_0\rangle$ plays an important role in determining what kind of information can be extracted from the tridiagonal matrix Q directly. To leap ahead, we state that $|u_0\rangle$ projects out the subspace of interest.

The diagonal matrix element between $|u_0\rangle$ and H is defined as

$$\alpha_0 = \langle u_0 | H | u_0 \rangle$$

We construct a new orthogonal basis vector $|u_1\rangle$ by projecting $|u_0\rangle$ onto H and subtracting the diagonal contribution,

$$\beta_1 |u_1\rangle = (H - \alpha_0) |u_0\rangle$$

Normalization of $|u_1\rangle$ yields β_1 ,

$$\beta_1^2 = [\langle u_0 | (H - \alpha_0)] [(H - \alpha_0) | u_0 \rangle]$$

For $n > 1$, the procedure continues in general as

$$\beta_{n+1} |u_{n+1}\rangle = (H - \alpha_n) |u_n\rangle - \beta_n |u_{n-1}\rangle, \quad (1.12)$$

where

$$\begin{aligned} \alpha_n &= \langle u_n | H | u_n \rangle \\ \beta_{n+1}^2 &= [\langle u_n | (H - \alpha_n) - \langle u_{n-1} | \beta_n] [(H - \alpha_n) | u_n \rangle - \beta_n | u_{n-1} \rangle] \end{aligned}$$

To illustrate the origin of equation (1.12), we rewrite it as

$$H |u_n\rangle = \beta_{n+1} |u_{n+1}\rangle + \alpha_n |u_n\rangle + \beta_n |u_{n-1}\rangle \quad (1.13)$$

The product $H |u_n\rangle$ is a linear combination of only $|u_{n+1}\rangle$, $|u_n\rangle$ and $|u_{n-1}\rangle$. By subtracting the contributions parallel to $|u_n\rangle$ and $|u_{n-1}\rangle$, therefore, the vector $|u_{n+1}\rangle$ has

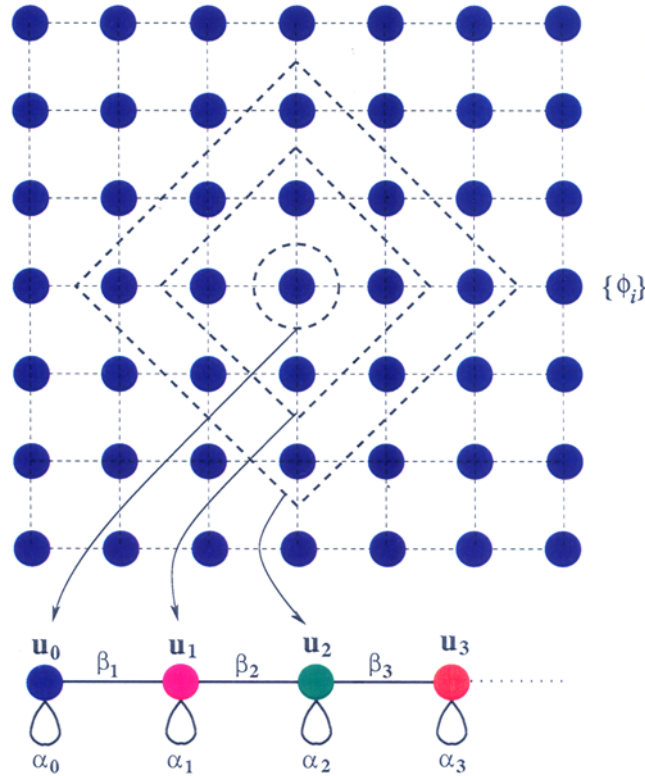


Figure 1.4: Transformation to the chain.

been constructed orthogonally to the former two, and furthermore to all previous vectors $|u_0\rangle, |u_1\rangle, \dots, |u_{n-1}\rangle$.

This construction is reminiscent of the Gram-Schmidt orthogonalization procedure, but, while in Gram-Schmidt any new vector has to be orthonormalized with respect to all previous vectors, in the case of the recursion basis any new vector needs to be orthogonalized only against the two previous ones. All other scalar products are automatically zero. The three-term recurrence relation equation (1.12) produces a new basis $\{|u_n\rangle\}$ in which the matrix has only diagonal elements $\{\alpha_n\}$ and symmetrical side diagonals $\{\beta_n\}$. The side diagonals will always be symmetrical if the matrix H is Hermitian, as is the case for all Hamiltonians.

The transformation to a tridiagonal matrix can be graphically represented as the transformation of a d -dimensional lattice into a one-dimensional semi-infinite chain model. The basis states $\{|u_n\rangle\}$ and the coupling between sites is provided by $\{\beta_n\}$, see figure 1.4.

In the lattice basis $\{|\phi_i\rangle\}$ of the Hamiltonian, each vector $|u_n\rangle$ is defined by its components $\{u_n^i\}$ on the lattice sites,

$$|u_n\rangle = \sum_i |\phi_i\rangle \langle \phi_i | u_n \rangle = \sum_i u_n^i |\phi_i\rangle \quad \text{i.e.} \quad |u_n\rangle \Rightarrow \begin{pmatrix} u_n^1 \\ u_n^2 \\ \vdots \\ u_n^j \\ \vdots \end{pmatrix} \quad (1.14)$$

If $|u_0\rangle$ is chosen so that its representation consists only of a single non-zero component located on a single site, i.e. $u_0 = \phi_0$, the vectors $\{|u_n\rangle\}$ form “shells” around the starting site, intuitively representing the “interaction” of increasingly distant environments with the state of projection.

1.4.1 Density of states

In conjunction with the Schrödinger equation a physical system is completely described by its Hamiltonian operator, H . For the present purpose it is useful to define an equivalent operator, the *Resolvent* of the Hamiltonian, called Green function :

$$G(z) \equiv (z - H)^{-1}$$

Let $\{|\psi_n\rangle\}$ be a complete set of eigenstates in Dirac notation with eigenvalues $\{\lambda_n\}$ of H . We can then rewrite it in spectral representation,

$$G(z) = \sum_n \frac{|\psi_n\rangle \langle \psi_n|}{z - \lambda_n} \quad (1.15)$$

The resolvent possesses simple poles along real axis at each eigenvalue λ_n . In an infinitely large system, the eigenvalues become dense, forming a band. The resolvent will then exhibit a branch cut for the width of the band. These observations indicate a relation to the density of states of the system : For a discrete spectrum, the density of states consists of discrete δ -functions at the location of the poles of the resolvent; for a continuous spectrum the δ -spikes fuse into a smooth function. A mathematically rigorous relation can be established by a limiting procedure approaching the singularities of the resolvent

from the above and below the real axis. Noting that

$$\lim_{\epsilon \rightarrow 0} \frac{1}{z \pm i\epsilon} = \mathcal{P} \frac{1}{z} \mp i\pi\delta(z), \quad (1.16)$$

we discover from equation (1.15) that the imaginary part of the resolvent becomes a sum of δ -functions, using the limiting procedure of equation (1.16),

$$\mp \frac{1}{\pi} \operatorname{Im} \left[\lim_{\epsilon \rightarrow 0} G(z \pm i\epsilon) \right] = \sum_n \delta(z - \lambda_n) \equiv n(z) \quad (1.17)$$

The expression on the right-hand-side is the (global) density of states $n(z)$.

1.4.2 Projected or local density of states

A quantity derived from the *global* density of states, equation (1.17) is the *projected* or *local* density of states (LDOS). The LDOS is weighted by the projection of the eigenstates $\{|\psi_n\rangle\}$ onto some state $|u\rangle$, hence the name :

$$n_{|u\rangle}(z) \equiv \sum_n |\langle \psi_n | u \rangle|^2 \delta(z - \lambda_n) \quad (1.18)$$

The projected density of states thus defined incorporates both local information by means of the overlaps with $|u\rangle$ as well as global information through the distribution of eigenstates. It is unique quantity and suited for studying the interplay of the specifics of a certain state $|u\rangle$ with the rest of the system at large. It can be used to measure the system's response to a disturbance brought on by the presence of the state $|u\rangle$. In a generalized sense, if the states are substituted for operators ("operator recursion") (Annett *et al* 1994), the resulting quantity is a *projected density of transitions* which has been employed to tackle many-body quantum problems, such as a Heisenberg spin chain. The transitions induced therein by the removal of an electron can be calculated by projecting onto annihilation operator (Haydock 2000).

The emphasis on the projected density of states stems from a neat relationship to the tridiagonal matrix Q . In the previous Section, we have shown how the global resolvent is related to the global density of states. If we consider a *projected resolvent*,

$$G_{|u\rangle}(z) \equiv \langle u | G(z) | u \rangle = \langle u | (z - H)^{-1} | u \rangle, \quad (1.19)$$

then by equations (1.17) and (1.18) the projected density of states emerges simply as

$$n_{|u\rangle}(z) = \mp \frac{1}{\pi} \operatorname{Im} \lim_{\epsilon \rightarrow 0} \langle u | (z \pm i\epsilon - H)^{-1} | u \rangle \quad (1.20)$$

If now the state $|u\rangle$ is chosen to be the starting state $|u_0\rangle$ of the recursion basis and we revert to matrix notation, then by straightforward linear algebra, the matrix element $\langle u_0 | (z - H)^{-1} | u_0 \rangle$ equals the top left matrix element of the inverse of $(z - Q)$, since $|u_0\rangle, |u_1\rangle, \dots, |u_n\rangle$ form the transformation matrix to Q ,

$$\langle u_0 | (z - H)^{-1} | u_0 \rangle = \langle e_0 | (z - Q)^{-1} | e_0 \rangle \quad (1.21)$$

where $\langle e_0 | = (1, 0, 0, \dots)$ the unit vectors in the Q basis. The top left element of an inverse matrix is easily obtained with the help of an expansion in cofactors. The result in a continued fraction expansion (Haydock 1980),

$$\langle e_0 | (E - Q)^{-1} | e_0 \rangle = \frac{1}{E - \alpha_0 - \frac{\beta_1^2}{E - \alpha_1 - \frac{\beta_2^2}{E - \alpha_2 - \frac{\beta_3^2}{E - \alpha_3 - \frac{\beta_4^2}{\ddots}}}}}$$

where the coefficients $\{\alpha_n\}$ and $\{\beta_n\}$ are the ones appearing in the tridiagonal matrix Q .

1.4.3 Terminating Schemes

If the system is infinitely large, the continued fraction does not terminate at any finite step. But in any practical calculation we can go only up to a finite number of steps, depending on our computational facility. So the continued fraction approach is meaningful only if we can estimate what its asymptotic part would be from a set of initial coefficients $\{\alpha_n, \beta_n\}$ $n = 0, \dots, N$. Once we can do this, there are several ways of appending a terminator to the continued fraction expansion of the diagonal element of the resolvent to yield the density of states. For applying the termination scheme to approximate the tail of the continued fraction, we have to ensure that the approximate resolvent (which replaces G) should be such that the corresponding approximate Hamiltonian should have

a similar energy spectrum, as the original Hamiltonian H . In other words, the resulting approximate density of states should preserve the singularities (singularities at the band edges and Van-Hove singularities) of the density of states of the system one is examining.

In case the coefficients converge after a certain number of steps, i.e. if $|\alpha_n - \alpha| \leq \epsilon$, $|\beta_n - \beta| \leq \epsilon$ for $n \geq N$, we may replace $\{\alpha_n, \beta_n\}$ by $\{\alpha, \beta\}$ for all $n \geq N$. In that case we can sum the remainder of the infinite continued fraction analytically as :

$$\Gamma(E) = \frac{\beta_n^2}{E - \alpha_n - \frac{\beta_{n+1}^2}{E - \alpha_{n+1} - \dots}}$$

is replaced by

$$\Gamma(E) = \frac{\beta^2}{E - \alpha - \frac{\beta^2}{E - \alpha} - \dots}$$

we can solve for

$$\Gamma(E) = \frac{1}{2} \left(E - \alpha - \sqrt{(E - \alpha)^2 - 4\beta^2} \right) \quad (1.22)$$

which gives a continuous spectrum in the range $\alpha - 2\beta \geq E \geq \alpha + 2\beta$. The terminator shown in equation (1.22) is called *square root terminator*.

In more complex systems involving a number of isolated bands (for example semiconductor and transition metal compounds), it is found that the $\{\alpha_n, \beta_n\}$ are not at all rapidly convergent, as they now incorporate the detailed information of internal band edges and singularities. But we need to make a reasonable choice of $\{\alpha, \beta\}$ to determine proper bandwidth and edges given by equation (1.22). It has been found that if the bandwidth chosen is too small, then the LDOS develops spurious peaks at the band edges, weight may be lost from the band by delta functions splitting off from the band edges. These delta functions have an initially zero weight which increases with their distance from the band. On the other hand, if a bandwidth is chosen which is too large, tails with negligible weight are pulled from the LDOS out the edges. But a more important effect is the emphasis of all the features in the LDOS - the LDOS tends to a spectrum of delta functions as the bandwidth tends to infinity.

Beer and Pettifor 1982 suggest a sensible criterion : given a finite number of coefficients, we must choose $\{\alpha, \beta\}$ in such a way so as to give, for this set of coefficients, the

minimum bandwidth consistent with no loss of spectral weight from the band. Let us call these values $\{\alpha_c, \beta_c\}$. This criterion is easily translated into mathematical terms. The delta function that would carry weight out the band must then be situated exactly at the band edges. We thus demand that the continued fraction diverge simultaneously at both the top and the bottom of the band.

At the band edges : $\Gamma(\alpha \pm 2\beta) = \pm\beta$, therefore, substituting $E = \alpha \pm \beta$ in the continued fraction we obtain

$$G(\alpha \pm 2\beta) = \frac{\beta_0^2/2}{\pm\beta - \frac{1}{2}(\alpha_0 - \alpha) - \frac{\beta_1^2/4}{\pm\beta - \frac{1}{2}(\alpha_1 - \alpha) - \frac{\beta_2^2/4}{\dots \frac{\beta_N^2/2}{\pm\beta - (\alpha_N - \alpha)}}}}$$

For a given α , the $(N + 1)$ eigenvalues of the finite tridiagonal matrix

$$\begin{pmatrix} \frac{1}{2}(\alpha_0 - \alpha) & \frac{1}{2}\beta_1 & 0 & \dots & \dots & 0 \\ \frac{1}{2}\beta_1 & \frac{1}{2}(\alpha_1 - \alpha) & \frac{1}{2}\beta_2 & \ddots & & \vdots \\ 0 & \frac{1}{2}\beta_2 & \ddots & \ddots & \ddots & \vdots \\ \vdots & \ddots & \ddots & \ddots & \ddots & 0 \\ \vdots & & \ddots & \ddots & \ddots & \frac{1}{\sqrt{2}}\beta_N \\ 0 & \dots & \dots & 0 & \frac{1}{\sqrt{2}}\beta_N & (\alpha_N - \alpha) \end{pmatrix}$$

are values at which the Green function diverges. The maximum and minimum of this set of eigenvalues are those values of β which carry weight out of the band. Thus our choice of α is that value for which the maximum eigenvalue is the largest and the minimum the smallest. Since the terminator only involves β^2 we must have

$$\beta_c = \sup_{\{\alpha\}} \beta_{\max}(\alpha_c) = \inf_{\{\alpha\}} |\beta_{\min}(\alpha_c)|.$$

With this choice the terminator $\Gamma(E)$ has all the Herglotz properties required.

1.5 Random alloys : Configuration averaging

The concept of configuration averaging is central to the study of disordered systems. The potentials which describe a disordered solid are characterized by random parameters. A

particular realization of these parameters, either in a given sample or at an instant is what we call a *configuration* of the system. The reason why one needs to introduce this idea for disordered system is as follows: with introduction of disorder, we face the problem of lack of sufficient information about the sample. When an experimentalist looks at a disordered sample with a view of studying its properties, he can interpret his results at most statistically. He is ignorant of microscopic configurations of random parameters of the system. For example, in a random binary alloy, the configuration of individual atoms on the lattice sites is different for different samples, and an experimentalist at the outset has no knowledge of the particular configuration of the sample. Evidently, every different sample of the random alloy will give experimental information having different microstructure according to the configuration it has. The experimentalist, on the other hand, is primarily interested in the overall statistical trends of his results which he interprets as the physical properties of the random alloy. The mass of sample dependent information about the detailed structure is of no use to him. The theorist, too, can generate from his model a myriad of results depending on the particular random configuration he chooses for his random parameters. This again is of little use to physics. One, therefore, has to evolve a statistical description of the system and the most basic of these descriptions is the averaging over all possible configurations. The correct approach for a theoretician here should be to take his cue from experiment. When an experimentalist speaks of averaged properties, he implies averaged physically measurable quantities : conductivity, susceptibility, electronic density of states etc. It is these quantities that one should average rather than averaging the Hamiltonian or the wave function. For a particular macroscopic system, the averaging over configurations is really done with the idea of *spatial ergodicity*. We assume that since the system is macroscopically large, we can partition it into subsystems, each of which resembles a configuration of the system. A global property which averages over the subsystem is then the same as average over all configurations. This assumption must hold in case of configuration averaging. In the next subsections we discuss a few methods of configuration averaging, their success and limitations.

1.6 The augmented space formalism (ASF)

The augmented space formalism introduced by Mookerjee 1973 is a conceptually elegant and exact method of configuration averaging. This formalism maps a disordered Hamiltonian described in Hilbert space \mathcal{H} onto an ordered Hamiltonian in a much enlarged Hilbert space whose Green function matrix elements correspond to appropriate configurational average of the Green function of the original disordered system. The ordered Hamiltonian is said to be in augmented space which is described as the direct product of the Hilbert space spanned by the original Hamiltonian with the configuration space which spans all possible configurations of the systems.

The probability density of a random variable n_R for a bimodal distribution has the following form :

$$p(n_R) = x \delta(n_R - 1) + y \delta(n_R) \quad (1.23)$$

It should have the following properties :

$$\begin{aligned} p(n_R) &\geq 0 \\ \int_{-\infty}^{\infty} p(n_R) dn_R &= 1 < \infty \\ \int_{-\infty}^{\infty} n_R^m p(n_R) dn_R &< \infty \quad m \geq 1 \end{aligned} \quad (1.24)$$

since the probability densities are positive definite functions, they are related to the spectral densities of a positive definite operator $G(n_R)$. That means, the probability density $p(n_R)$ is similar to the density of states of the Hamiltonian. In recursion method, one transforms the Hamiltonian into a tridiagonal one and expresses the density of states as the imaginary part of a continued fraction containing the tridiagonal elements. Inversely, if one can find a convergent continued fraction expansion of the probability density, then the tridiagonal matrix formed out of the continued fraction co-efficients is a representation of the operator \mathbf{M}_R . If n_R has a binary distribution, taking the values 1 and 0 with probabilities x and $y = 1 - x$, then one can write the right hand side of the equation (1.23) in a continued fraction expansion as :

$$p(n_R) = -\frac{1}{\pi} \text{Im} \left(\frac{x}{n_R - 1} + \frac{y}{n_R} \right)$$

$$\begin{aligned}
&= -\frac{1}{\pi} \text{Im} \left(\frac{1}{n_R - x - \frac{xy}{n_R - y}} \right) \\
&= -\frac{1}{\pi} \text{Im} \langle 1 | ((n_R + i\delta)\mathbf{I} - \mathbf{M}_R)^{-1} | 1 \rangle
\end{aligned} \tag{1.25}$$

where

$$\mathbf{M}_R = \begin{pmatrix} x & \sqrt{xy} \\ \sqrt{xy} & y \end{pmatrix}$$

Since the distribution is bimodal, the rank of the matrix \mathbf{M}_R is 2. The eigenvalues 1,0 of the matrix \mathbf{M}_R correspond to the observed values of n_R and the eigenvectors $|1_R\rangle$, $|0_R\rangle$ are the state vectors of the variable. These two state vectors span a configuration space ϕ_R of rank 2. The tridiagonal representation of \mathbf{M}_R is in a basis such that the basis vectors can be expressed in terms of the eigenvectors as :

$$\begin{aligned}
|\uparrow_R\rangle &= \sqrt{x}|1_R\rangle + \sqrt{y}|0_R\rangle \\
|\downarrow_R\rangle &= \sqrt{y}|1_R\rangle - \sqrt{x}|0_R\rangle
\end{aligned}$$

In these new basis the operator \mathbf{M}_R is :

$$n_R \rightarrow \mathbf{M}_R = x\mathcal{P}_R^\uparrow + y\mathcal{P}_R^\downarrow + \sqrt{xy} (\mathcal{T}_R^{\uparrow\downarrow} + \mathcal{T}_R^{\downarrow\uparrow}) \tag{1.26}$$

where the projection operators $\mathcal{P}_R^\uparrow = |\uparrow_R\rangle\langle\uparrow_R|$ and $\mathcal{P}_R^\downarrow = |\downarrow_R\rangle\langle\downarrow_R|$, and the transfer operator $\mathcal{T}_R^{\uparrow\downarrow} = |\uparrow_R\rangle\langle\downarrow_R|$ are in the configuration space ϕ_R spanned by the basis $|\uparrow_R\rangle$, $|\downarrow_R\rangle$.

The full configuration space $\Phi = \prod_R^\otimes \phi_R$ is then spanned by vectors of the form $|\uparrow\uparrow\downarrow\uparrow\downarrow\dots\rangle$. These configurations may be labeled by the sequence of sites $\{\mathcal{C}\}$ at which we have a \downarrow . For example, for the state just quoted $\{\mathcal{C}\} = \{3, 5, \dots\}$. This sequence is called the *cardinality sequence*. If we define the configuration $|\uparrow\uparrow\dots\uparrow\dots\rangle$ as the *reference configuration*, then the *cardinality sequence* of the *reference configuration* is the null sequence $\{\emptyset\}$.

1.6.1 The augmented space theorem

The average of a well-behaved function $f(n_R)$ of the random variable n_R is expressed as :

$$\begin{aligned} \ll f(n_R) \gg &= \int_{-\infty}^{\infty} f(n_R) p(n_R) dn_R \\ &= -\frac{1}{\pi} \text{Im} \int_{-\infty}^{\infty} f(n_R) \langle \uparrow_R | (n_R \mathbf{I} - \mathbf{M}_R)^{-1} | \uparrow_R \rangle dn_R \end{aligned} \quad (1.27)$$

Now, as the eigenvectors $\{|\lambda\rangle\}$ of the operator \mathbf{M}_R form a complete set, we may write :

$$\ll f(n_R) \gg = -\frac{1}{\pi} \text{Im} \sum_{\lambda=0,1} \sum_{\lambda'=0,1} \int_{-\infty}^{\infty} f(n_R) \langle \uparrow_R | \lambda \rangle \langle \lambda | (n_R \mathbf{I} - \mathbf{M}_R)^{-1} | \lambda' \rangle \langle \lambda' | \uparrow_R \rangle dn_R \quad (1.28)$$

But $(n_R \mathbf{I} - \mathbf{M}_R)^{-1}$ is diagonal in the eigenbasis of \mathbf{M}_R and is equal to $1/(n_R - \lambda) \delta_{\lambda\lambda'}$, so that

$$\begin{aligned} \ll f(n_R) \gg &= \sum_{\lambda=0,1} \int_{-\infty}^{\infty} f(n_R) \langle \uparrow_R | \lambda \rangle \delta(n_R - \lambda) \langle \lambda | \uparrow_R \rangle dn_R \\ &= \langle \uparrow_R | \left[\sum_{\lambda=0,1} |\lambda\rangle f(\lambda) \langle \lambda| \right] | \uparrow_R \rangle = \langle \uparrow_R | \tilde{\mathbf{f}} | \uparrow_R \rangle \end{aligned} \quad (1.29)$$

The final equation (1.29) is the central equation of the augmented space theorem. Here $\tilde{\mathbf{f}}$ is an operator built out of $f(n_R)$ by simply replacing the variable n_R by the associated operator \mathbf{M}_R . The above expression shows that the average is obtained by taking the matrix element of this operator between the *reference state* $|\uparrow_R\rangle$.

Let us generalize the above theorem for functions of many independent random variables. Suppose we have a set $\{n_R\}$ of discrete independent random variables and $f(\{n_R\})$ are some function of these random variables. So the joint probability distribution is :

$$P(n_1, \dots, n_R, \dots) = p(n_1) \dots p(n_R) \dots$$

and the generalization of the above theorem to averages of functions of the set of random variables is given by :

$$\ll f(\{n_R\}) \gg = \langle \uparrow_R | \tilde{f}(\{\tilde{\mathbf{M}}_R\}) | \uparrow_R \rangle \quad (1.30)$$

where the operators $\widetilde{\mathbf{M}}_R$ in the full configuration space Φ are built up from the operators \mathbf{M}_R as :

$$\widetilde{\mathbf{M}}_R = \mathbf{I} \otimes \mathbf{I} \otimes \dots \otimes \mathbf{M}_R \otimes \mathbf{I} \otimes \dots$$

This is the *augmented space theorem* (Mookerjee 1973).

If we wish to carry out the configuration averaging of, say, the Green function element

$$G_{RR}(z) = \langle R | (z\mathbf{I} - H(\{n_{R'}\}))^{-1} | R \rangle$$

The theorem leads to :

$$\ll G_{RR}(z) \gg = \langle R \otimes \emptyset | (z\widetilde{\mathbf{I}} - \widetilde{H}(\{\mathbf{M}_{R'}\}))^{-1} | R \otimes \emptyset \rangle \quad (1.31)$$

where

$$\widetilde{H} = \sum_R \mathcal{P}_R \otimes \widetilde{M}_R + \sum_R \sum_{R'} V_{RR'} \mathcal{T}_{RR'} \otimes \widetilde{I}$$

The power of the theorem now becomes apparent. The average is seen to be a particular matrix element of the Green function of an augmented Hamiltonian. This is constructed out of the original random Hamiltonian by replacing the random variables by the corresponding configuration space operators built out of their probability distributions. This augmented Hamiltonian is an operator in the augmented space $\Psi = \mathcal{H} \otimes \Phi$ where \mathcal{H} is the space spanned by the tight-binding basis and Φ the full configuration space. The expression in equation (1.31) is *exact*, and approximations may now be introduced in the calculation of the matrix element.

Chapter 2

The Augmented space recursion

2.1 Augmented space recursion (ASR)

From the discussion of the previous chapter it has been established that for a disordered system the augmented space theorem maps a disordered Hamiltonian described in a Hilbert space onto an ordered Hamiltonian in a space augmented by the configuration space of the random variables of the disordered Hamiltonian. The configuration average of the Green function reduces to the evaluation of a particular matrix element of the resolvent of the ordered augmented Hamiltonian in this augmented space. Hence, if one performs a recursion in the augmented space, one can obtain the matrix element necessary to calculate the configuration average of a Green function directly. The advantage of the method is that it does not involve a single site approximation or the solution of any self-consistent equation (which is a prerequisite for the CPA or its generalizations). Furthermore, one can treat both diagonal and off-diagonal disorder on an equal footing. We now briefly describe the diagonal formulation of the ASR within the framework of TB-LMTO formalism.

2.1.1 The TB-LMTO Hamiltonian for random binary alloys

The starting point of the augmented space recursion is the most localized, sparse, tight-binding Hamiltonian, derived systematically from the LMTO-ASA theory and generalized

⁰Part of this chapter has been published : **K K Saha**, T Saha-Dasgupta, A Mookerjee and I Dasgupta, *J. Phys.: Condens. Matter* **16** 1409 (2004).

to substitutionally disordered random binary alloys :

$$\mathbf{H} = \sum_{RL} \mathbf{C}_{RL} \mathcal{P}_{RL} + \sum_{RL} \sum_{R'L'} \Delta_{RL}^{1/2} S_{RL,R'L'} \Delta_{R'L'}^{1/2} \mathcal{T}_{RL,R'L'}$$

The *potential parameters*, \mathbf{C} and Δ are diagonal matrices in the angular momentum indices, and

$$\begin{aligned} \mathbf{C}_{RL} &= C_L^A n_R + C_L^B (1 - n_R) \\ \Delta_{RL}^{1/2} &= (\Delta_L^A)^{1/2} n_R + (\Delta_L^B)^{1/2} (1 - n_R) \end{aligned} \quad (2.1)$$

Here R refers to the position of atoms in the solid and L is a composite label $\{\ell, m, m_s\}$ for the angular momentum quantum numbers. n_R is the random site-occupation variable which takes values 0 or 1 with probability x or y ($x + y = 1$) respectively, depending upon whether the muffin-tin labeled by R is occupied by A or B-type of atom.

The \mathcal{P}_{RL} and $\mathcal{T}_{RL,R'L'}$ are projection and transfer operators in the Hilbert space \mathcal{H} spanned by the tight-binding basis $\{|RL\rangle\}$.

2.1.2 Configuration-averaged Green function

We first want to introduce the configuration-averaged Green function which is defined as the resolvent of the random Hamiltonian. To do this, we suppress all the indices and express the Green function in the following form :

$$\begin{aligned} \mathbf{G}(E) &= (E\mathbf{I} - \mathbf{H})^{-1} = (E\mathbf{I} - \mathbf{C} - \Delta^{-1/2} \mathbf{S} \Delta^{-1/2})^{-1} \\ &= \Delta^{-1/2} \left\{ (E\mathbf{I} - \mathbf{C})/\Delta - \mathbf{S} \right\} \Delta^{-1/2} \end{aligned} \quad (2.2)$$

Using the augmented space theorem, we can write the expression of configuration averaged Green function as

$$\begin{aligned} \ll \mathbf{G}(E) \gg &= \langle \{\emptyset\} \parallel \mathbf{D} \left\{ \left[(E\mathbf{I} - \mathbf{C}^B)/\Delta^B \right] \mathcal{P}_{RL} \otimes \mathbf{I} \dots \right. \\ &\quad \left. + \delta \left[(E\mathbf{I} - \mathbf{C})/\Delta \right] \mathcal{P}_{RL} \otimes \mathbf{M}_R - \mathbf{S} \mathcal{T}_{RR'} \otimes \mathbf{I} \right\}^{-1} \mathbf{D} \parallel \{\emptyset\} \rangle \end{aligned}$$

where

$$\mathbf{D} \parallel \{\emptyset\} \rangle = \left(\Delta_L^B \mathcal{P}_{RL} \otimes \mathbf{I} + \delta \Delta_L \mathcal{P}_{RL} \otimes \mathbf{M}_R \right) \mid R, L \otimes \{\emptyset\} \rangle$$

where $\delta()$ denotes the difference of potentials at A and B. After a little bit of algebra, we arrive at a convenient expression as

$$\ll \mathbf{G}(E) \gg = \langle \{\emptyset\} | \tilde{\mathbf{D}} (\tilde{\mathbf{A}} + \tilde{\mathbf{B}} + \tilde{\mathbf{F}} - \tilde{\mathbf{S}})^{-1} \tilde{\mathbf{D}} | \{\emptyset\} \rangle \quad (2.3)$$

where

$$\begin{aligned} \tilde{\mathbf{A}} &= \sum_{RL} A [(E - C_L)/\Delta_L] \mathcal{P}_R \otimes \mathcal{P}_L \otimes \mathcal{I} \\ \tilde{\mathbf{B}} &= \sum_{RL} B [(E - C_L)/\Delta_L] \mathcal{P}_R \otimes \mathcal{P}_L \otimes \mathcal{P}_R^\dagger \\ \tilde{\mathbf{F}} &= \sum_{RL} C [(E - C_L)/\Delta_L] \mathcal{P}_R \otimes \mathcal{P}_L \otimes \{\mathcal{T}_R^{\uparrow\dagger} + \mathcal{T}_R^{\dagger\uparrow}\} \\ \tilde{\mathbf{S}} &= \sum_{RL} \sum_{R'L'} S_{RL,R'L'} \mathcal{T}_{RR'} \otimes \mathcal{T}_{LL'} \otimes \mathcal{I} \\ \tilde{\mathbf{D}} &= \sum_{RL} A (\Delta_L^{1/2}) \mathcal{P}_R \otimes \mathcal{P}_L \otimes \mathcal{I} + \sum_{RL} B (\Delta_L^{1/2}) \mathcal{P}_R \otimes \mathcal{P}_L \otimes \mathcal{P}_R^\dagger \\ &\quad + \sum_{RL} C (\Delta_L^{1/2}) \mathcal{P}_R \otimes \mathcal{P}_L \otimes \{\mathcal{T}_R^{\uparrow\dagger} + \mathcal{T}_R^{\dagger\uparrow}\} \end{aligned}$$

and

$$\begin{aligned} A(\mathbf{V}) &= x\mathbf{V}_A + y\mathbf{V}_B \quad i.e. \text{ the average of } \mathbf{V} \\ B(\mathbf{V}) &= (1 - 2x)(\mathbf{V}_A - \mathbf{V}_B) \\ F(\mathbf{V}) &= \sqrt{xy}(\mathbf{V}_A - \mathbf{V}_B) \end{aligned}$$

Since

$$\tilde{\mathbf{D}}|\{\emptyset\}\rangle = A(\Delta_L^{-1/2})|\{\emptyset\}\rangle + F(\Delta_L^{-1/2})|\{R\}\rangle = |1\rangle$$

The ket $|1\rangle$ is not normalized. We first write the above in terms of a normalized ket $|1\rangle = [A(\Delta^{-1})]^{-1/2} |1\rangle$. We now have :

$$\begin{aligned} \ll \mathbf{G}(E) \gg &= \langle 1 | (\mathbf{E}\tilde{\mathbf{I}} - \tilde{\mathbf{A}}' - \tilde{\mathbf{B}}' - \tilde{\mathbf{F}}' - \tilde{\mathbf{S}}')^{-1} | 1 \rangle = \langle 1 | (\mathbf{E}\tilde{\mathbf{I}} - \tilde{\mathbf{H}}^{\text{eff}})^{-1} | 1 \rangle \\ \tilde{\mathbf{H}}^{\text{eff}} &= \tilde{\mathbf{A}}' + \tilde{\mathbf{B}}' + \tilde{\mathbf{F}}' + \tilde{\mathbf{S}}' \end{aligned} \quad (2.4)$$

where

$$\tilde{\mathbf{A}}' = \sum_{RL} \{A(C_L/\Delta_L)/A(1/\Delta_L)\} \mathcal{P}_R \otimes \mathcal{P}_L \otimes \tilde{\mathcal{I}}$$

$$\begin{aligned}
\tilde{\mathbf{B}}' &= \sum_{RL} \{B[(C_L - E)/\Delta_L]/A(1/\Delta_L)\} \mathcal{P}_R \otimes \mathcal{P}_L \otimes \mathcal{P}_R^\dagger \\
\tilde{\mathbf{F}}' &= \sum_{RL} \{C[(C_L - E)/\Delta_L]/A(1/\Delta_L)\} \mathcal{P}_R \otimes \mathcal{P}_L \otimes \{\mathcal{T}_R^{\uparrow\downarrow} + \mathcal{T}_R^{\downarrow\uparrow}\} \\
\tilde{\mathbf{S}}' &= \sum_{RL} \sum_{R'L'} [A(1/\Delta_L)]^{-1/2} S_{RL,R'L'} [A(1/\Delta_{L'})]^{-1/2} \mathcal{T}_{RR'} \otimes \mathcal{T}_{LL'} \otimes \tilde{\mathcal{I}} \quad (2.5)
\end{aligned}$$

This equation is exactly in the form in which the recursion method may now be applied. The computational burden is considerably reduced due to this diagonal formulation, the recursion now becomes energy dependent as is clear from the form of the effective Hamiltonian as shown in (2.3). The recursion formalism of the ordered Hamiltonian was free of this constraint. This energy dependence makes the recursion technique computationally unsuitable because to obtain the Green functions we have to carry out recursion per energy point of interest. This problem has been tackled using *seed recursion technique* (Ghosh *et al* 1999). The idea is to choose a few seed points across the energy spectrum uniformly, carry out recursion over those points and then interpolate the values of coefficients across the band. In this way one may reduce computation time. For example, if one is interested in an energy spectrum of 200 points, in the bare diagonal formulation recursion has to be carried out at all the 200 points, but in the seed recursion technique one needs to perform recursions only at 10-15 points. The whole idea stems from the fact that in most of the cases of binary alloys, it is seen that the recursion coefficients α_n and β_n vary quite weakly across the energy spectrum. At this point we note that the above expression for the averaged $\ll G_{LL}(E) \gg$ is *exact*.

2.2 Symmetry reduction of the augmented space rank

We mentioned earlier that recursion on the augmented space is not computationally feasible because of its large rank. For a binary alloy with N sites and with only s-orbitals on them, the rank of the augmented space is $N \times 2^N$. Implementing recursion on this huge space for a sufficient number of steps to ensure accuracy is often not feasible on available computers. However, if we exploit the symmetry both of the underlying lattice in real-space and of the configuration space (which arises due to the homogeneity of the disorder and arrangements of atoms on the underlying lattice), the rank of the irreducible part of the augmented space in which the recursion is effectively carried out becomes tractable.

The conceptual advantages in ASF include, apart from analyticity, translational and underlying lattice symmetries automatically built into the augmented space Hamiltonian. This allows us to involve the idea of utilizing symmetry operations present in both the real and configuration spaces, in the context of recursion method, reducing the rank of the Hamiltonian drastically and making the implementation of ASF feasible. Since the augmented space recursion essentially retains all the properties of real-space recursion but is described in a much enlarged space, it will be useful to consider symmetry operations in real-space recursion first and then consider those in the full augmented space.

During the recursion, the basis member $|u_n\rangle$ is generated from the starting state $|u_1\rangle$ by repeated application of the Hamiltonian. If the starting state belongs to an irreducible sub-space of the Hilbert space, then all subsequent states generated from recursion will belong to the same irreducible sub-space. Physically, we may understand this as follows: the recursion states $|u_n\rangle$ carry information on the distant environment of the starting state. If the Hamiltonian is nearest-neighbour *only*, then the state $|u_2\rangle$, which arises by the application of the Hamiltonian on $|u_1\rangle$ is a combination of states in the nearest shell with which $|u_1\rangle$ couples via the Hamiltonian. Similarly, $|u_n\rangle$ is a combination of n th neighbour shell with which $|u_1\rangle$ is coupled via the Hamiltonian. If \mathcal{R} is a point group symmetry of the Hamiltonian, then all n th neighbour-shell states which are related to one another through the symmetry operator must have equal coupling to $|u_1\rangle$. Hence, it is useful to consider among the n th neighbour-shell states of which $|u_n\rangle$ is a linear combination, only those belonging to the irreducible subspace and redefine the Hamiltonian operation.

As an example, take a nearest-neighbour s-state Anderson model on a square lattice, with a binary distribution of its diagonal elements. We shall label the tight-binding basis with the position of the lattice points in units of the lattice constant, e.g. $|(mn)\rangle$ where m, n are integers $0, \pm 1, \pm 2, \dots$. The starting state $|(00)\rangle$ belongs to the one-dimensional representation of the point group of a square lattice. This state then couples with linear combinations of states on neighbour shells which are symmetric under the operations which transforms the square onto itself, i.e. $\pi/2, \pi$ and $3\pi/2$ rotations about the \hat{z} axis :

$$\begin{aligned} |(0m)\rangle &= \left(|(0m)\rangle + |(m0)\rangle + |(\bar{m}0)\rangle + |(0\bar{m})\rangle \right) / 2, \quad m > 0 \\ |(mm)\rangle &= \left(|(mm)\rangle + |(\bar{m}m)\rangle + |(m\bar{m})\rangle + |(\bar{m}\bar{m})\rangle \right) / 2, \quad m > 0 \end{aligned}$$

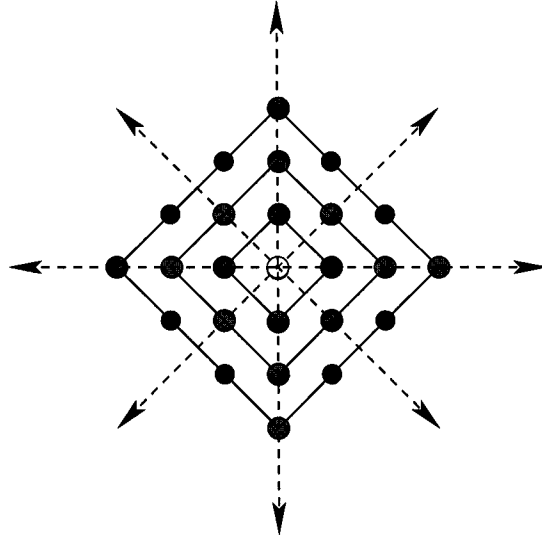


Figure 2.1: Nearest neighbour shells around a central site on a square lattice. The colour coding indicates the symmetry weight of the sites : white represents sites with weight 1, gray with weight 4 and black with weight 8.

$$\begin{aligned}
 |(mn)\rangle &= \left(|(mn)\rangle + |(\bar{m}n)\rangle + |(m\bar{n})\rangle + |(\bar{m}\bar{n})\rangle \dots \right. \\
 &\quad \left. + |(nm)\rangle + |(\bar{n}m)\rangle + |(n\bar{m})\rangle + |(\bar{n}\bar{m})\rangle \right) / (2\sqrt{2}) \\
 &\qquad\qquad\qquad m > 1, \quad 0 < n < m \qquad (2.6)
 \end{aligned}$$

Figure 2.1 shows the grouping together of sites with the local symmetry of the square lattice on the first three nearest-neighbour shells of the central site. The first and second groups in (2.6) are coloured gray in figure 2.1 and the last group coloured black. The labels on the groups (shown on the left sides of the equations (2.6)) are confined *only* to the upper right quadrant of the lattice.

If we go up to N shells (for large N) there are about $2N^2$ states in the diamond shaped nearest-neighbour cluster. However, there are only $(N^2/4 + N/2) \sim N^2/4$ states with square symmetry.

So within this reduction we can work only in 1/8th of the lattice, provided we incorporate proper weights into the states to reproduce the correct matrix elements. If $|R\rangle$ and $|R'\rangle$ are two states coupled to each other via the Hamiltonian, and both belong to the same irreducible subspace, and if $|R_1\rangle, |R_2\rangle, \dots, |R_{\mathcal{W}_R}\rangle$ are states obtained by operating

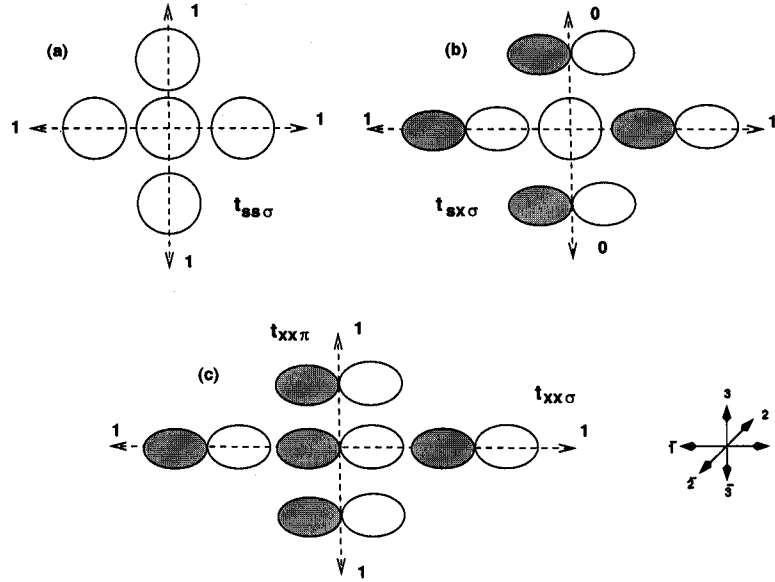


Figure 2.2: sp-orbitals on a cubic lattice. Only projections on the xy plane are shown. The positive parts of the lobes are unshaded, while the negative parts of the lobes are shaded. The values of the symmetry factor for the overlaps ($\beta_{LL'}(\ell m)$, defined in the text) are shown for each direction. The numbering of sites on the cubic lattice is shown in the inset at the bottom right.

on $|R\rangle$ by the symmetry group operations of the real-space lattice, then \mathcal{W}_R is called the *weight* associated with the state labeled by R . If we wish to retain only the states in the irreducible subspace and throw out the others and yet obtain the same results, we have to redefine the Hamiltonian matrix elements as follows :

$$\langle R|H|R'\rangle \rightarrow \sqrt{\frac{\mathcal{W}_{R'}}{\mathcal{W}_R}} \langle R|H|R'\rangle. \quad (2.7)$$

In the above prescription, the new irreducible basis only reflects the symmetry of the underlying lattice and holds properly for a model system which has s-like orbitals only. But for a real system, the TB-LMTO minimal basis contains members with other symmetries as well. For example, in a cubic lattice with a spd minimal basis, we have basis members with s, p, e_g and t_{2g} symmetries. The symmetry of the orbitals is reflected in the two-centered Slater-Koster integrals and this prohibits overlap integrals at certain positions, called *symmetric positions* with respect to the overlapping orbitals. A few of these sym-

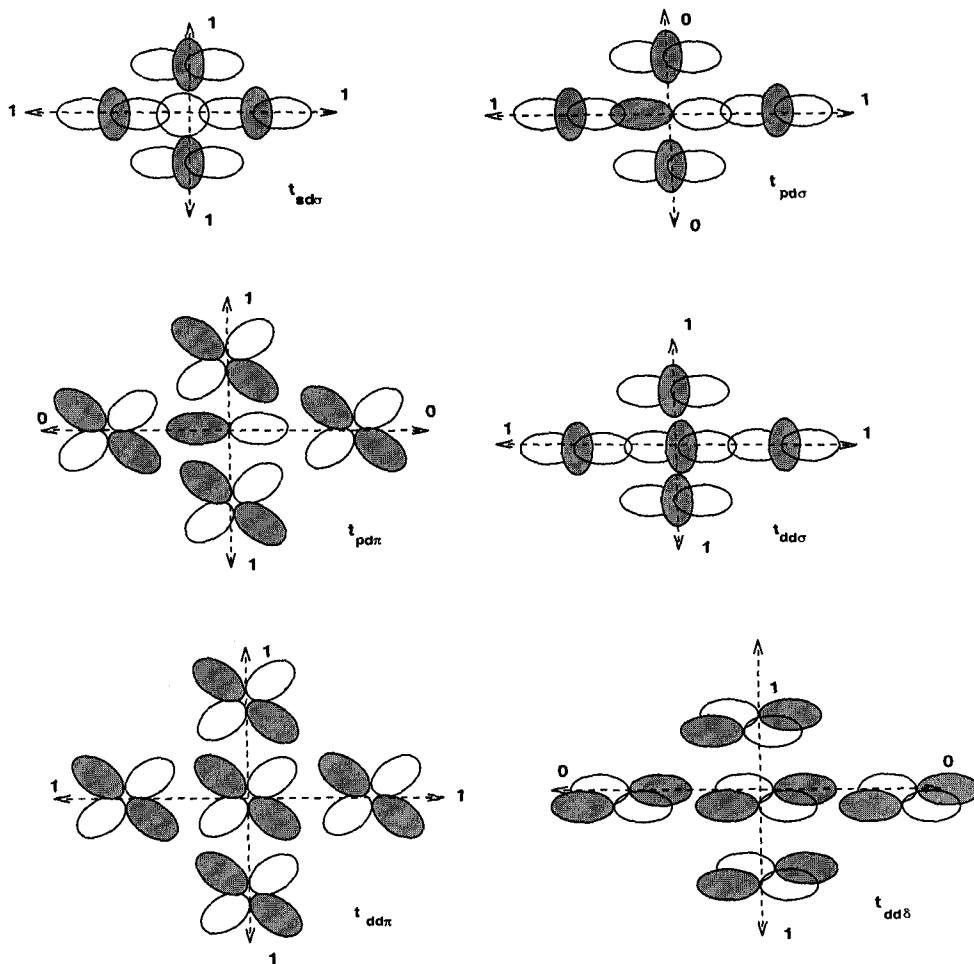


Figure 2.3: Overlaps involving d orbitals in the e_g and t_{2g} symmetries. Only projections in the xy plane are shown. The positive parts of the lobes are unshaded, while the negative parts of the lobes are shaded.

metric positions for a simple cubic lattice are shown in figure 2.2. For the sake of clarity we have shown only the projections on xy plane. We have indicated the positive and negative parts of the orbital lobes by different shades. From figure 2.2(b) it is easy to argue that since the Hamiltonian is spherically symmetric and the product $\phi_s(000)\phi_{p_x}(010)$ is positive in the upper right quadrant and negative in the upper left quadrant : $\langle 0, s|H|2, p_x\rangle = 0$. The same is true for $\langle 0, s|H|\bar{2}, p_x\rangle = 0$. Similarly, $\langle 0, s|H|3, p_x\rangle = \langle 0, s|H|\bar{3}, p_x\rangle = 0$. On the other hand, $\langle 0, s|H|1, p_x\rangle = -\langle 0, s|H|\bar{1}, p_x\rangle \neq 0$.

The above is an illustration; detailed arguments for the orbital symmetry have been

discussed by Harrison 1999.

Table 2.1 provides the conditions for obtaining the orbital based symmetry factor $\beta_{LL'}(R - R')$ for a lattice with cubic symmetry. We shall describe the direction of $\vec{R} - \vec{R}'$ by the direction cosines (lmn) . The table gives the details for the calculation of the symmetry factor $\beta_{LL'}(lmn)$ on a cubic lattice. A look at figures 2.2 and 2.3 shows why this factor needs to be introduced.

For the s-orbital overlaps the symmetry factor is always 1 (figure 2.2(a)). All six neighbours in the cubic lattice in the directions (100) , $(\bar{1}00)$, (010) , $(0\bar{1}0)$, (001) and $(00\bar{1})$ are equivalent with the same overlap integrals $t_{ss\sigma}$ (only four are shown in the xy plane). We may then reduce the lattice and retain only the neighbour in the (100) direction and scale the overlap $t_{ss\sigma}$ by the appropriate weight (i.e. 2 in this case) as discussed earlier. The sp_x overlaps (figure 2.2(b)), in the (010) , $(0\bar{1}0)$, (001) and $(00\bar{1})$ directions are zero. This can be deduced immediately by noticing that the overlap products in these directions are positive for $x > 0$ and negative for $x < 0$. Therefore, although they are related to one another by the symmetry operations of the cubic lattice, the overlaps in the (100) and $(\bar{1}00)$ directions are different from those in the (010) , $(0\bar{1}0)$, (001) and $(00\bar{1})$ directions and we will have to set the latter to be zero by introducing the symmetry factor $\beta_{LL'}(lmn)$.

$$\langle RL|H|R'L' \rangle \rightarrow \sqrt{\frac{\mathcal{W}_{R'}}{\mathcal{W}_R}} \beta_{LL'}(lmn) \langle RL|H|R'L' \rangle \quad (2.8)$$

where $\beta_{LL'}(lmn)$ is 0 if R' is a symmetric position of R with respect to L and L' , otherwise it is 1.

Figure 2.3 illustrates some of the overlaps involving the d states with e_g and t_{2g} symmetries. With this simple reduction procedure the real-space part can be reduced to 1/8th, keeping only the sites in the $(x > 0, y > 0, z > 0)$ octant and suitably re-normalizing the Hamiltonian matrix elements as described earlier.

We still have not exhausted all the symmetries in the full augmented space. As discussed earlier, this space is a direct product of the real (lattice-orbital) space and the configuration space which are disjoint. As a consequence the symmetry operations apply independently to each of them. Since the disorder is homogeneous, the cardinality sequence in configuration space itself has the symmetry of the underlying lattice. To see

Table 2.1: Table showing the Slater-Koster parameters and the consequent symmetry factors $\beta_{LL'}^{\ell mn}$. The parameters for which the zero condition have been omitted can be obtained from the last column by permuting the direction cosines.

Matrix Element	Slater-Koster Expression	Symmetry Factor	Condition for it to be zero
t_{ss}	$t_{ss\sigma}$	$\beta_{s,s}^{\ell mn}$	—
$t_{s,x}$	$\ell t_{sp\sigma}$	$\beta_{s,p_x}^{\ell mn}$	$\ell = 0$
$t_{s,xy}$	$\sqrt{3} \ell m t_{sd\sigma}$	$\beta_{s,xy}^{\ell mn}$	$\ell = 0$ or $m = 0$
t_{s,x^2-y^2}	$\sqrt{3}/2 (\ell^2 - m^2) t_{sd\sigma}$	$\beta_{s,x^2-y^2}^{\ell mn}$	$\ell = m$
$t_{s,3z^2-r^2}$	$[n^2 - 1/2(\ell^2 + m^2)] t_{sd\sigma}$	$\beta_{s,3z^2-r^2}^{\ell mn}$	$n = 1/\sqrt{3}$
$t_{x,x}$	$\ell^2 t_{pp\sigma} + (1 - \ell^2) t_{pp\pi}$	$\beta_{x,x}^{\ell mn}$	—
$t_{x,y}$	$\ell m (t_{pp\sigma} - t_{pp\pi})$	$\beta_{x,y}^{\ell mn}$	$\ell = 0$ or $m = 0$
$t_{x,xy}$	$m [\sqrt{3}\ell^2 t_{pd\sigma} + (1 - 2\ell^2) t_{pd\pi}]$	$\beta_{x,xy}^{\ell mn}$	$m = 0$
$t_{x,yz}$	$\sqrt{3} \ell m (t_{pd\sigma} - 2 t_{pd\pi})$	$\beta_{x,yz}^{\ell mn}$	$\ell = 0$ or $m = 0 \dots$ \dots or $= 0$
t_{x,x^2-y^2}	$\ell [\sqrt{3}/2 (\ell^2 - m^2) t_{pd\sigma} + (1 - \ell^2 + m^2) t_{pd\pi}]$	$\beta_{x,x^2-y^2}^{\ell mn}$	$\ell = 0$
t_{z,x^2-y^2}	$(\ell^2 - m^2) [\sqrt{3}/2 t_{pd\sigma} - t_{pd\pi}]$	$\beta_{z,x^2-y^2}^{\ell mn}$	$= 0$ or $\ell = m$
$t_{x,3z^2-r^2}$	$\ell \{ [2 - (\ell^2 + m^2)/2] t_{pd\sigma} - \sqrt{3}^2 t_{pd\pi} \}$	$\beta_{x,3z^2-r^2}^{\ell mn}$	$\ell = 0$
$t_{xy,xy}$	$3\ell^2 m^2 t_{dd\sigma} + (\ell^2 + m^2 - 4\ell^2 m^2) t_{dd\pi} \dots$ $\dots + (2 + \ell^2 m^2) t_{dd\delta}$	$\beta_{xy,xy}^{\ell mn}$	—
$t_{xy,yz}$	$\ell \{ 3m^2 t_{dd\sigma} + (1 - 4m^2) t_{dd\pi} \} + (m^2 - 1) t_{dd\delta}$	$\beta_{xy,yz}^{\ell mn}$	$\ell = 0$ or $= 0$
t_{xy,x^2-y^2}	$\ell m (\ell^2 - m^2) \{ (3/2) t_{dd\sigma} - 2 t_{dd\pi} + (1/2) t_{dd\delta} \}$	$\beta_{xy,x^2-y^2}^{\ell mn}$	$\ell = 0$ or $m = 0 \dots$ \dots or $\ell = m$
t_{yz,x^2-y^2}	$m \{ (3/2) (\ell^2 - m^2) t_{dd\sigma} - [1 + 2(\ell^2 - m^2)] t_{dd\pi} \dots$ $\dots + [1 + 1/2(\ell^2 - m^2)] t_{dd\delta} \}$	$\beta_{yz,x^2-y^2}^{\ell mn}$	$m = 0$ or $= 0$
$t_{xy,3z^2-r^2}$	$\sqrt{3} \ell m \{ [2 - 1/2(\ell^2 + m^2)] t_{dd\sigma} - 2^2 t_{dd\pi} \dots$ $\dots + 1/2(1 + \ell^2) t_{dd\delta} \}$	$\beta_{xy,3z^2-r^2}^{\ell mn}$	$\ell = 0$ or $m = 0$
$t_{x^2-y^2,x^2-y^2}$	$3/4(\ell^2 - m^2)^2 t_{dd\sigma} + [\ell^2 + m^2 - (\ell^2 - m^2)^2] t_{dd\pi} \dots$ $\dots + [2 + 1/4(\ell^2 - m^2)^2] t_{dd\delta}$	$\beta_{x^2-y^2,x^2-y^2}^{\ell mn}$	—
$t_{x^2-y^2,3z^2-r^2}$	$\sqrt{3} (\ell^2 - m^2) \{ [2/2 - 1/4(\ell^2 + m^2)] t_{dd\sigma} - 2^2 t_{dd\pi} \dots$ $\dots + 1/4(1 + \ell^2) t_{dd\delta} \}$	$\beta_{x^2-y^2,3z^2-r^2}^{\ell mn}$	$\ell = m$
$t_{3z^2-r^2,3z^2-r^2}$	$[2 - 1/2(\ell^2 + m^2)]^2 t_{dd\sigma} + 3^2(\ell^2 + m^2) t_{dd\pi} \dots$ $\dots + 3/4(\ell^2 + m^2)^2 t_{dd\delta}$	$\beta_{3z^2-r^2,3z^2-r^2}^{\ell mn}$	—

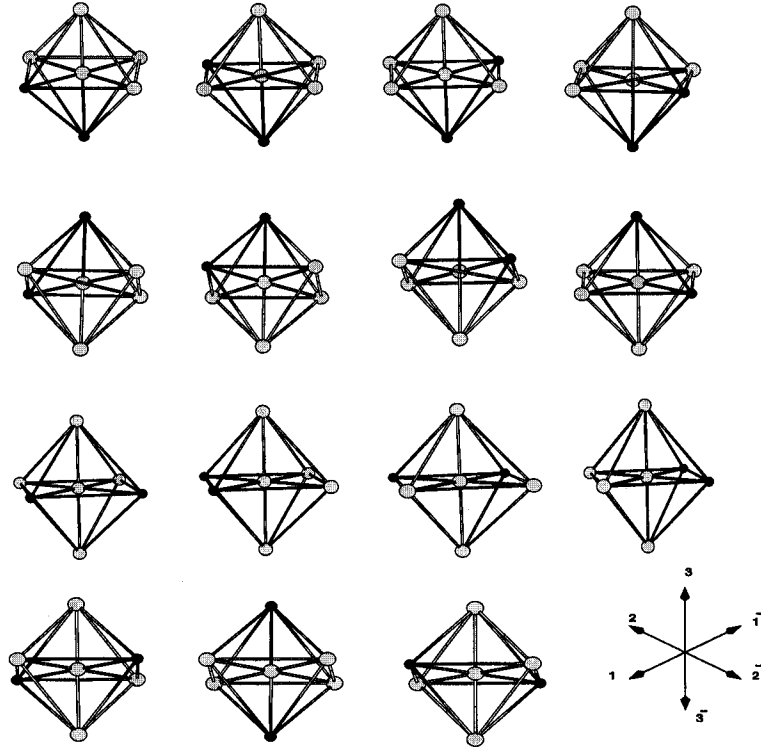


Figure 2.4: Equivalent configurations on a cubic lattice. Configurations labelled by \uparrow are shown as light spheres, while those labeled by \downarrow are shown as dark spheres. The top twelve configurations are equivalent, while the bottom three are equivalent. The lower right inset shows the numbering scheme used for the lattice sites in the main text.

this, let us look at figure 2.4 where we show a part of a cubic lattice where the central site is occupied by a configuration labelled by \uparrow , while two of the six nearest-neighbours are occupied by configurations labeled by \downarrow , and four of them by \uparrow s. We note that the twelve configurations in the first three rows of the figure, where the two \downarrow s sit at distances $\sqrt{2}$ times the lattice constant, are related to one another by the symmetry operations of the cubic lattice. For example, the second to the fourth configurations on the top row of figure 2.4, can be obtained from the first by the rotations $\mathcal{R}(\pi/2, \hat{z})$, $\mathcal{R}(\pi, \hat{z})$ and $\mathcal{R}(3\pi/2, \hat{z})$ respectively. The configurations are described by *cardinality sequences* (as described earlier). The cardinality sequences for the four configurations on the top row

of figure 2.4 are : $\{1\bar{3}\}$, $\{2\bar{3}\}$, $\{\bar{1}3\}$ and $\{\bar{2}3\}$. From the figure it is easy to see that :

$$\{2\bar{3}\} = \mathcal{R}(\pi/2, \hat{z}) \{1\bar{3}\} ; \{\bar{1}3\} = \mathcal{R}(\pi, \hat{z}) \{1\bar{3}\} \text{ and } \{\bar{2}3\} = \mathcal{R}(3\pi/2, \hat{z}) \{1\bar{3}\}$$

This equivalence of the configurations on the lattice is quite independent of the symmetries of the Hamiltonian in real-space discussed earlier. Thus, in augmented space, equivalent states are $|R \otimes \{C\}\rangle$ and the set $|\mathfrak{R}R \otimes \mathfrak{R}\{C\}\rangle$ for all different symmetry operators \mathfrak{R} of the underlying lattice. Again the symmetry of the orbitals also rules out the operation of the Hamiltonian at certain symmetric positions discussed earlier.

Once we have defined the reduced Hamiltonian, recursion on the reduced augmented space with starting state $|u_1\rangle = |RL \otimes \{\emptyset\}\rangle$ gives the configuration averaged Green function directly.

In order to give the readers a flavour of the reduction in storage and CPU time, we have carried out two sets of recursion calculations : first, a standard recursion on ordered Ag on a fcc lattice, and second, an augmented space recursion with 15 seed points on a fcc alloy $\text{Ag}_{50}\text{Pd}_{50}$ both with and without symmetry reduction. The calculations were done on a P4 machine with 1.13 GHz clock speed and 256 MB RAM.

The first point to note is that convergence of the recursion technique is measured by the convergence of the energy moments of the corresponding density of states obtained from recursion (Haydock 1980, Chakrabarti and Mookerjee 2002). These energy moments are defined by :

$$M_n = \int_{-\infty}^{E_F} dE E^n n(E) \quad \text{where} \quad \int_{-\infty}^{E_F} dE n(E) = n_e$$

where n_e is the number of valence electrons. The convergence of these moments with the number of recursion steps N , from which the density of states $n(E)$ and the Fermi energy E_F is calculated, is reflected in the errors

$$\Delta M_n^N = |M_n^N - M_n^{N-1}|.$$

Figure 2.5 shows the convergence of the first three moments for a $\text{Ag}_{50}\text{Pd}_{50}$ disordered alloy on a fcc lattice in a spd TB-LMTO minimal basis set. It is clear from the figure that for a convergence within a specified error window one has to carry out recursion for

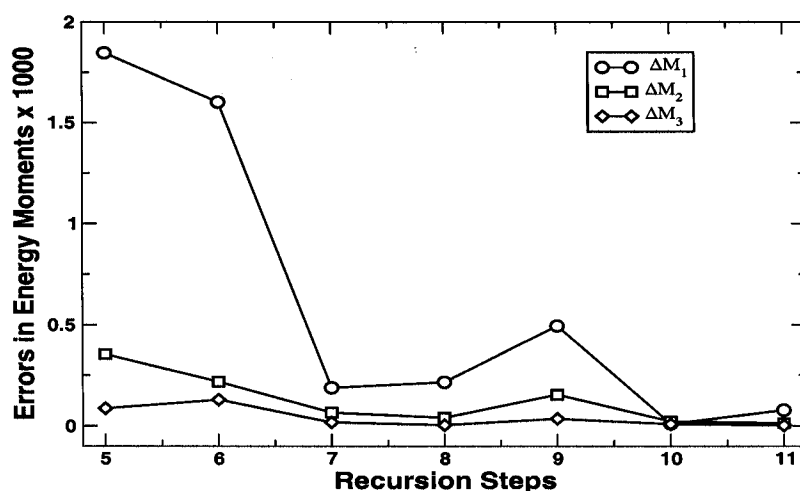


Figure 2.5: Convergence of the errors in energy moments of $\text{Ag}_{50}\text{Pd}_{50}$ as functions of the recursion step.

a specific large number of steps determined by the error window. Symmetry reduction allows us to carry out recursion exactly over a much larger number of steps than is possible for ordinary recursion, given our computational resources. There was a similar observation made in an earlier estimate of the errors of the recursion method (Chakrabarti and Mookerjee 2002). In order to carry out this many recursion steps we have to generate at least this many shells exactly around the starting site in order to avoid surface-like effects. Haydock *et al* 1972 have suggested a *trick* which allow us to obtain extra levels of continued fraction without severe consequence on the accuracy of the calculations. However, this *trick* gives even better accuracy if the starting point of the extension is itself after a larger number of exact recursions, which our symmetry reduction allows us to do.

For the case of the ordered fcc lattice, figure 2.6 shows how the size of the map increases as we increase the number of nearest-neighbour shells from a starting site, both with and without reduction. Table 2.2 shows the details of the CPU time and storage space reduction for recursion after applying the symmetry reduction. We have carried out calculations both on a simple model system with s-states on a fcc lattice, as well as for Ag (with spd minimal TB-LMTO basis) also on a fcc lattice, both with nearest-neighbour

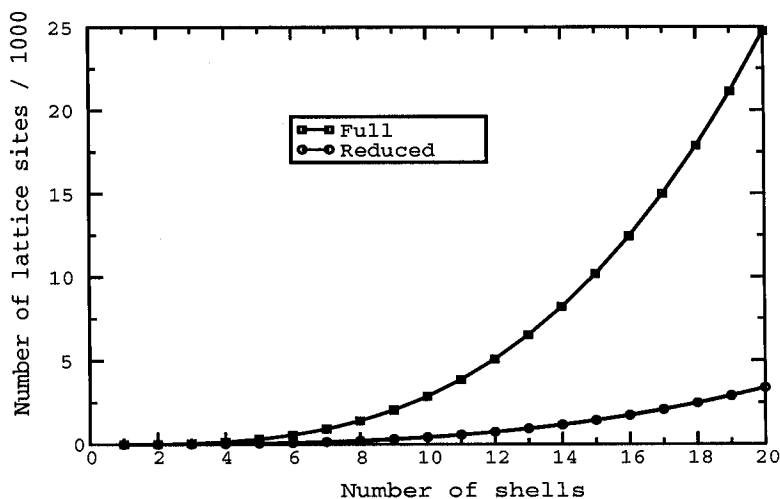


Figure 2.6: Showing how the number of lattice sites increase with increasing the number of shells in the real-space map and its reduced version. This is for an ordered fcc lattice.

hopping integrals only.

For the calculation of a disordered binary alloy on a fcc lattice, figure 2.7 shows the enormous decrease in the size of the augmented space map after application of symmetry reduction for a seven nearest-neighbour map on a fcc lattice. Table 2.3 tabulates the reduction in storage and CPU time for a 7 shell, 11 step recursion in augmented space carried over 15 seed points using TB-LMTO potential parameters and structure matrix to build the Hamiltonian. The power of symmetry reduction on storage space is more evident

Table 2.2: Comparison between system size and CPU time (in seconds) taken for recursion on a P4/256 machine for a full fcc lattice and the reduced lattice in real-space. The model system consists of s-states with nearest-neighbour hopping integrals and the Hamiltonian for Ag is taken from a TB-LMTO calculation with a minimal spd basis.

		Full lattice			Reduced lattice	
System	Shells	Steps	Sites	CPU time	Sites	CPU time
Model	20	20	24739	2.36	3385	0.54
Ag	20	30	24739	47.15	3385	15.83

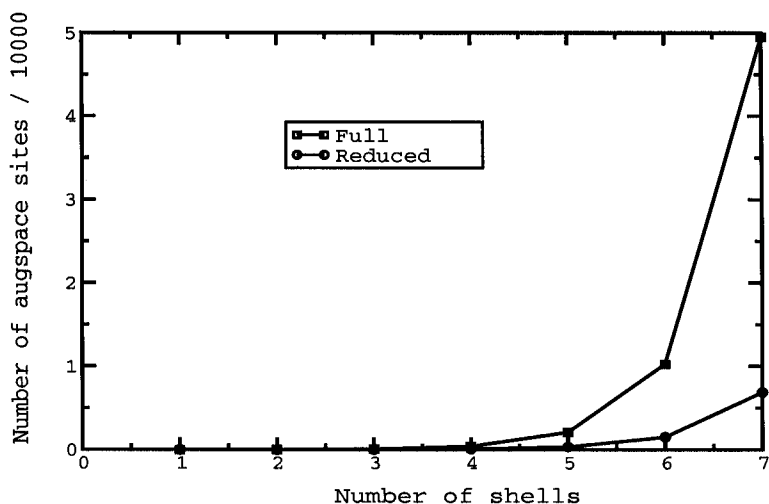


Figure 2.7: Showing how the number of lattice sites increase with increasing the number of shells in an augmented space map on a disordered binary alloy on a fcc lattice.

in this example. Such reduction will allow us to stretch our nearest-neighbour map up to 9-10 shells, stepping up our accuracy. Figure 2.8 shows the reduction in CPU time as we increase the number of recursion steps. Further, since the number of sites in the map decreases, the number of individual applications of the 9×9 Hamiltonian also decreases significantly, as do the number of operations involved in taking various inner products. This will reduce the inherent cumulative error of the recursion technique and lessen the probability of the appearance of *ghost bands* which often plague recursion calculations.

Table 2.3: Comparison between system size and time (in seconds) taken for recursion (using 15 seed points for $\text{Ag}_{50}\text{Pd}_{50}$) on a P4/256 machine for a full fcc lattice and the reduced lattice in augmented space. The model is that of an alloy whose constituents have only s states and the Hamiltonian for $\text{Ag}_{50}\text{Pd}_{50}$ is taken from a TB-LMTO minimal spd basis for each constituent.

System	Full lattice				Reduced lattice	
	Shells	Steps	Sites	CPU time	Sites	CPU time
Model (50-50)	7	7	49476	6.67	6856	1.21
$\text{Ag}_{50}\text{Pd}_{50}$	7	11	49476	1136.6	6856	336.27

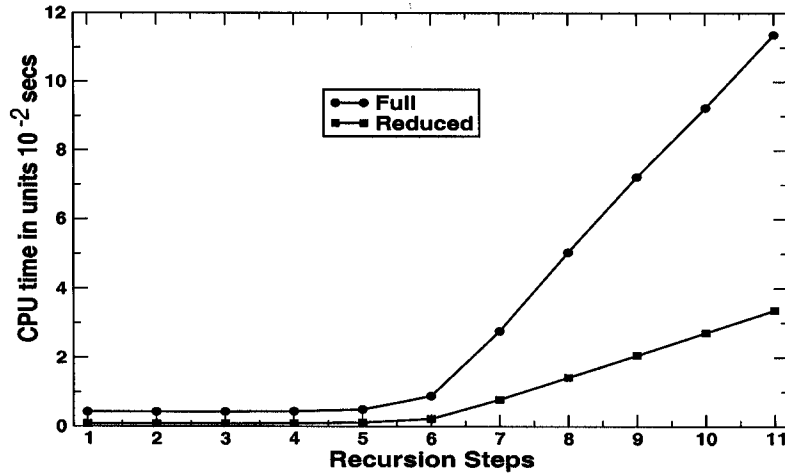


Figure 2.8: CPU time taken per recursion step for a $\text{Ag}_{50}\text{Pd}_{50}$ disordered binary alloy on a fcc lattice in a spd TB-LMTO minimal basis set. The times with and without symmetry reduction are shown.

2.3 Conclusions

To deal with disorder in real alloys, we have described the implementation of ASR within the framework of TB-LMTO method. The ASR with its terminator approximation works well going beyond the standard single-site mean-field theories. We have carried out the symmetry reduction in the ASR calculations using the symmetries of both the underlying lattice and orbitals on the lattice, and also symmetry of the random configurations on the lattice. Considering all these symmetries we keep recursion basis vectors in the irreducible subspace of the Hilbert space which helps to reduce the rank of the Hamiltonian in the augmented space. This symmetry reduction helps us to carry out recursion for many more steps exactly and this is required to get a proper termination of the continued fraction. In addition, the symmetry reduction saves the computer memory and reduces the computational time, which is very effective for a self-consistent calculations. In this chapter we have described the details of the implementation of this symmetry reduction and the modifications required in the standard recursion method. We propose using the symmetry reduced version of the augmented space recursion in our future work on disordered alloys.

Chapter 3

Augmented space recursion in reciprocal space

3.1 Introduction

The augmented space recursion carried out in a minimal basis set representation of the tight-binding linear muffin-tin orbitals method (TB-LMTO-ASR) has been proposed earlier by Saha *et al* 1994b, Saha *et al* 1996 as an interesting technique for incorporation of the effects of configuration fluctuations about the mean-field (the coherent potential approximation or the CPA) for random substitutionally disordered alloys. This can be achieved without the usual problems of violation of the Herglotz analytic properties ¹ of the approximated configuration-averaged Green functions for the Schrödinger equation for these random alloys. Earlier we had used this technique to look at short-ranged ordering in such systems (Mookerjee and Prasad 1993, Dasgupta *et al* 1995), as well as local lattice distortions caused by size difference between the constituents of the alloy (Saha and Mookerjee 1996).

One of the dissatisfying features of the method, and this has to do with the recursion part, is the truncation of the continued fraction expansion of the Green function. Truncation in the configuration space part of the problem can be handled easily. We truncate out only those configurations which occur with low probability and contribute to the tail of the continued fraction. It is on the truncation in real-space that we do not

⁰Part of this chapter has been accepted for publication : **K K Saha**, A Mookerjee and O Jepsen, *Phys. Rev. B* (2004); cond-mat/0405175.

¹A complex function $f(z)$ is called *Herglotz* if it is analytic everywhere except on the real z -axis and $\text{sgn}(\text{Im } f(z)) = -\text{sgn}(\text{Im}(z))$.

have a controllable handle. Any truncation in real-space means that our recursion has been carried out on a finite cluster and edge effects become important. Quantities which converge fast are integrals of the density of states multiplied by well-behaved functions of energy. We can also estimate the errors committed by truncating at a particular step (Chakrabarti and Mookerjee 2002). However, the errors in the density of states itself cannot be controlled. This is because even a small perturbation (like truncation after a large number of recursive steps) has a profound effect on the spectrum of the Hamiltonian (Haydock 1980). The problem of truncation has always been laid at the door of the recursion method.

Is it not possible to modify the TB-LMTO-ASR in such a way that the truncation is carried out only in configuration space ? One way of reducing the gigantic rank of the Hamiltonian in a real-space-labelled basis, is to go over to reciprocal-space. In the \mathbf{k} labelled basis, for a basis involving only s, p and d states, the operators in reciprocal-space have rank 9. However, to do this we require lattice translational symmetry. In a random binary alloy, for instance, this is not immediately possible. However, the full augmented space, which is the direct product of the real-space spanned by the site labelled basis $\{\underline{R}_i\}$ and the configuration space spanned by the configurations of the system, possesses translational as well as point group symmetries (Saha and Mookerjee 2004a). Configurations of a binary alloy can be labelled by a binary sequence of 0 and 1 (or \uparrow and \downarrow if Ising models appeal to you more) and uniquely described by the *cardinality sequence* $\{\mathcal{C}\}$, i.e. the sequence of positions where we have a 1 or a \downarrow state. We had shown earlier that in the subspace spanned by the reference states $\{\emptyset\}$, in which the configuration average is described, we have full lattice translation symmetry provided the disorder is homogeneous (Biswas *et al* 1995). The same statement would be true if there is short-ranged order or local lattice distortions, provided the short-ranged order or local lattice distortions are probabilistically identical anywhere in the system. A consequence of this is that probability densities are independent of the site label and the configuration-averaged quantity :

$$\sum_{R_i} \sum_{R_j} \exp \{i(\mathbf{k} \cdot R_i - \mathbf{k}' \cdot R_j)\} \ll \mathbf{G}(R_i, R_j, z) \gg = \mathbf{G}(\mathbf{k}, z) \delta(\mathbf{k} - \mathbf{k}')$$

Based on this, we had proposed a TB-LMTO-Recursion in the reciprocal augmented

space (Biswas *et al* 1997). The recursion, as we shall show subsequently, is entirely in configuration space for each \mathbf{k} label. The truncation is also in configuration space alone and leads to calculation of the configuration averaged spectral densities. These spectral densities are not a bunch of delta functions, as in the case of ordered systems, but the complex self-energies, in general both energy and \mathbf{k} dependent, shift the peaks as well as broaden them : leading to fuzzy, complex band structures.

Although our method allows us to carry our augmented space recursion in reciprocal space, for many physical problems we need to carry our integration over the Brillouin zone. For instance, to obtain the density of states :

$$\langle\langle n(E) \rangle\rangle = \int_{BZ} \frac{d^3\mathbf{k}}{8\pi^3} \text{Tr} \langle\langle \mathbf{A}(\mathbf{k}, E) \rangle\rangle$$

Another contribution of this work, described subsequently, will be to modify the tetrahedral method of Brillouin zone integration, so that we may carry out a similar integration technique for integrands which are smoother than the highly singular spectral functions of the ordered systems. The proposed Brillouin zone integration is closely related to that of Jepsen and Andersen 1971 or Lehmann and Taut 1972 for ordered systems.

3.2 Augmented space recursion in \mathbf{k} -space

We shall start from a first principles TB-LMTO method (Andersen 1975, Andersen and Jepsen 1984) in the most-localized representation (α representation). This is necessary, because recursion requires a sparse representation of the Hamiltonian. In this representation, the second order alloy Hamiltonian is given by

$$\mathbf{H}^{(2)} = \mathbf{E}_\nu + \mathbf{h} - \mathbf{h}\mathbf{o}\mathbf{h}$$

where

$$\begin{aligned} \mathbf{h} &= \sum_R (\mathbf{C}_R - \mathbf{E}_{\nu R}) \mathcal{P}_R + \sum_R \sum_{R'} \Delta_R^{1/2} \mathbf{S}_{RR'} \Delta_{R'}^{1/2} \mathcal{T}_{RR'} \\ \mathbf{o} &= \sum_R \mathbf{o}_R \mathcal{P}_R \end{aligned} \tag{3.1}$$

and $\mathbf{S}_{RR'}$ is a matrix of rank L_{\max} . \mathbf{C} , Δ and \mathbf{o} 's are diagonal in L space and are the potential parameters of the TB-LMTO method; \mathbf{o}^{-1} has dimension of energy and \mathbf{E}_ν 's are the reference energies about which the muffin-tin orbitals are linearized.

Applying the augmented space theorem as in equations (2.1)-(2.3) the configuration-averaged Green function becomes :

$$\ll \mathbf{G}(\mathbf{k}, z) \gg = \langle \mathbf{k} \otimes \{\emptyset\} | (z\tilde{\mathbf{I}} - \tilde{\mathbf{H}}^{(2)})^{-1} | \mathbf{k} \otimes \{\emptyset\} \rangle. \quad (3.2)$$

where \mathbf{G} and $\mathbf{H}^{(2)}$ are operators which are matrices in angular momentum space, and the augmented \mathbf{k} -space basis $|\mathbf{k}, L \otimes \{\emptyset\}\rangle$ has the form

$$(1/\sqrt{N}) \sum_R \exp(-i\mathbf{k} \cdot R) |R \otimes \{\emptyset\}\rangle.$$

The augmented space Hamiltonian $\tilde{\mathbf{H}}^{(2)}$ is constructed from the TB-LMTO Hamiltonian $\mathbf{H}^{(2)}$ by replacing each random variable n_R by operators \mathbf{M}_R .

If we now follow the same mathematical manipulations as in the augmented space recursion in real-space (equations (2.2)-(2.5)) we obtain :

$$\ll \mathbf{G}(\mathbf{k}, z) \gg = \langle 1 | (z\tilde{\mathbf{I}} - \tilde{\mathbf{A}} + \tilde{\mathbf{B}} + \tilde{\mathbf{F}} - \tilde{\mathbf{S}} + (\tilde{\mathbf{J}} + \tilde{\mathbf{S}}) \tilde{\mathbf{o}} (\tilde{\mathbf{J}} + \tilde{\mathbf{S}}))^{-1} | 1 \rangle$$

where

$$\begin{aligned} \tilde{\mathbf{A}} &= \sum_R \left\{ \mathbf{A}(\mathbf{C}\Delta^{-1})/\mathbf{A}(\Delta^{-1}) \right\} \mathcal{P}_R \otimes \mathcal{I} \\ \tilde{\mathbf{B}} &= \sum_R \left\{ \mathbf{B}((z\mathbf{I} - \mathbf{C})\Delta^{-1})/\mathbf{A}(\Delta^{-1}) \right\} \mathcal{P}_R \otimes \mathcal{P}_R^\downarrow \\ \tilde{\mathbf{F}} &= \sum_R \left\{ \mathbf{F}((z\mathbf{I} - \mathbf{C})\Delta^{-1})/\mathbf{A}(\Delta^{-1}) \right\} \mathcal{P}_R \otimes \left\{ \mathcal{T}_R^{\uparrow\downarrow} + \mathcal{T}_R^{\downarrow\uparrow} \right\} \end{aligned} \quad (3.3)$$

and $\tilde{\mathbf{J}} = \tilde{\mathbf{J}}_A + \tilde{\mathbf{J}}_B + \tilde{\mathbf{J}}_F$ and $\tilde{\mathbf{o}} = \tilde{\mathbf{o}}_A + \tilde{\mathbf{o}}_B + \tilde{\mathbf{o}}_F$ where :

$$\begin{aligned} \tilde{\mathbf{J}}_A &= \sum_R \left\{ \mathbf{A}((\mathbf{C} - \mathbf{E}_\nu)\Delta^{-1})/\mathbf{A}(\Delta^{-1}) \right\} \mathcal{P}_R \otimes \mathcal{I} \\ \tilde{\mathbf{J}}_B &= \sum_R \left\{ \mathbf{B}((\mathbf{C} - \mathbf{E}_\nu)\Delta^{-1})/\mathbf{A}(\Delta^{-1}) \right\} \mathcal{P}_R \otimes \mathcal{P}_R^\downarrow \\ \tilde{\mathbf{J}}_F &= \sum_R \left\{ \mathbf{F}((\mathbf{C} - \mathbf{E}_\nu)\Delta^{-1})/\mathbf{A}(\Delta^{-1}) \right\} \mathcal{P}_R \otimes \left\{ \mathcal{T}_R^{\uparrow\downarrow} + \mathcal{T}_R^{\downarrow\uparrow} \right\} \end{aligned}$$

$$\begin{aligned}
\tilde{\mathbf{o}}_{\mathbf{A}} &= \sum_R \{ \mathbf{A}(\mathbf{o}\Delta) \mathbf{A}(\Delta^{-1}) \} \mathcal{P}_R \otimes \mathcal{I} \\
\tilde{\mathbf{o}}_{\mathbf{B}} &= \sum_R \{ \mathbf{B}(\mathbf{o}\Delta) \mathbf{A}(\Delta^{-1}) \} \mathcal{P}_R \otimes \mathcal{P}_R^\dagger \\
\tilde{\mathbf{o}}_{\mathbf{F}} &= \sum_R \{ \mathbf{F}(\mathbf{o}\Delta) \mathbf{A}(\Delta^{-1}) \} \mathcal{P}_R \otimes \{ \mathcal{T}_R^{\uparrow\downarrow} + \mathcal{T}_R^{\downarrow\uparrow} \}.
\end{aligned} \tag{3.4}$$

In case there is no off-diagonal disorder due to local lattice distortion because of size mismatch :

$$\tilde{\mathbf{S}} = \sum_R \sum_{R'} \mathbf{A}(\Delta_R^{-1})^{-1/2} \mathbf{S}_{RR'} \mathbf{A}(\Delta_{R'}^{-1})^{-1/2} \mathcal{T}_{RR'} \otimes \mathcal{I}.$$

This equation is now exactly in the form in which recursion method may be applied. At this point we note that the above expression for the averaged $G_{LL}(\mathbf{k}, z)$ is exact.

The recursion method addresses inversions of infinite matrices (Haydock 1981, Haydock and Te 1994). Once a sparse representation of an operator in Hilbert space, $\widetilde{\mathbf{H}}^{(2)}$, is known in a countable basis, the recursion method obtains an alternative basis in which the operator becomes tridiagonal. This basis and the representations of the operator in it are found recursively through a three-term recurrence relation :

$$|u_{n+1}\rangle = \widetilde{\mathbf{H}}^{(2)}|u_n\rangle - \alpha_n(\mathbf{k})|u_n\rangle - \beta_n^2(\mathbf{k})|u_{n-1}\rangle \tag{3.5}$$

with the initial choice $|u_1\rangle = |RL\rangle \otimes |1\rangle$ and $\beta_1^2 = 1$. The recursion coefficients α_n and β_n are real and are obtained by imposing the ortho-normalizability condition of the new basis set as :

$$\alpha_n(\mathbf{k}) = \frac{\{n|\widetilde{\mathbf{H}}^{(2)}|n\rangle}{\{n|n\rangle} ; \quad \beta_{n-1}^2(\mathbf{k}) = \frac{\{n-1|\widetilde{\mathbf{H}}^{(2)}|n\rangle}{\{n|n\rangle}$$

$$\text{and also } \{m|\widetilde{\mathbf{H}}^{(2)}|n\rangle = 0 \text{ for } m \neq n, n \pm 1$$

To obtain the spectral function we first write the configuration-averaged L -projected Green functions as continued fractions :

$$\begin{aligned}
\ll G_{LL}(\mathbf{k}, z) \gg &= \frac{\beta_{1L}^2}{z - \alpha_{1L}(\mathbf{k}) - \frac{\beta_{2L}^2(\mathbf{k})}{z - \alpha_{2L}(\mathbf{k}) - \frac{\beta_{3L}^2(\mathbf{k})}{\ddots}}} \\
&\quad \frac{\beta_{NL}^2(\mathbf{k})}{z - \alpha_{NL}(\mathbf{k}) - \Gamma_L(\mathbf{k}, z)}
\end{aligned}$$

where $\Gamma_L(\mathbf{k}, z)$ is the asymptotic part of the continued fraction. The approximation involved has to do with the termination of this continued fraction. The coefficients are calculated exactly up to a finite number of steps $\{\alpha_n, \beta_n\}$ for $n < N$ and the asymptotic part of the continued fraction is obtained from the initial set of coefficients using the idea of Beer and Pettifor terminator (Beer and Pettifor 1982) as described in chapter 1.

It is important to note that the operators $\tilde{\mathbf{A}}, \tilde{\mathbf{B}}, \tilde{\mathbf{F}}$ are all projection operators in real-space (i.e. unit operators in \mathbf{k} -space) and acts on an augmented space basis only to change the configuration part (i.e. the cardinality sequence $\{\mathcal{C}\}$).

$$\begin{aligned}\tilde{\mathbf{A}}|\{\mathcal{C}\}\rangle &= A_1|\{\mathcal{C}\}\rangle, \\ \tilde{\mathbf{B}}|\{\mathcal{C}\}\rangle &= A_2|\{\mathcal{C}\}\rangle \delta(R \in \{\mathcal{C}\}), \\ \tilde{\mathbf{F}}|\{\mathcal{C}\}\rangle &= A_3|\{\mathcal{C} \pm R\}\rangle.\end{aligned}$$

The coefficients $A_1 - A_3$ can be expressed from equation (3.3). Similar expressions hold for the operators in equation (3.4). The remaining operator $\tilde{\mathbf{S}}$ is diagonal in \mathbf{k} -space and acts on an augmented space only to change the configuration part :

$$\tilde{\mathbf{S}}|\{\mathcal{C}\}\rangle = \sum_{\chi} \exp(-i\mathbf{k}\cdot\chi)|\{\mathcal{C} - \chi\}\rangle. \quad (3.6)$$

Here χ s are the nearest-neighbour vectors. The operation of the effective Hamiltonian is thus entirely in the configuration space and the calculation does not involve the space \mathcal{H} at all. This is an enormous simplification over the standard augmented space recursion described earlier (Saha *et al* 1994b, Saha *et al* 1996, Dasgupta *et al* 1997, Ghosh *et al* 1999), where the entire reduced real space part as well as the configuration part was involved in the recursion process. Earlier we had to resort to symmetry reduction of this enormous space in order to make the recursion tractable. Here the rank of only the configuration space is much smaller and we may further reduce it by using the local symmetries of the configuration space, as described in previous chapter. However, this advantage is offset by the fact that the effective Hamiltonian is energy dependent. This means that to obtain the Green functions we have to carry out the recursion for each energy point. This process is simplified by carrying out recursion over a suitably chosen set of *seed energies* and interpolating the values of the coefficients across the band.

3.3 Spectral density and fuzzy bands

The self-energy which arises because of scattering by the random potential fluctuations is of the form :

$$\Sigma_L(\mathbf{k}, z) = \frac{\beta_{2L}^2(\mathbf{k})}{z - \alpha_{2L}(\mathbf{k}) - \frac{\beta_{3L}^2(\mathbf{k})}{\ddots}} \frac{\beta_{3L}^2(\mathbf{k})}{z - \alpha_{NL}(\mathbf{k}) - \Gamma_L(\mathbf{k}, z)}$$

So the continued fraction can be written in the form $1/(z - \tilde{E}_L(\mathbf{k}) - \Sigma_L(\mathbf{k}, E))$, where $\tilde{E}_L(\mathbf{k}) = \alpha_{1L}(\mathbf{k})$.

The average spectral function $\ll A_{\mathbf{k}}(E) \gg$ is related to the averaged Green function in reciprocal-space as :

$$\ll A_{\mathbf{k}}(E) \gg = \sum_L \ll A_{\mathbf{k}L}(E) \gg,$$

where

$$\ll A_{\mathbf{k}L}(E) \gg = -\frac{1}{\pi} \lim_{\delta \rightarrow 0^+} \{\text{Im} \ll G_{LL}(\mathbf{k}, E - i\delta) \gg\}.$$

To obtain the complex bands for the alloy we fix a value for \mathbf{k} and solve for :

$$z - \tilde{E}_L(\mathbf{k}) - \Sigma_L(\mathbf{k}, E) = 0$$

The real part of the roots will give the position of the bands, while the imaginary part of roots will be proportional to the lifetime. Since the alloy is random, the bands always have finite lifetimes and are fuzzy.

3.4 Generalized tetrahedron method integration in k-space

To obtain the density of states we need to integrate over the Brillouin zone

$$\ll n(E) \gg = \sum_L \int_{BZ} \frac{d^3\mathbf{k}}{8\pi^3} \ll A_{\mathbf{k}L}(E) \gg \quad (3.7)$$

For ordered systems the spectral function consists of delta functions : $A_{\mathbf{k}}^0(E) = \sum_j A_j \delta(E - E_j(\mathbf{k}))$, with j labeling a particular energy band. The integrand being highly singular, the integral (3.7) has to be calculated carefully. Jepsen and Andersen

1971 and Lehmann and Taut 1972 had proposed an accurate technique : the tetrahedron method, for obtaining such integrals accurately. In this section we shall discuss an extension of that method for application to disordered systems.

In the presence of disorder the spectral function is smoother and we may rewrite it in terms of the real and imaginary parts of the disorder induced self-energy :

$$\ll A_{\mathbf{k}L}(E) \gg = \frac{-\Sigma_L^I(\mathbf{k}, E)/\pi}{(E - \tilde{E}_L(\mathbf{k}) - \Sigma_L^R(\mathbf{k}, E))^2 + \Sigma_L^I(\mathbf{k}, E)^2} \quad (3.8)$$

Such a function is peaked around the zeroes of $E - \tilde{E}_L(\mathbf{k}) - \Sigma_L^R(\mathbf{k}, E)$ and the $\Sigma_L^I(\mathbf{k}, E)$ provides the width of the peaks. The spectral function behaves roughly as *Lorentzian* in the vicinity of its peaks. We may reduce the above expression to one amenable to the tetrahedron integration form by the following trick :

$$\begin{aligned} &= \int dE' \frac{-\Sigma_L^I(\mathbf{k}, E)/\pi}{(E - E' - \Sigma_L^R(\mathbf{k}, E))^2 + \Sigma_L^I(\mathbf{k}, E)^2} \delta(E' - \tilde{E}_L(\mathbf{k})) \\ &= \int dE' \mathcal{W}_{\mathbf{k}L}(E, E') \delta(E' - \tilde{E}_L(\mathbf{k})) \end{aligned}$$

where $\mathcal{W}_{\mathbf{k}L}$ is defined as a *weight function*. Now integrating above over the Brillouin zone, we may get configuration-averaged density of states (DOS) :

$$\begin{aligned} \ll n(E) \gg &= \sum_L \int_{BZ} \frac{d^3\mathbf{k}}{8\pi^3} \ll A_{\mathbf{k}L}(E) \gg \\ &= \sum_L \int dE' \int_{BZ} \frac{d^3\mathbf{k}}{8\pi^3} \mathcal{W}_{\mathbf{k}L}(E, E') \delta(E' - \tilde{E}_L(\mathbf{k})) \end{aligned}$$

At this stage, in order to simplify notation we shall drop the L index from all L dependent factors and understood that the eventual result is summed over all L . In order to perform the above integration over BZ, we have generalized *tetrahedron method* developed by Jepsen and Andersen 1971 and Lehmann and Taut 1972 to include the weight function $\mathcal{W}_{\mathbf{k}}(E, E')$. We have followed the idea of MacDonald *et al* 1979. In this generalization the energies as well as the weight functions are linearly interpolated throughout the vertices of small tetrahedrons. We label the energies at the vertices of the i th tetrahedron $\tilde{E}_1^i, \tilde{E}_2^i, \tilde{E}_3^i$ and \tilde{E}_4^i , where the indices correspond to increasing magnitude

of the energy, i.e. $\tilde{E}_1^i \geq \tilde{E}_2^i \geq \tilde{E}_3^i \geq \tilde{E}_4^i$ and the corner values of the weight function be $\mathcal{W}_1^i, \mathcal{W}_2^i, \mathcal{W}_3^i$ and \mathcal{W}_4^i . Then the averaged DOS may be written as :

$$\ll n(E) \gg = V_{MZ} \int dE' \sum_{i=1}^N C^i \sum_{k=1}^4 I_k^i \mathcal{W}_k^i \quad (3.9)$$

where $I_k^i = I_k(E, E', \tilde{E}_1^i, \tilde{E}_2^i, \tilde{E}_3^i, \tilde{E}_4^i)$, N is the number of tetrahedral micro-zones and V_{MZ} is the micro-zone volume and also,

for $\tilde{E}_1^i < E' \leq \tilde{E}_2^i$

$$\begin{aligned} C^i &= 3 F_{21} F_{31} F_{41} / (E' - \tilde{E}_1) \\ I_1^i &= (F_{12} + F_{13} + F_{14}) / 3 \\ I_k^i &= F_{k1} / 3, \quad k = 2, 3, 4. \end{aligned}$$

for $\tilde{E}_2^i < E' \leq \tilde{E}_3^i$

$$\begin{aligned} C^i &= 3 (F_{23} F_{31} + F_{32} F_{24}) / E_{41} \\ I_1^i &= F_{14} / 3 + F_{13} F_{31} F_{23} / C^i E_{41} \\ I_2^i &= F_{23} / 3 + F_{24}^2 F_{32} / C^i E_{41} \\ I_3^i &= F_{32} / 3 + F_{31}^2 F_{23} / C^i E_{41} \\ I_4^i &= F_{41} / 3 + F_{42} F_{24} F_{32} / C^i E_{41} \end{aligned}$$

for $\tilde{E}_3^i < E' \leq \tilde{E}_4^i$

$$\begin{aligned} C^i &= 3 F_{14} F_{24} F_{34} / (\tilde{E}_4 - E') \\ I_k^i &= F_{k4} / 3, \quad k = 1, 2, 3 \\ I_4^i &= (F_{41} + F_{42} + F_{43}) / 3 \end{aligned}$$

where $E_{mn} = \tilde{E}_m - \tilde{E}_n$ and $F_{mn} = (E' - \tilde{E}_n) / E_{mn}$. Also $\ll n(E) \gg$ is zero for $E' \leq \tilde{E}_1^i$ or $E' \geq \tilde{E}_4^i$.

3.5 Computational details and results

For ordered faces the calculations have been performed in the basis of LMTO in the atomic sphere approximation including combined corrections. The scalar-relativistic calculations

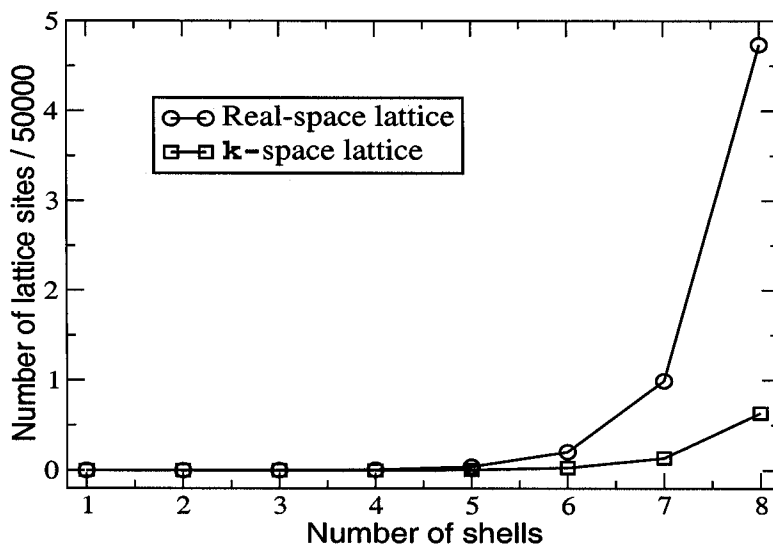


Figure 3.1: Showing how the number of lattice sites increase with increasing the number of shells in the real-space and reciprocal-space map.

in this case are carried out for equal atomic spheres. The \mathbf{k} -space integration was carried out with $16 \times 16 \times 16$ mesh resulting 145 k -points for cubic primitive structure in the irreducible part of the Brillouin zone.

In figure 3.1 shows how the size of the augmented space map (in both \mathbf{k} -space and real-space representation) increases as we increase the number of nearest-neighbour shells from a starting site. We note that the reciprocal-space map at a particular recursion step is much smaller than the real augmented space map. This is because in the reciprocal augmented space we generate only the different configurations. The full real-space lattice map has been collapsed using lattice translational symmetry in full augmented space.

We have first carried out calculations on a simple model disordered binary alloy system described by a s -state tight-binding Hamiltonian with nearest-neighbour hopping integrals only.

In figure 3.2 we compare the results obtained using reciprocal and real space formulation of ASR. The \mathbf{k} -space integration has been performed in two ways. The brute force method, where we replace the integral by a sum with appropriate weights at different \mathbf{k} -points, generates some unusual oscillations particularly in the lower part of the band.

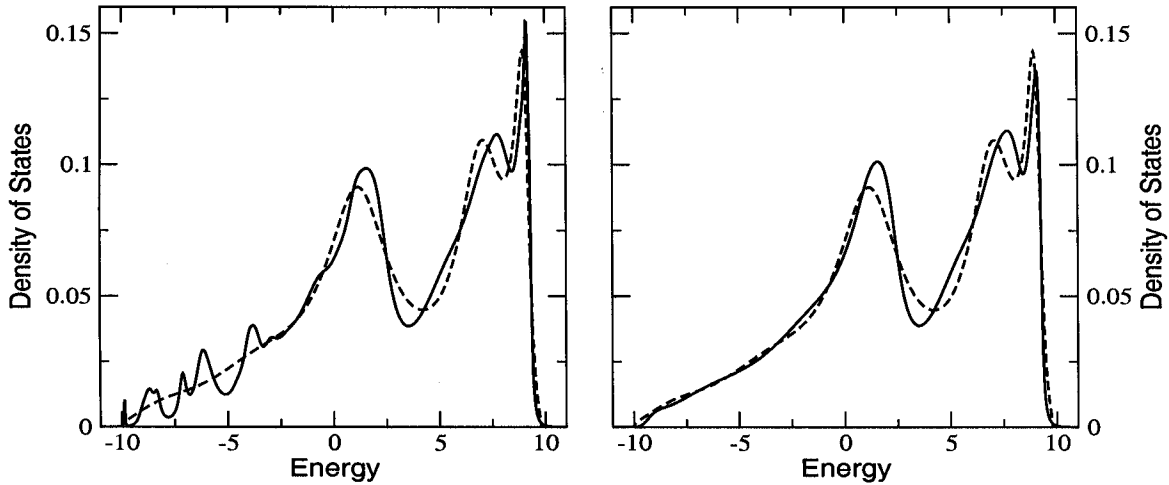


Figure 3.2: Comparison of the average (50-50) density of states for a model fcc alloy calculated using \mathbf{k} -space formulation of ASR (solid curve) and using real-space formulation of ASR (dotted curve). \mathbf{k} -space integration has been performed in two ways : (a) using Tetrahedron Method (right solid curve) (b) multiplying spectral function $A_k(E)$ by k -point weight and then summing up over k (left solid curve). In both figures we note that the oscillations shown by the brute force technique is smoothed by the TM.

However, the tetrahedron method gives smoother results which are in good agreement with the real-space calculations as well.

We now go over to calculations for the disordered $\text{Ni}_{50}\text{Pt}_{50}$ alloy. We have used the minimal basis set of the TB-LMTO with nine orbitals per atom (s, p and d) to set up our Hamiltonian.

In figure 3.3 we present the results for the spectral functions for $\text{Ni}_{50}\text{Pt}_{50}$ alloy along the $\Gamma - X$ direction. We have chosen 11 equidistant k -points between Γ and X points and show the spectral function in those points. These spectral functions shows good agreement with the same results obtained from KKR-CPA calculations (Pinski *et al* 1991). It may be seen that the widths of the spectral function varies considerably as a function of \mathbf{k} and E . There are some simple trends concerning this behaviour. The sharp peaks on the lower band edge near the Γ point appear as the s-like band. As we go from Γ towards the X point the s-band hybridizes with the p-band and the peak becomes wider. The structures on the upper band edges are mostly due to the overlap of the d-states of Ni and

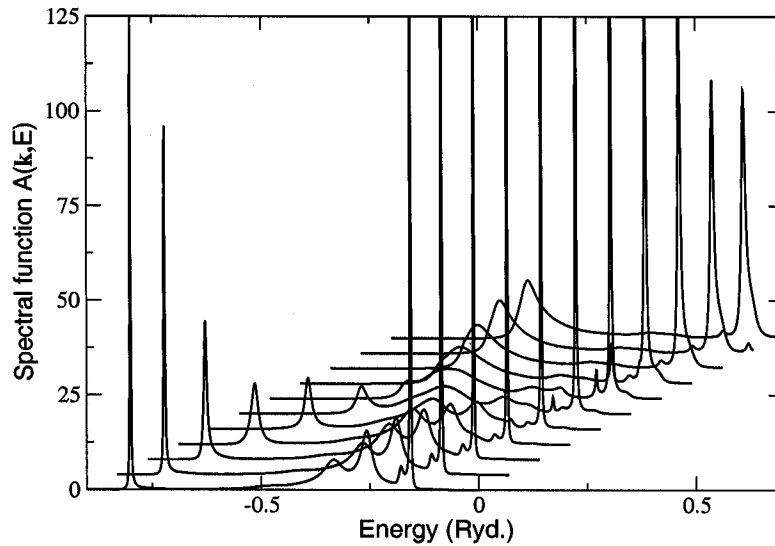


Figure 3.3: The spectral function of $\text{Ni}_{50}\text{Pt}_{50}$ alloy plotted as a function of energy at several \mathbf{k} -points along the $\Gamma - X$ direction:

Pt. The disorder effects on these d-dominated states are strong and there is significant broadening.

In figure 3.4 we presented the complex fuzzy bands of the disordered alloy. The disorder smearing is maximum in the overlapping d-bands of the constituents, and is negligible in the s-like part. This is also apparent in the spectral functions shown earlier. The sharp s-like peaks flank wide d-like structures in figure 3.3.

Finally, using our modified tetrahedron method we have calculated the density of states (DOS) of ordered and homogeneous disordered NiPt alloys from its spectral function. Side by side we have also carried out the same calculation in real augmented space. In figure 3.5 we show the ℓ -projected density of states for the $\text{Ni}_{50}\text{Pt}_{50}$ alloy. We compare the \mathbf{k} -space results with those found from real-space recursion. The main improvement occurs in the e_g and t_{2g} d-bands. In particular, the sharp feature straddling the Fermi energy is better reproduced in the \mathbf{k} -space recursion than that in real-space. The reason for this is the early truncation of recursion in real-space and the consequent finite size effects to which the more localized d-states are more susceptible.

In figure 3.6 (top row) we show a comparison between average DOS calculated by real

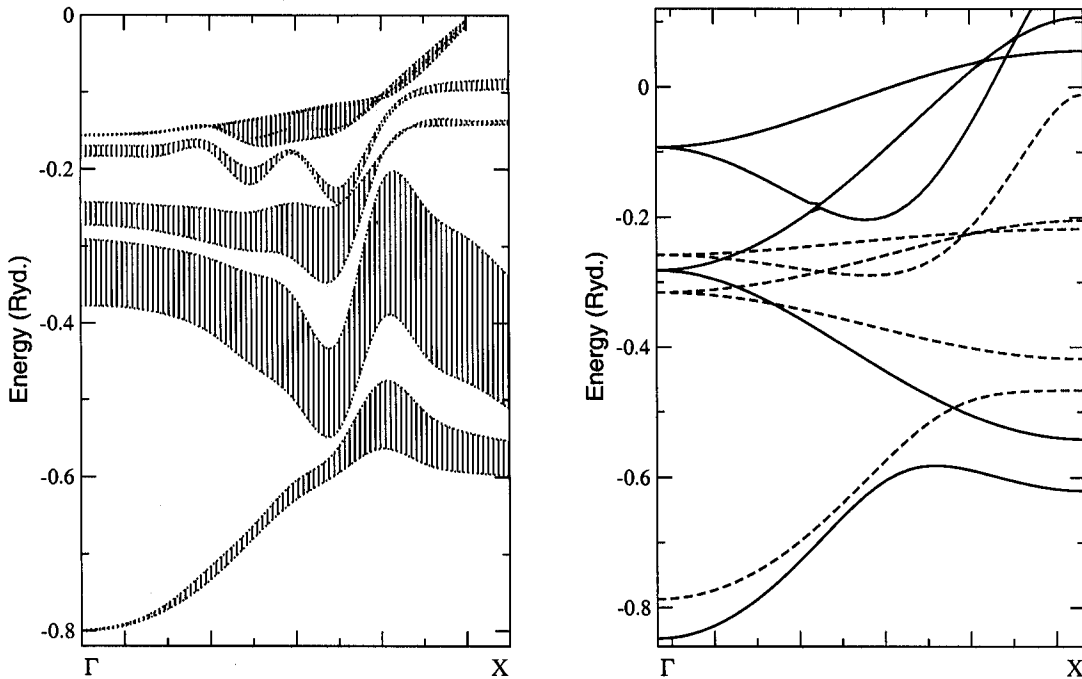


Figure 3.4: (Right) Ni (dashed lines) and Pt (bold lines) energy bands on a lattice appropriate to the $\text{Ni}_{50}\text{Pt}_{50}$ alloy, in the $\Gamma-X$ direction. Average lattice parameter $a_0 = 7.127a_u$ was fixed after minimizing the energy. (Left) The fuzzy band of the disordered $\text{Ni}_{50}\text{Pt}_{50}$ system plotted along the same direction.

and reciprocal-space recursions. As discussed before, it is the sharp feature straddling the Fermi energy with major contribution coming from the Ni d-states which are not well reproduced in the real-space technique. In this point our \mathbf{k} -space calculations agree with the KKR-CPA results of Pinski *et al* 1991. In the left lower panel of figure 3.6 we show the DOS for pure Ni and Pt, but in a lattice with the lattice parameter the same as in the alloy. We may compare this with the DOS for the disordered alloy. The right most three peaks at -0.25, -0.16 and -0.11 Ryd. of the disordered DOS are mostly contributed by Ni whereas the left (lower energy) structures come (large shoulder at -0.57 Ryd.) mostly from Pt. The sharp peaks in the elemental results are obviously because of the Van Hove singularities of the DOS. The effect of disorder mainly smears out the sharp peaks present in the DOS. The disorder smearing is more pronounced for the d-like parts of the band. We remark that there is very little shift in the DOS-related features between the ordered

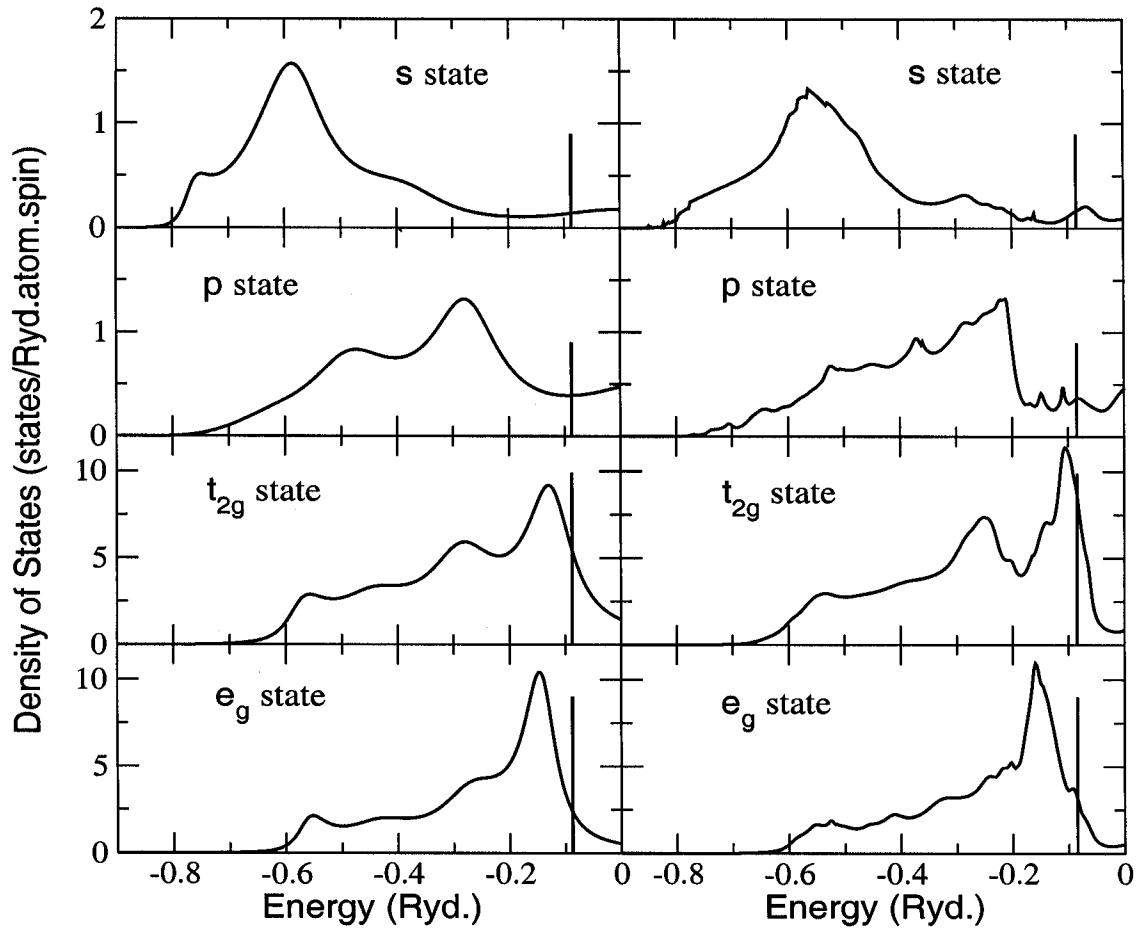


Figure 3.5: Comparison of the partial density of states of $\text{Ni}_{50}\text{Pt}_{50}$ alloy calculated using augmented space recursion in (a) real-space formulation (left panel). (b) \mathbf{k} -space formulation (right panel).

and disordered states.

Finally, in the right lower panel we show the photoemission spectrum of $\text{Ni}_{50}\text{Pt}_{50}$ reported by Nahm *et al* 1996. The general features with a double peak straddling the Fermi energy and a lower energy shoulder are clearly seen. The photoemission spectra are convolutions of the density of states with a weakly energy/wavenumber dependent transition matrix. This may lead to shifting and smearing of the prominent peak structures. Keeping this in mind, our \mathbf{k} -space recursion results are in good agreement with experiment.

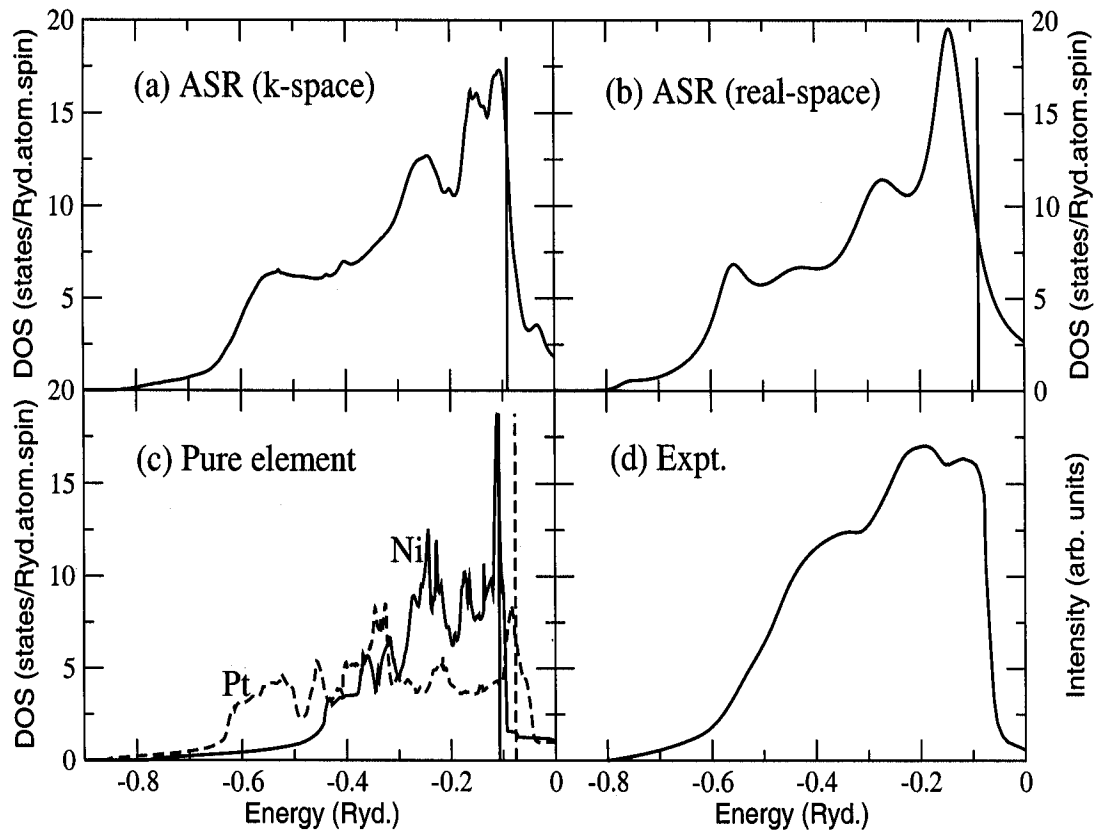


Figure 3.6: Comparison of the density of states of the $\text{Ni}_{50}\text{Pt}_{50}$ alloy calculated using augmented space recursion in (a) \mathbf{k} -space formulation. (b) real-space formulation. (c) Density of states of Ni (solid line) and Pt (dotted line) on a lattice appropriate to the $\text{Ni}_{50}\text{Pt}_{50}$ alloy. (d) Valence-band photo-emission spectra of $\text{Ni}_{50}\text{Pt}_{50}$ with photon energy $h\nu = 60$ (Nahm *et al* 1996).

3.6 Parallelization of codes

As a programmer, we may find that we need to solve ever longer, more memory intensive problems, or simply solve problems with greater speed than is possible on a serial computer. We can turn to parallel computers to satisfy these needs. Using parallel programming methods on parallel computers gives us access to greater memory and Central Processing Unit (CPU) resources not available on serial computers. Hence, we are able to solve large problems that may not have been possible otherwise, as well as solve problems more quickly.

The ASR in its reciprocal-space formulation requires a huge computational time as well as memory space. In the irreducible part of the Brillouin zone of a cubic primitive structured system, we have considered $16 \times 16 \times 16$ mesh which results 145 \mathbf{k} -points. For each angular momentum index, we needed to calculate spectral functions at these \mathbf{k} -points. In order to carry out a calculation on a real alloy system, a serial program required a very long time. We have, therefore, parallelized our codes, leading to faster computation.

Before going into the details of parallelization of our code, let us first clear our ideas about the structure of the ASR program on a serial computer. In the figure 3.7 (left panel) we have shown a brief flowchart of the \mathbf{k} -space formulation of the ASR code. As you see in the flowchart, the code has basically three loops : angular momentum loop, \mathbf{k} -point loop and energy loop. For a given L and \mathbf{k} , the innermost loop calculates the spectral functions $A_{\mathbf{k}L}(E)$ at all energy points. Once the calculation of $A_{\mathbf{k}L}(E)$ for all \mathbf{k} -points is over, we have to carry out a Brillouin zone integration to get the projected density of states.

In the right column of the same figure we have shown the schematic diagrams of the parallel codes. In our Beowulf Cluster system we have 10 nodes, each of them is a dual Xeon 2.4 Ghz processor, with 2 GB RAM. So we use any of these processors as a master and rest of them (i.e. 39 processors) as slaves. The job in the innermost loop (put in a dotted box in the flowchart) is shared by the slaves. We shall now describe the structure of the parallel codes, and the way it runs in the following steps :

- Master broadcast (MPI.BCAST) a copy of the initial inputs (for example, augmented space map, potential file, energy points, \mathbf{k} -points data, etc.) to all slaves in a group.
- For a given L (angular-momentum index) master sends (MPI.SEND) 39 \mathbf{k} -points to 39-slaves one by one.
- Slaves receive (MPI.RECV) jobs from master, carry out recursion in all seed energy points, fit the recursion coefficients along the energy spectrum, then calculate spectral function $A_{\mathbf{k}L}(E)$, and finally feedback output to the master.

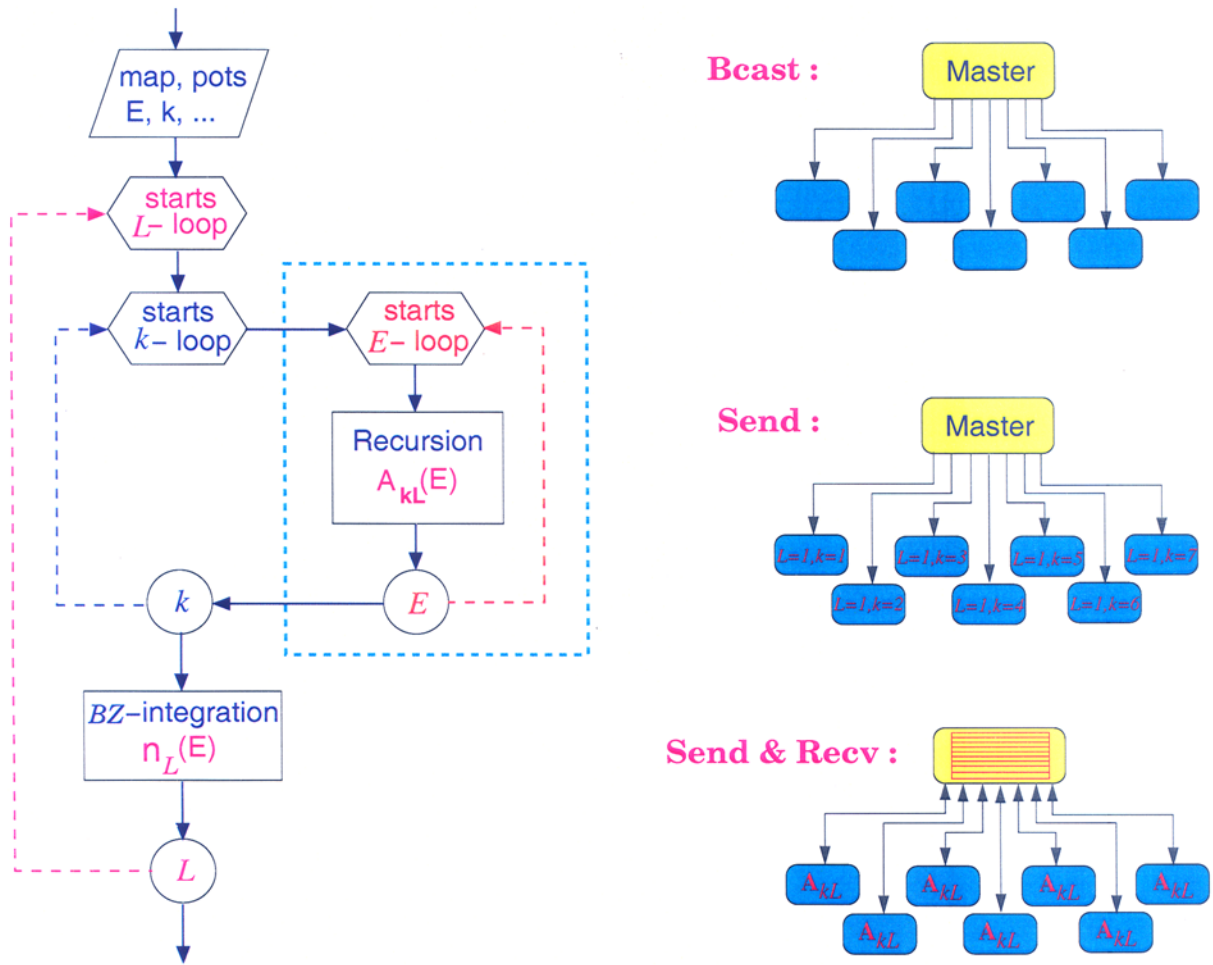


Figure 3.7: Flowchart of the augmented space recursion method (left) and schematic flowchart for parallelization of the same code (right).

- When master receives output $A_{kL}(E)$ from different slaves, it does not ensure that the output will come in the same order as master passed input to slaves. Because all the slaves may not be equally efficient. Any of them may be busy with some other job submitted by another person. So while receiving output master also receives the k -point at which the $A_{kL}(E)$ has been calculated. In this way master always keeps track of the input and output. Master always allocates some memory space to keep the outputs coming from different slaves.
- As soon as master receives an output from a slave immediately it gives it a new job

for another \mathbf{k} -point.

- Once all the jobs for all \mathbf{k} -points are completed, that is, all the spectral functions in all energy and \mathbf{k} -points are ready, master itself carry out the \mathbf{k} -space integration to calculate the projected (at the given L) density of states. During this integration the slaves need to wait for a few moments to get a new job for next L .
- Once the jobs for the projected DOS are being carried out, master sends some information to all the slaves to finalize (MPI_FINALIZE) themselves, that is, to ask them to stop running.

We have checked out the total time that is required to run this ASR code for a calculation on real material using both serial and parallel codes. To calculate each projected DOS of NiPt (50-50) alloy the serial computer needs around 18 hrs whereas the parallel machine (using 32 processors) reduces the time to only around 48 minutes !

3.7 Conclusion

We have presented an augmented space recursion formulation in reciprocal-space. We also present a generalization of the tetrahedron method proposed by Jepsen and Andersen 1971 for inverting the spectral functions to obtain the density of states. This technique will be useful for carrying of Brillouin zone integrals for disordered alloys. We have studied both a model alloy and NiPt. We have shown that the reciprocal-space calculation gives much better result than in real-space. This is because, in reciprocal-space formulation we really work with an infinite solids. The alloy NiPt was chosen since it has a sharp structure straddling the Fermi energy and therefore is a sensitive test for the accuracy of our technique. Finally, in order to accelerate the computation we have developed a parallel code (MPI program) feasible to a Beowulf cluster machine.

Chapter 4

Block recursion and Green matrices

4.1 Block recursion

Augmented space recursion carried out in a minimal basis set representation of the tight-binding linear muffin-tin orbitals method (TB-LMTO-ASR) has been proposed earlier (Saha *et al* 1994b, Saha *et al* 1996) as a technique for the incorporation of the effects of configuration fluctuations for random substitutionally disordered alloys. This can be achieved without the usual problems of violation of the Herglotz analytic properties of the approximated configuration-averaged Green functions for the Schrödinger equation for these random alloys. Although our initial focus was on configuration averages of the density of states and spectral functions, recently we have proposed using the TB-LMTO-ASR for the study of configuration-averaged optical conductivities (Saha and Mookerjee 2004b) or coherent and incoherent neutron scattering cross-sections (Alam and Mookerjee 2004b). These calculations require the full Green matrices in angular momentum space and not only their diagonal elements. We propose here the use of a generalization of the recursion method of Haydock *et al* 1972. The block recursion technique had been introduced earlier by Godin and Haydock 1988, 1992 in the very different context for obtaining the scattering S-matrix for finite scatterers attached to perfect leads. It has been discussed in a general context by Nex 1989 and Haydock *et al* 2004. Earlier, Inoue and Ohta 1987 had proposed the use of an orbital symmetrized version of the block recursion method for electronic structure calculations. We shall borrow their ideas and set up a

⁰Part of this chapter has been accepted for publication in : K K Saha and A Mookerjee, *J. Phys.: Condens. Matter* (2004).

block recursion in angular momentum space (rather than the lead space, as in Godin and Haydock's work) in order to obtain the Green matrices (in angular momentum space) directly. Unlike in the earlier works, the application will be to configuration averages in random alloys.

The need to develop the block recursion will become evident when we attempt to calculate the response functions in random alloys. Let us, in anticipation, quote here the result for the dominant term in the configuration-averaged current-current correlation function which will be discussed in the following two chapters (Saha and Mookerjee 2004b). This correlation function is directly related to the optical conductivity. We note that the expression involves the full Green matrix in angular momentum space and not only its diagonal elements.

The expression for correlation function is

$$\ll \mathcal{S}(z_1, z_2) \gg = \int_{\text{BZ}} \frac{d^3\mathbf{k}}{8\pi^3} \text{Tr} \left[\mathbf{J}^{\text{eff}}(\mathbf{k}, z_1, z_2) \ll \mathbf{G}^v(\mathbf{k}, z_1) \gg \mathbf{J}^{\text{eff}}(\mathbf{k}, z_1, z_2)^\dagger \ll \mathbf{G}^c(\mathbf{k}, z_2) \gg \right] \quad (4.1)$$

and the renormalized current term is given by :

$$\begin{aligned} \mathbf{J}^{\text{eff}}(\mathbf{k}, z_1, z_2) = & \ll \mathbf{j}(\mathbf{k}) \gg + 2 \left[\Sigma(\mathbf{k}, z_2) \mathbf{f}(z_2) \mathbf{j}^{(1)}(\mathbf{k}) + \mathbf{j}^{(1)}(\mathbf{k}) \mathbf{f}(z_1) \Sigma(\mathbf{k}, z_1) \right] \\ & + \Sigma(\mathbf{k}, z_2) \mathbf{f}(z_2) \mathbf{j}^{(2)}(\mathbf{k}) \mathbf{f}(z_1) \Sigma(\mathbf{k}, z_1) \end{aligned} \quad (4.2)$$

where

$$\mathbf{f}(z) = f_{LL'}(z) = \left\langle \frac{1}{\Delta_L} \right\rangle \left[\frac{C_L^A}{\Delta_L^A} - \frac{C_L^B}{\Delta_L^B} - z \left(\frac{1}{\Delta_L^A} - \frac{1}{\Delta_L^B} \right) \right]^{-1} \delta_{LL'}$$

and

$$\Sigma = \mathbf{g}^{-1} - \mathbf{G}^{-1}$$

\mathbf{g} is the virtual crystal Green function. The interested readers are referred to the chapter 6 which derives these expressions in some detail. The main point in setting these equations out, is to note that in such calculations one needs the *full* Green matrix in angular momentum space. This is the main motivation for this work.

The first step in setting up the block recursion procedure is to systematically renumber the real-space basis with integers. An example on a square lattice is shown in figure 4.1.

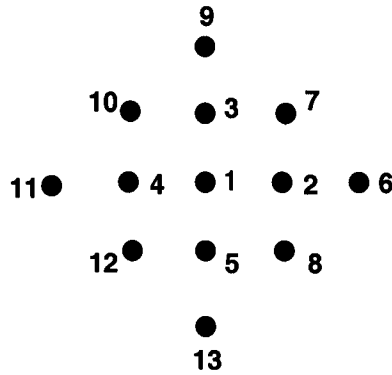


Figure 4.1: Systematic discrete numbering of the nearest-neighbour map on a square lattice.

The nearest-neighbour map is now generated by a systematic numbering of the states in augmented space as follows :

(A) Real-space formulation : We start with numbering $|R, \{\emptyset\}\rangle$ as 1, and then recursively generate the neighbours by acting on the states by $\tilde{\mathbf{S}}$ and $\tilde{\mathbf{F}}$. Let us take an example of a square lattice :

1. $\tilde{\mathbf{S}}$ acting on $|1, \{\emptyset\}\rangle \equiv |1\rangle$ gives four new neighbours $|2, \{\emptyset\}\rangle \dots |5, \{\emptyset\}\rangle$. The four real-space neighbours of $|1\rangle$ are then $|2\rangle, |3\rangle, |4\rangle$ and $|5\rangle$.
2. $\tilde{\mathbf{F}}$ acting on $|1, \{\emptyset\}\rangle \equiv |1\rangle$ gives $|1, \{1\}\rangle$. This we number $|6\rangle$.
3. $\tilde{\mathbf{S}}$ acting on $|2, \{\emptyset\}\rangle \equiv |2\rangle$ gives : $|6, \{\emptyset\}\rangle, |7, \{\emptyset\}\rangle, |1, \{\emptyset\}\rangle$ and $|8, \{\emptyset\}\rangle$. These we number $|7\rangle, |8\rangle, |1\rangle$ and $|9\rangle$.
4. $\tilde{\mathbf{F}}$ acting on $|2, \{\emptyset\}\rangle \equiv |2\rangle$ gives $|2, \{2\}\rangle \equiv |10\rangle$.

We proceed exactly as above and finally obtain the nearest-neighbour map matrix, the n th column of whose m th row gives the n th neighbour of m . We show below the initial part of the nearest-neighbour map for the above example :

$$\begin{pmatrix} 2 & 3 & 4 & 5 & 6 \\ 7 & 8 & 1 & 9 & 10 \\ 8 & 11 & 12 & 1 & 13 \\ \dots & \dots & \dots & \dots & \dots \end{pmatrix}$$

The equivalences are :

Augmented-space element	⇒	1{∅}	2{∅}	3{∅}	4{∅}	5{∅}	1{1}	6{∅}
Discrete numbering	⇒	1	2	3	4	5	6	7

Augmented-space element	⇒	7{∅}	8{∅}	2{2}	9{∅}	10{∅}	3{3}
Discrete numbering	⇒	8	9	10	11	12	13

(B) Reciprocal-space formulation : In reciprocal-space the procedure is even simpler, since the operators act *only* on the configuration part of the space. As before, we start with numbering $|k, \{\emptyset\}\rangle$ as 1 and then recursively generate the neighbours by acting on the states successively by $\tilde{\mathbf{S}}$ and $\tilde{\mathbf{F}}$. Let us take the example of the square lattice :

1. $\tilde{\mathbf{S}}$ acting on $|\{\emptyset\}\rangle \equiv |1\rangle$ leaves it unchanged. The four neighbours of $|1\rangle$ are then $|1\rangle, |1\rangle, |1\rangle$ and $|1\rangle$.
2. $\tilde{\mathbf{F}}$ acting on $|\{\emptyset\}\rangle \equiv |1\rangle$ is $|\{1\}\rangle$. This we number $|2\rangle$.
3. $\tilde{\mathbf{S}}$ acting on $|\{1\}\rangle \equiv |2\rangle$ gives : $|\{2\}\rangle, |\{3\}\rangle, |\{4\}\rangle$ and $|\{5\}\rangle$. These we number $|3\rangle, |4\rangle, |5\rangle$ and $|6\rangle$.
4. $\tilde{\mathbf{F}}$ acting on $|\{1\}\rangle \equiv |2\rangle$ is $|\{\emptyset\}\rangle \equiv |1\rangle$.

We proceed as before and obtain the nearest-neighbour map matrix. We again show below the initial part of the nearest-neighbour map in reciprocal-space :

$$\begin{pmatrix} 1 & 1 & 1 & 1 & 2 \\ 3 & 4 & 5 & 6 & 1 \\ 7 & 8 & 2 & 9 & 10 \\ \dots\dots\dots \end{pmatrix}$$

Now the equivalences are :

Cardinality sequence	⇒	{∅}	{1}	{2}	{3}	{4}	{5}	{6}	{7}	{8}	{1, 2}
Discrete numbering	⇒	1	2	3	4	5	6	7	8	9	10

(C) **The Block recursion** : We now go over to a matrix basis of the form $\{\Phi_{J,LL'}^{(n)}\}$, where J is the discrete labelling of the augmented space states and L, L' labels the angular momenta. The inner product of such basis is defined by

$$\left(\Phi^{(n)}, \Phi^{(m)}\right) = \sum_J \sum_{L''} \Phi_{LL'',J}^{(n)\dagger} \Phi_{J,L''L'}^{(m)} = N_{LL'}^{nm}$$

For a real-space calculations on a lattice with Z nearest-neighbours, we start the recursion with

$$\Phi_{J,LL'}^{(1)} = \mathbf{W}_{LL'}^{(1)} \delta_{J,1} + \mathbf{W}_{LL'}^{(2)} \delta_{J,Z+1},$$

while for a reciprocal-space calculation we start with

$$\Phi_{J,LL'}^{(1)} = \mathbf{W}_{LL'}^{(1)} \delta_{J,1} + \mathbf{W}_{LL'}^{(2)} \delta_{J,2},$$

where

$$\mathbf{W}_{LL'}^{(1)} = \frac{A(\Delta_L^{-1/2})}{[A(\Delta_L^{-1})]^{1/2}} \delta_{LL'} \quad \mathbf{W}_{LL'}^{(2)} = \frac{F(\Delta_L^{-1/2})}{[A(\Delta_L^{-1})]^{1/2}} \delta_{LL'}. \quad (4.3)$$

The remaining terms in the basis are recursively obtained from

$$\begin{aligned} \sum_{L''} \Phi_{J,LL''}^{(2)} B_{L''L'}^{(2)\dagger} &= \sum_{J'} \sum_{L''} H_{JL,J'L''} \Phi_{J',L''L'}^{(1)} - \sum_{L''} \Phi_{J,LL''}^{(1)} A_{L''L'}^{(1)} \\ \sum_{L''} \Phi_{J,LL''}^{(n+1)} B_{L''L'}^{(n+1)\dagger} &= \sum_{J'} \sum_{L''} H_{JL,J'L''} \Phi_{J',L''L'}^{(n)} - \sum_{L''} \Phi_{J,LL''}^{(n)} A_{L''L'}^{(n)} - \sum_{L''} \Phi_{J,LL''}^{(n-1)} B_{L''L'}^{(n)}. \end{aligned}$$

Orthogonalization of the basis gives

$$\sum_J \sum_{L''} \sum_{J'} \sum_{L'''} \Phi_{LL'',J}^{(n)\dagger} H_{JL,J'L'''} \Phi_{J',L''L'}^{(n)} = \sum_{L''} N_{LL''}^{nn} A_{L''L'}^{(n)}. \quad (4.4)$$

In matrix notation, where matrices are in angular momentum space,

$$\mathbf{A}^{(n)} = (\mathbf{N}^{nn})^{-1} \sum_J \sum_{J'} \Phi_J^{(n)\dagger} \mathbf{H}_{JJ'} \Phi_{J'}^{(n)}. \quad (4.5)$$

Next, we note that we had started with $J_{\max} \times L_{\max}^2$ orthogonal basis set. The above procedure merely gives J_{\max} basis sets. We still have orthogonality conditions among the various columns of $\Phi_{J,LL'}^{(n)}$. In order to impose these conditions, consider

$$\Psi_{J,LL'} = \sum_{J'} \sum_{L''} H_{JL,J'L''} \Phi_{J',L''L'}^{(n)} - \sum_{L''} \Phi_{J,LL''}^{(n)} A_{L''L'}^{(n)} - \sum_{L''} \Phi_{J,LL''}^{(n-1)} B_{L''L'}^{(n)}.$$

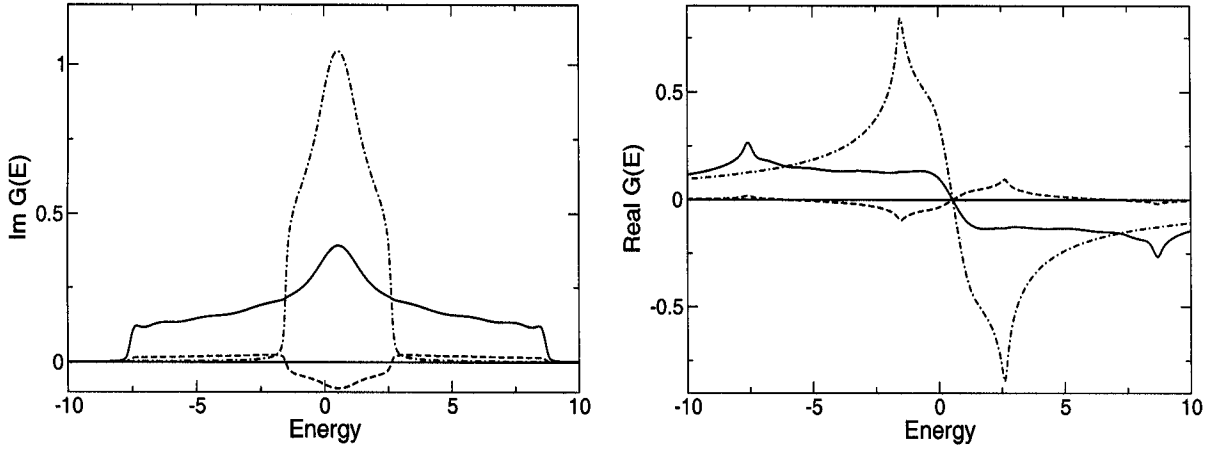


Figure 4.2: The real and imaginary parts of the Green matrix for a 2×2 Hamiltonian model. The full lines refer to \mathbf{G}_{11} , the dashed-dotted line to \mathbf{G}_{22} and dashed lines to \mathbf{G}_{12} .

get a smooth density of states we had taken $\delta = 0.01$ and $N_{\max} = 10^4$. The elements of the Green matrix are shown in figure 4.2. The imaginary part of the diagonal elements give the projected density of states. Herglotz properties of the diagonal parts give rise to a positive definite density of states. The off-diagonal part is relatively small and is not Herglotz. The projected density of states is symmetric, as is the imaginary part of the off-diagonal element. The real parts of the matrix elements are also shown. These are related to the imaginary parts by the Kramers-Krönig relation.

(B) The s-d model of a transition-noble metal alloy : Levin and Ehrenreich 1971, and Gelatt and Ehrenreich 1974 have introduced a simple two band model for transition-noble metal alloys. Physical effects like charge transfer between constituents will usually differ for the s-p conduction bands on one hand and the relatively narrow d bands on the other. Their model includes the conduction bands described together as a single band and the set of d bands also described as a single band and their hybridization. The model also takes into account the large widths of the conduction bands and the relatively narrow widths of the d bands. The following Hamiltonian has many (but not all) of the essential features :

$$H = \sum_R \begin{pmatrix} \epsilon_s & \gamma \\ \gamma & \epsilon_d \end{pmatrix} P_R + \sum_R \sum_{R'} \begin{pmatrix} t_s & 0 \\ 0 & t_d \end{pmatrix} T_{RR'} \quad (4.9)$$

The dominant disorder is taken to be in the terms ϵ_s and ϵ_d . The hybridization is taken

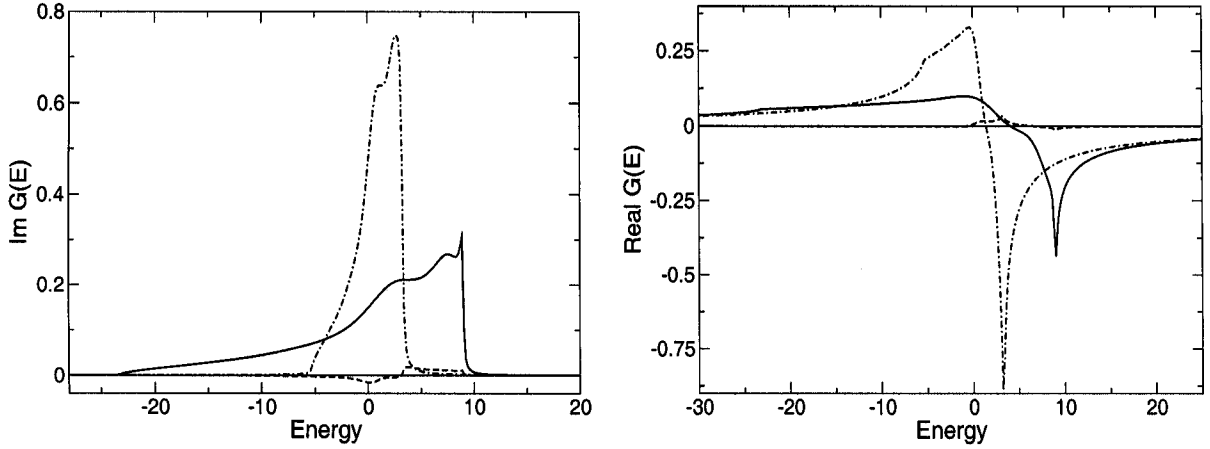


Figure 4.3: The real and imaginary parts of the Green matrix for the s-d model on a fcc lattice. The calculations were done by a real-space block recursion. The full lines refer to \mathbf{G}_{11} , the dashed-dotted line to \mathbf{G}_{22} and dashed lines to \mathbf{G}_{12} .

between states at the same site only and the hopping terms are related by $t_s = \alpha t_d$. The sites R vary over the sites of a face-centered cubic lattice. As a model case we have taken the parameters shown in the following table :

Table 4.1: Parameters for our calculation for $A_{50}B_{50}$ alloy on a fcc lattice.

Constituent	ϵ_s	ϵ_d	γ	α	t_d
A	1.5	1.5	0.2	4.0	-0.5
B	0.0	0.0	0.2	4.0	-0.5

(i) **Calculations using real-space block recursion** : Figure 4.3 shows the real and imaginary parts of the Green matrix. These calculation are carried out through a real-space block recursion technique. In general the qualitative features for the diagonal elements are similar to our square lattice model. The main difference is that on a fcc lattice the partial density of states, related to the imaginary part of the diagonal elements of the Green matrix, are no longer symmetric about the band centre. Consequently, the behaviour of the off-diagonal element is quite different. The total density of states is given by

$$n(E) = (1/\pi) \text{Im} \left(G_{ss}(E - i\delta) + 5G_{dd}(E - i\delta) \right).$$

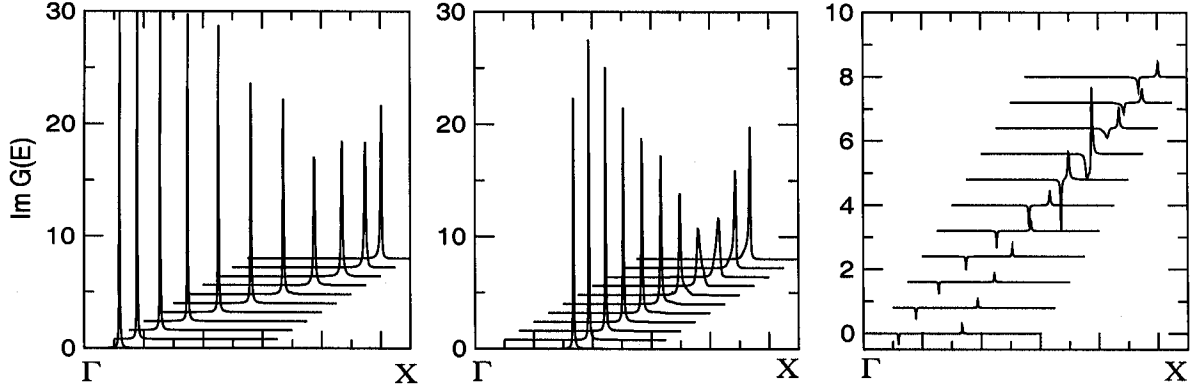


Figure 4.4: The matrix elements of $\mathbf{G}(\mathbf{k}, E)$ on a fcc lattice : the 11 element (left), the 22 element (middle), and the 12 element (right) along the Γ to X direction.

If, for example, the number of electrons in the constituents is 5 per atom per spin for A and 5.5 per atom per spin for B, the position of the Fermi energy is given by

$$\int_{-\infty}^{E_F} dE n(E) = \langle n_e \rangle = x n_A + (1 - x) n_B = 5.25$$

where n_A and n_B are the number of valence electrons of A and B type of atom.

(ii) Calculations using reciprocal-space block recursion : We have carried out the block recursion in reciprocal-space for the s-d model. The Green matrix in reciprocal-space $\mathbf{G}(\mathbf{k}, E)$ is the factor that arises in our earlier expression for the configuration-averaged current-current correlation function. Its diagonal matrix element is related to the spectral functions for the different bands. In figure 4.4 we show the spectral functions along a given direction $\Gamma - X$ in reciprocal-space. The imaginary part of the off-diagonal matrix element is also shown in the figure. We note that the off-diagonal part of the Green matrix has antisymmetric structure in its peaks, while the diagonal matrix elements are positive (as they represent spectral functions).

Figure 4.5 shows the Green matrix elements calculated starting from the $\mathbf{G}(\mathbf{k}, E)$ and carrying out a reciprocal-space integration developed by us (Saha *et al* 2004) as a generalization of the tetrahedron method proposed by Jepsen and Andersen 1971 for crystalline systems. The close comparison between the figures 4.3 and 4.5 gives strong support for the accuracy of the reciprocal-space recursion followed by the generalized tetrahedron integration developed in the previous chapter.

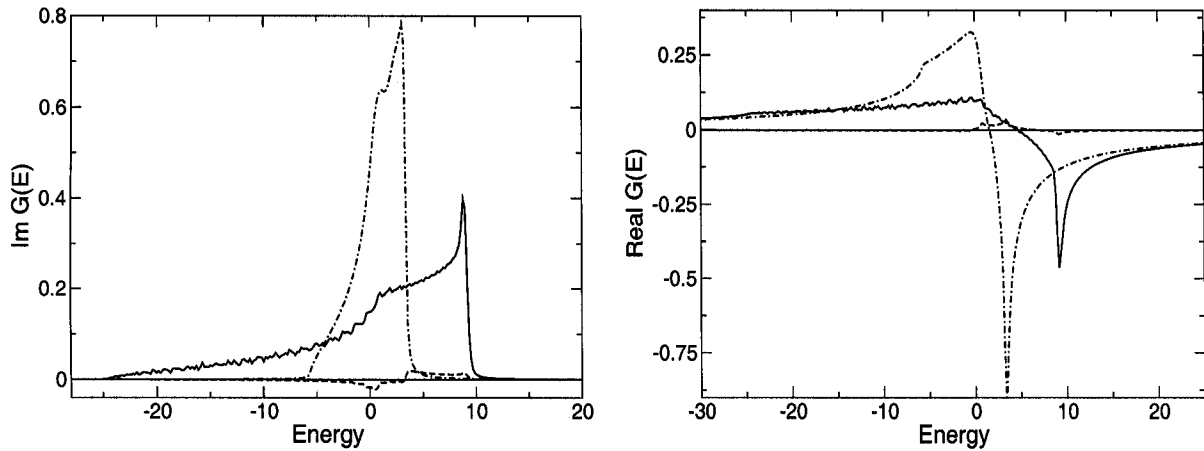


Figure 4.5: The real and imaginary parts of the Green matrix for the s-d model on a fcc lattice. The calculations are done by a k-space block recursion followed by a reciprocal-space integration (Saha *et al* 2004). The full lines refer to \mathbf{G}_{11} , the dashed-dotted line to \mathbf{G}_{22} and dashed lines to \mathbf{G}_{12} .

4.3 Conclusion

In this chapter we have described a block recursion in augmented space suitable for calculations of the Green matrices. The recursion is set up both with real-space augmented by the configuration space of the alloy and the reciprocal-space augmented with the configuration space. For the latter case we have coupled it with a Brillouin zone integration scheme which is a generalization of the tetrahedron method developed earlier for crystalline systems. The Green matrices are essential for the calculation of the response functions and effective current terms which are related to the self-energy matrices. We propose to use these techniques in our next applications.

Chapter 5

Optical properties of ordered compounds

5.1 Introduction

The object of our present study is to derive an expression for the optical conductivity as a convolution of the energy-resolved joint density of states (JDOS) and an energy-frequency dependent transition rate. The need is to go beyond the usual reciprocal-space based formulations and obtain an expression which we can immediately generalize for disordered systems. This would require labelling states by energy and the angular momentum labels (ℓ, m) alone. Once we derive this expression we shall find a representation for the optical conductivity in the minimal basis set of the TB-LMTO. The generalization to disordered systems will be carried out through the ASR introduced earlier for the study of electronic properties of disordered systems (Mookerjee 1973, Ghosh *et al* 1999). The ASR carries out the configuration averaging essential to the description of properties of disordered systems, going beyond the usual mean-field approaches and taking into account configuration fluctuations. The input into the ASR method includes the Hamiltonian parameters of the pure constituents, as the starting point of the local spin-density approximation (LSDA) iterations for the alloy. It also includes the information about the transition rates of the pure constituents, expressed as functions of the initial and final state energies. The aim of this work is to reformulate the reciprocal-space representation of the transition rate and re-express it in the energy-frequency labelled representation for the pure constituents.

⁰The contents of this chapter has been published in two papers : (1) **K K Saha**, T Saha-Dasgupta, A Mookerjee, S Saha and T P Sinha, *J. Phys.: Condens. Matter* **14** 3849 (2002) and (2) B Ganguli, **K K Saha**, A Mookerjee, *Physica B* **348** 382 (2004).

Only when we are confident that this works can we proceed with the full calculations for the disordered alloy. This work is an attempt to verify our formulation for a series of alkaline-earth titanates in the paraelectric phase and the defect-chalcopyrite ZnIn_2Te_4 , on which extensive theoretical and experimental data of optical properties are available for comparison.

5.2 Methodology

In recent years a number of methods have been proposed for calculating optical properties within the framework of the LMTO (Uspenski *et al* 1983, Alouani *et al* 1986, Alouani *et al* 1988, Zemach *et al* 1989a, Zemach *et al* 1989b, Hobbs *et al* 1995) for both metals and semiconductors. We shall present here a gauge-independent formalism, following the ideas of Hobbs *et al* 1995. Since our final aim is to use the ASR method (Mookerjee 1973, Kaplan and Gray 1977, Saha *et al* 1996, Dasgupta *et al* 1997, Ghosh *et al* 1999) to study the optical properties of random systems, we shall modify the reciprocal-space formulation and obtain an expression in which all states are labelled by their energy and the optical conductivity is expressed as a convolution of the energy-resolved JDOS and an energy-frequency dependent transition matrix. This formulation will then be directly generalized within the ASR.

The Hamiltonian describing the effect of a radiation field on the electronic states of a solid is given by

$$H = \sum_{i=1}^N \left\{ \frac{1}{2m_e} \left(\mathbf{p}_i + \frac{e}{c} \mathbf{A}(\mathbf{r}_i, t) \right)^2 + V(\mathbf{r}_i) + e\Phi(\mathbf{r}_i, t) \right\}.$$

Here e is the magnitude of electronic charge, m_e the electronic mass, c is the velocity of light and \hbar is the Planck's constant. $\mathbf{A}(\mathbf{r}_i, t)$ and $\Phi(\mathbf{r}_i, t)$ are the vector and scalar potentials seen by the i th electron because of the radiation field. There are N electrons labelled by i . The potential $V(\mathbf{r}_i)$ experienced by the electrons is expressed as an effective independent electron approximation within the LDA of the density functional theory (DFT). For not-too-large external optical fields, neglecting terms of the order of $|\mathbf{A}|^2$, the Hamiltonian reduces to

$$H = \sum_{i=1}^N \left\{ \frac{1}{2m_e} \mathbf{p}_i^2 + V(\mathbf{r}_i) + \frac{1}{c} \mathbf{A}(\mathbf{r}_i, t) \cdot \mathbf{j}_i \right\}. \quad (5.1)$$

Here $\mathbf{j}_i = (e/m) \mathbf{p}_i$ is the current operator. We work in the Coulomb gauge where $\nabla \cdot \mathbf{A}(\mathbf{r}_i, t) = 0$ and $\Phi(\mathbf{r}_i, t) = 0$, so that the electric field

$$\mathbf{E}(\mathbf{r}_i, t) = -\frac{\partial \mathbf{A}(\mathbf{r}_i, t)}{\partial t}.$$

In choosing the above equation we have ignored the response of the system. The local electric field is made up of the external field due to the incident radiation as well as the internal field due to the polarization of the medium. Such local field corrections are important for insulators. We intend, as is customary, to introduce the local field corrections as well as corrections due to the Coulomb hole in our final GW calculations, for which the single-particle picture will form the zeroth starting point.

The Kubo formula then relates the linear current response to the radiation field :

$$\langle j_\mu(t) \rangle = \sum_\nu \int_{-\infty}^{\infty} dt' \chi_{\mu\nu}(t-t') A_\nu(t').$$

The generalized susceptibility is given by

$$\chi_{\mu\nu}(\tau) = i\Theta(\tau) \langle \phi_0 | [j_\mu(\tau), j_\nu(0)] | \phi_0 \rangle$$

where $\tau = t - t'$ and $\Theta(\tau)$ is the Heaviside step function:

$$\Theta(\tau) = \begin{cases} 1 & \text{if } \tau > 0 \\ 0 & \text{if } \tau \leq 0. \end{cases}$$

$|\phi_0\rangle$ is the ground state of the unperturbed system, that is, the solid in the absence of the radiation field. In the absence of the radiation field, there is no photocurrent, i.e. $\langle \phi_0 | j_\mu | \phi_0 \rangle = 0$. The fluctuation-dissipation theorem relates the imaginary part of the generalized susceptibility to the correlation function as follows :

$$\chi''_{\mu\nu}(\omega) = \frac{1}{2} (1 - e^{-\beta\hbar\omega}) S_{\mu\nu}(\omega) \quad (5.2)$$

where

$$\beta = \frac{1}{k_B T}$$

where k_B is the Boltzmann constant and T the temperature and

$$\chi''_{\mu\nu}(\omega) = \text{Im} \int_{-\infty}^{\infty} dt e^{iz\tau} \chi_{\mu\nu}(\tau) \quad z=\omega+i0^+$$

and

$$S_{\mu\nu}(\omega) = \text{Im} \int_{-\infty}^{\infty} dt e^{iz\tau} \langle \phi_0 | j_\mu(\tau) j_\nu(0) | \phi_0 \rangle \quad z=\omega+i0^+. \quad (5.3)$$

An expression for the correlation function can be obtained via the Kubo-Greenwood expression:

$$S(\omega) = \frac{\pi}{3} \sum_i \sum_f \sum_\mu \langle \phi_i | j_\mu | \phi_f \rangle \langle \phi_f | j_\mu | \phi_i \rangle \delta(E_f - E_i - \hbar\omega). \quad (5.4)$$

We have assumed isotropy of the response so that the tensor $S_{\mu\nu}$ is diagonal and we have defined $S(\omega)$ as the direction averaged quantity $\frac{1}{3} \sum_\mu S_{\mu\mu}(\omega)$. The $|\{\phi_i\}\rangle$ are the occupied 'initial' single-electronic states in the ground state while $|\{\phi_f\}\rangle$ are the unoccupied single-electron 'final' excited states in the LDA description.

The imaginary part of the dielectric function is related to the above :

$$\epsilon_2(\omega) = \frac{1}{\pi^2 \omega^2} S(\omega). \quad (5.5)$$

We may obtain the real part of the dielectric function $\epsilon_1(\omega)$ from a Kramers-Krönig relationship,

$$\epsilon_1(\omega) = 1 + \frac{2}{\pi} \int_0^\infty \frac{(\omega' - \omega) \epsilon_2(\omega')}{\omega'^2 - \omega^2} d\omega'. \quad (5.6)$$

For crystalline semiconductors the equation (5.4) may be rewritten as follows :

$$S(\omega) = \frac{\pi}{3} \sum_j \sum_{j'} \int_{\text{BZ}} \frac{d^3\mathbf{k}}{8\pi^3} |\langle \Phi_{j'\mathbf{k}} | \mathbf{j} | \Phi_{j\mathbf{k}} \rangle|^2 \delta(E_{j'}(\mathbf{k}) - E_j(\mathbf{k}) - \hbar\omega). \quad (5.7)$$

Here j and j' refer to band labels : j for the occupied valence bands and j' the unoccupied conduction bands at $T=0$ K. The \mathbf{k} is the quantum label associated with the Bloch theorem. For disordered materials, the Bloch theorem fails and the expression (5.7) can no longer be used. Our first aim will be to obtain an alternative expression where the

quantum states are directly labelled by energy and frequency, rather than by the ‘band’ and ‘crystal momentum’ indices. To this end, let us examine the following expressions :

$$n(E) = \sum_j \int_{\text{BZ}} \frac{d^3\mathbf{k}}{8\pi^3} \delta(E_j(\mathbf{k}) - E) \quad (5.8)$$

$$J(E, \omega) = \sum_j^{\text{occ}} \sum_{j'}^{\text{unocc}} \int_{\text{BZ}} \frac{d^3\mathbf{k}}{8\pi^3} \delta(E_j(\mathbf{k}) - E) \delta(E_{j'}(\mathbf{k}) - E - \hbar\omega). \quad (5.9)$$

In the equation (5.8), the right hand side picks up a factor of 1 whenever a quantum state, labelled by $\{\mathbf{k}, j\}$ falls in the range $E, E+\delta E$. The left-hand side, therefore, is the *density of states* arising from the bands labelled j .

In the equation (5.9), the right-hand side picks up a factor of 1 whenever a quantum state in the filled bands labelled j falls in the range $E, E+\delta E$ and *simultaneously* a quantum state in the unfilled bands labelled j' falls in the range $E+\omega, E+\omega+\delta E$. The left-hand side is then the *energy-resolved joint density of states* :

$$J(E, \omega) = n_v(E) n_c(E + \hbar\omega). \quad (5.10)$$

We shall define the energy-frequency labelled *transition rate* as

$$T(E, \omega) = \frac{\sum_j \sum_{j'} \int_{\text{BZ}} \frac{d^3\mathbf{k}}{8\pi^3} T^{jj'}(\mathbf{k}) \delta(E_j(\mathbf{k}) - E) \delta(E_{j'}(\mathbf{k}) - E - \hbar\omega)}{\sum_j \sum_{j'} \int_{\text{BZ}} \frac{d^3\mathbf{k}}{8\pi^3} \delta(E_j(\mathbf{k}) - E) \delta(E_{j'}(\mathbf{k}) - E - \hbar\omega)} \quad (5.11)$$

where

$$T^{jj'}(\mathbf{k}) = \sum_{\mu} \left| \langle \Phi_{j'\mathbf{k}} | j_{\mu} | \Phi_{j\mathbf{k}} \rangle \right|^2.$$

The expression for $S(\omega)$ from equation (5.7) then becomes

$$S(\omega) = (\pi/3) \int dE T(E, \omega) J(E, \omega). \quad (5.12)$$

Many earlier workers argued that the transition matrix element is weakly dependent on both E and ω . They then assumed it to be constant, T_0 , and obtained a simple expression for the correlation function :

$$S_0(\omega) = (\pi/3) T_0 \int dE J(E, \omega). \quad (5.13)$$

We shall investigate the validity of this approximation for the systems under study in this work. Let us first get an expression for the equation (5.12) within the TB-LMTO formalism of Andersen 1975 and Skriver 1984: The basis of the LMTO starts from the minimal muffin-tin orbital basis set of a KKR formalism and then linearizes it by expanding around a ‘nodal’ energy point $E_{\nu\ell}^\alpha$. The wave function is then expanded in this basis :

$$\Phi_{j\mathbf{k}}(\mathbf{r}) = \sum_L \sum_\alpha c_{L\alpha}^{j\mathbf{k}} \left[\phi_{\nu L}^\alpha(\mathbf{r}) + \sum_{L'} \sum_{\alpha'} h_{LL'}^{\alpha\alpha'}(\mathbf{k}) \phi_{\nu L'}^{\alpha'}(\mathbf{r}) \right]$$

where L is the composite angular momentum index (ℓ, m) , j is the band index and α labels the atom in the unit cell. Also,

$$\begin{aligned} \phi_{\nu L}^\alpha(\mathbf{r}) &= i^\ell Y_L(\hat{r}) \phi_\ell^\alpha(r, E_{\nu\ell}^\alpha), \\ \dot{\phi}_{\nu L}^\alpha(\mathbf{r}) &= i^\ell Y_L(\hat{r}) \frac{\partial \phi_\ell^\alpha(r, E_{\nu\ell}^\alpha)}{\partial E}, \\ h_{LL'}^{\alpha\alpha'}(\mathbf{k}) &= (C_L^\alpha - E_{\nu\ell}^\alpha) \delta_{LL'} \delta_{\alpha\alpha'} + \sqrt{\Delta_L^\alpha} S_{LL'}^{\alpha\alpha'}(\mathbf{k}) \sqrt{\Delta_{L'}^{\alpha'}}. \end{aligned}$$

C_L^α and Δ_L^α are TB-LMTO potential parameters and $S_{LL'}^{\alpha\alpha'}(\mathbf{k})$ is the structure matrix. These terms are standard for the LMTO formulation and the reader is referred to the citation (Andersen 1975) for greater detail. The TB-LMTO secular equation provides the expansion coefficients $c_{L\alpha}^{j\mathbf{k}}$ via

$$\sum_{L'} \sum_{\alpha'} \left[h_{LL'}^{\alpha\alpha'}(\mathbf{k}) + (E_{\nu\ell}^\alpha - E^{j\mathbf{k}}) \delta_{LL'} \delta_{\alpha\alpha'} \right] c_{L'\alpha'}^{j\mathbf{k}} = 0. \quad (5.14)$$

We may now immediately write an expression for the matrix element of the current operator as in equation (5.11) :

$$\begin{aligned} \langle \Phi_{j'\mathbf{k}}(\mathbf{r}) | \mathbf{j} | \Phi_{j\mathbf{k}}(\mathbf{r}) \rangle &= \sum_{LL'} \sum_\alpha \bar{c}_{L'\alpha}^{j'\mathbf{k}} c_{L\alpha}^{j\mathbf{k}} \left\{ \langle \phi_{\nu L'}^\alpha(\mathbf{r}) | \mathbf{j} | \phi_{\nu L}^\alpha(\mathbf{r}) \rangle \right. \\ &+ (E^{j\mathbf{k}} - E_{\nu\ell}^\alpha) \langle \phi_{\nu L'}^\alpha(\mathbf{r}) | \mathbf{j} | \dot{\phi}_{\nu L}^\alpha(\mathbf{r}) \rangle \\ &+ (E^{j'\mathbf{k}} - E_{\nu\ell'}^\alpha) \langle \dot{\phi}_{\nu L'}^\alpha(\mathbf{r}) | \mathbf{j} | \phi_{\nu L}^\alpha(\mathbf{r}) \rangle \\ &\left. + (E^{j\mathbf{k}} - E_{\nu\ell}^\alpha) (E^{j'\mathbf{k}} - E_{\nu\ell'}^\alpha) \langle \dot{\phi}_{\nu L'}^\alpha(\mathbf{r}) | \mathbf{j} | \dot{\phi}_{\nu L}^\alpha(\mathbf{r}) \rangle \right\} \quad (5.15) \end{aligned}$$

We shall now obtain expressions for the right-hand terms by noting the following :

$$\mathbf{j} = e \frac{d\mathbf{r}}{dt} = \frac{e}{i\hbar} [\mathbf{r}, H]$$

$$H\phi_{\nu L}^{\alpha}(\mathbf{r}) = E_{\nu\ell}^{\alpha} \phi_{\nu L}^{\alpha}(\mathbf{r}), H\dot{\phi}_{\nu L}^{\alpha}(\mathbf{r}) = \phi_{\nu L}^{\alpha}(\mathbf{r}) + E_{\nu\ell}^{\alpha} \dot{\phi}_{\nu L}^{\alpha}(\mathbf{r}). \quad (5.16)$$

We can write

$$\mathbf{r} = (2\pi/3)^{1/2} r \left[(Y_{1,-1} - Y_{1,1}) \hat{\mathbf{i}} + i(Y_{1,-1} + Y_{1,1}) \hat{\mathbf{j}} + 2^{1/2} Y_{1,0} \hat{\mathbf{k}} \right].$$

Using the above two equations we get

$$\int \phi_{\nu L'}^{\alpha}(\mathbf{r})^* \mathbf{r} H \phi_{\nu L}^{\alpha}(\mathbf{r}) d^3\mathbf{r} = i^{\ell-\ell'} E_{\nu\ell}^{\alpha} \Gamma_{LL'} \int_0^{s_{\alpha}} \phi_{\nu\ell'}^{\alpha}(r) \phi_{\nu\ell}^{\alpha}(r) r^3 dr \quad (5.17)$$

where s_{α} is the atomic sphere radius of the α th atom in the unit cell and $\Gamma_{LL'}$ is a combination of Gaunt coefficients Hobbs *et al* 1995 :

$$\Gamma_{LL'} = \sqrt{(2\pi/3)} \left[(G_{\ell',1,\ell}^{m',-1,m} - G_{\ell',1,\ell}^{m',1,m}) \hat{\mathbf{i}} + i(G_{\ell',1,\ell}^{m',-1,m} + G_{\ell',1,\ell}^{m',1,m}) \hat{\mathbf{j}} + \sqrt{2} G_{\ell',1,\ell}^{m',0,m} \hat{\mathbf{k}} \right]$$

In order to obtain $\int \phi_{\nu L'}^{\alpha}(\mathbf{r})^* H \mathbf{r} \phi_{\nu L}^{\alpha}(\mathbf{r}) d^3\mathbf{r}$, we note that $H = (\hbar^2/2m_e)\nabla^2 + V(\mathbf{r})$ so using the Green's second identity we can obtain

$$\begin{aligned} \int \phi_{\nu L'}^{\alpha}(\mathbf{r})^* H \mathbf{r} \phi_{\nu L}^{\alpha}(\mathbf{r}) d^3\mathbf{r} &= i^{\ell-\ell'} \Gamma_{LL'} \left\{ E_{\nu\ell'}^{\alpha} \int_0^{s_{\alpha}} \phi_{\nu\ell'}^{\alpha}(r) \phi_{\nu\ell}^{\alpha}(r) r^3 dr \right. \\ &\quad \left. + (\hbar^2/2m_e) s_{\alpha}^2 \phi_{\nu\ell}^{\alpha}(s_{\alpha}) \phi_{\nu\ell'}^{\alpha}(s_{\alpha}) (D_{\nu\ell'}^{\alpha} - D_{\nu\ell}^{\alpha} - 1) \right\}. \end{aligned} \quad (5.18)$$

$D_{\nu\ell}^{\alpha}$ are the logarithmic derivatives of $\phi_{\nu\ell}^{\alpha}(r)$ at $r = s_{\alpha}$ and are obtained as parameters in the TB-LMTO routines. We define the following integrals :

$$\begin{aligned} \int_0^{s_{\alpha}} \phi_{\nu\ell'}^{\alpha}(r) \phi_{\nu\ell}^{\alpha}(r) r^3 dr &= I_{\ell\ell'}^{\alpha} \\ \int_0^{s_{\alpha}} \phi_{\nu\ell'}^{\alpha}(r) \dot{\phi}_{\nu\ell}^{\alpha}(r) r^3 dr &= J_{\ell\ell'}^{\alpha} \\ \int_0^{s_{\alpha}} \dot{\phi}_{\nu\ell'}^{\alpha}(r) \dot{\phi}_{\nu\ell}^{\alpha}(r) r^3 dr &= K_{\ell\ell'}^{\alpha} \end{aligned}$$

and use the notation $(\hbar^2/2m_e) s_{\alpha}^2 (D_{\nu\ell}^{\alpha} - D_{\nu\ell'}^{\alpha} - 1) = \mathcal{D}_{\ell\ell'}^{\alpha}$. Then the matrix elements for the current operator become

$$\begin{aligned} \mathcal{I}_{LL',\mu}^{(1)\alpha} &= \langle \phi_{\nu L'}^{\alpha}(\mathbf{r}) | j_{\mu} | \phi_{\nu L}^{\alpha}(\mathbf{r}) \rangle = \frac{i^{\ell-\ell'-1}}{\hbar} \Gamma_{LL'}^{\mu} [(E_{\nu\ell}^{\alpha} - E_{\nu\ell'}^{\alpha}) I_{\ell'\ell}^{\alpha} - \mathcal{D}_{\ell'\ell}^{\alpha} \phi_{\nu\ell}^{\alpha}(s_{\alpha}) \phi_{\nu\ell'}^{\alpha}(s_{\alpha})] \\ \mathcal{I}_{LL',\mu}^{(2)\alpha} &= \langle \phi_{\nu L'}^{\alpha}(\mathbf{r}) | j_{\mu} | \dot{\phi}_{\nu L}^{\alpha}(\mathbf{r}) \rangle = \frac{i^{\ell-\ell'-1}}{\hbar} \Gamma_{LL'}^{\mu} [(E_{\nu\ell}^{\alpha} - E_{\nu\ell'}^{\alpha}) J_{\ell'\ell}^{\alpha} + I_{\ell'\ell}^{\alpha} - \mathcal{D}_{\ell'\ell}^{\alpha} \dot{\phi}_{\nu\ell}^{\alpha}(s_{\alpha}) \phi_{\nu\ell'}^{\alpha}(s_{\alpha})] \end{aligned}$$

$$\begin{aligned} \mathcal{I}_{LL',\mu}^{(3)\alpha} &= \langle \dot{\phi}_{\nu L'}^\alpha(\mathbf{r}) | j_\mu | \phi_{\nu L}^\alpha(\mathbf{r}) \rangle = \frac{v^{\ell-\ell'-1}}{\hbar} \Gamma_{LL'}^\mu \left[(E_{\nu\ell}^\alpha - E_{\nu\ell'}^\alpha) J_{\ell\ell'}^\alpha - I_{\ell\ell'}^\alpha - \mathcal{D}_{\ell\ell'}^\alpha \phi_{\nu\ell}^\alpha(s_\alpha) \dot{\phi}_{\nu\ell'}^\alpha(s_\alpha) \right] \\ \mathcal{I}_{LL',\mu}^{(4)\alpha} &= \langle \dot{\phi}_{\nu L'}^\alpha(\mathbf{r}) | j_\mu | \dot{\phi}_{\nu L}^\alpha(\mathbf{r}) \rangle = \\ &= \frac{v^{\ell-\ell'-1}}{\hbar} \Gamma_{LL'}^\mu \left[(E_{\nu\ell}^\alpha - E_{\nu\ell'}^\alpha) K_{\ell\ell'}^\alpha + J_{\ell\ell'}^\alpha - J_{\ell\ell'}^\alpha - \mathcal{D}_{\ell\ell'}^\alpha \dot{\phi}_{\nu\ell}^\alpha(s_\alpha) \dot{\phi}_{\nu\ell'}^\alpha(s_\alpha) \right] \end{aligned}$$

The transition term $T^{jj'}(\mathbf{k})$ has to be written in terms of the normalized wave function. The normalizing factors for the wave functions are obtained from

$$\begin{aligned} N_{\mathbf{k}}^j &= \int d^3\mathbf{r} \Phi_{j\mathbf{k}}^*(\mathbf{r}) \Phi_{j\mathbf{k}}(\mathbf{r}) \\ &= \sum_L \sum_\alpha |\bar{c}_{L\alpha}^{j\mathbf{k}}|^2 \left\{ \mathcal{J}_{L\alpha}^{(1)} + 2(E^{j\mathbf{k}} - E_{\nu\ell}^\alpha) \mathcal{J}_{L\alpha}^{(2)} + (E^{j\mathbf{k}} - E_{\nu\ell}^\alpha)^2 \mathcal{J}_{L\alpha}^{(3)} \right\} \end{aligned} \quad (5.20)$$

where

$$\mathcal{J}_{L\alpha}^{(1)} = \int_0^{s_\alpha} |\phi_{\nu L}^\alpha(r)|^2 r^2 dr ; \quad \mathcal{J}_{L\alpha}^{(2)} = \int_0^{s_\alpha} \phi_{\nu L}^\alpha(r)^* \dot{\phi}_{\nu L}^\alpha(r) r^2 dr ; \quad \mathcal{J}_{L\alpha}^{(3)} = \int_0^{s_\alpha} |\dot{\phi}_{\nu L}^\alpha(r)|^2 r^2 dr.$$

Using the secular equation (5.14), the expression for the transition term becomes

$$\begin{aligned} T^{jj'}(\mathbf{k}) &= \left(N_{\mathbf{k}}^j N_{\mathbf{k}}^{j'} \right)^{-1/2} \left| \sum_\mu \sum_{LL'} \sum_\alpha \bar{c}_{L'\alpha}^{j'\mathbf{k}} c_{L\alpha}^{j\mathbf{k}} \left\{ \mathcal{I}_{LL',\mu}^{(1)\alpha} + (E^{j\mathbf{k}} - E_{\nu\ell}^\alpha) \mathcal{I}_{LL',\mu}^{(2)\alpha} \right. \right. \\ &\quad \left. \left. + (E^{j'\mathbf{k}} - E_{\nu\ell'}^\alpha) \mathcal{I}_{LL',\mu}^{(3)\alpha} + (E^{j\mathbf{k}} - E_{\nu\ell}^\alpha)(E^{j'\mathbf{k}} - E_{\nu\ell'}^\alpha) \mathcal{I}_{LL',\mu}^{(4)\alpha} \right\} \right|^2. \end{aligned} \quad (5.21)$$

The equation (5.12) provides an expression for the optical conductivity where both the transition matrix and the energy-resolved JDOS are expressed as functions of energy and frequency. As we shall show in a subsequent work, that within the ASR formalism this is the form in which the information about the constituents are input, and the configuration-averaged correlation function for the alloy may be expressed as

$$\ll S(\omega) \gg = (\pi/3) \int dE T^{\text{eff}}(E, \omega) \ll J(E, \omega) \gg \quad (5.22)$$

where

$$\ll J(E, \omega) \gg = \ll n_v(E) \gg \ll n_c(E + \omega) \gg \left[1 + \Lambda(E, \omega) \ll J(E, \omega) \gg \right]$$

and

$$T^{\text{eff}}(E, \omega) = \ll T(E, \omega) \gg + \delta T(E, \omega, \Sigma(E, \omega))$$

where $\Sigma(E, \omega)$ is the self-energy due to disorder scattering and $\Lambda(E, \omega)$ the corresponding vertex correction.

5.3 Application to perovskite alkaline-earth titanates

Perovskite structured titanate ferroelectric compound has been, to date, one of the most extensively investigated materials. They are extremely interesting from the viewpoint of solid-state theoreticians because their structures are a lot simpler than those of any other ferroelectric material known and, therefore, they prove to be rather simple systems to study in order to better understand the ferroelectric phenomenon. The titanates are very easily prepared as polycrystalline ceramics; they are chemically and mechanically fairly stable and they exhibit a paraelectric-to-ferroelectric phase transition at or above room temperature. Continued interest in these compounds has led to a wide variety of theoretical and experimental work, specially on lattice vibrations. A less common approach has been those based on electronic structure calculations (Castet-Mejean 1986). Michel-Calendini and Mesnard 1971, 1973 have reported the band structure of BaTiO_3 within a linear combination of atomic orbitals (LCAO) method with empirical off-diagonal integrals. The pioneering work on SrTiO_3 was that of Kahn and Leyendeker 1964. This was followed by an augmented plane wave (APW) calculation by Mattheis 1972 and a self-consistent tight-binding calculation by Soules *et al* 1972. However, Battaye *et al* 1976 have compared experimental valence band spectra with these early theoretical predictions and have concluded that the agreement was not satisfactory. Pertosa and Michel-Calendini 1978 carried out a modified tight-binding calculation on BaTiO_3 and SrTiO_3 and compared their results with X-ray photoelectron spectra. These authors introduced inner orbital interactions. Perkins and Winter 1983 have carried out LCAO calculations on the band structure of SrTiO_3 . There have been several all-electron, full-potential linearized augmented plane waves (FP-LAPW) studies of the titanates in recent times (Cohen and Krakauer 1990, 1992, Singh and Boyer 1992). In addition, studies based on ultrasoft-pseudopotential local density approximation (LDA) on perovskites have been

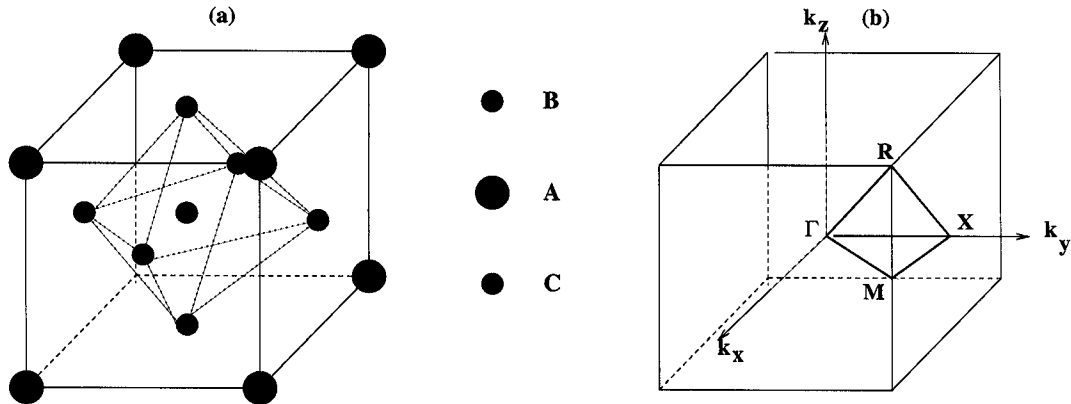


Figure 5.1: (a) Cubic unit cell for a perovskite ABC_3 . (b) The Brilluoin zone for the cubic phase.

carried out by King-Smith and Vanderbilt 1992, 1994. In comparison, electronic structure calculations on CaTiO_3 have been fewer. Ueda *et al* 1998, 1999 have used the first-principles tight-binding method to study CaTiO_3 .

We shall show that for all three compounds the transition rate, defined by us, is strongly energy and frequency dependent, i.e. it depends upon the energy of both the initial and the final states. We shall compare the theoretical results with experiment.

5.3.1 Electronic structure calculations

The primitive cell for the ideal perovskite structure ABC_3 is illustrated in figure 5.1(a). For the class of compounds we are interested in, the generic chemical formula is ABO_3 . A is a monovalent or divalent cation, B is a tetravalent or pentavalent metal. In the paraelectric phase there is full cubic symmetry. It can be thought of as lattice of corner-sharing oxygen octahedra with interpenetrating simple cubic lattices of A and B. The B cations sit at the centres of the octahedral O cages, while the A metal ions sit in the 12-fold coordinated sites between the octahedra. In our case the body-centre position is occupied by the Ti atom, the edges by alkaline-earth atoms and the face centres by O atoms. The space group is O_h^1 and the corresponding Brilluoin zone is shown in figure 5.1 (b). Both the A and B atoms are situated at sites with full cubic (O_h) point symmetry, while the O atoms have tetragonal (D_{4h}) symmetry.

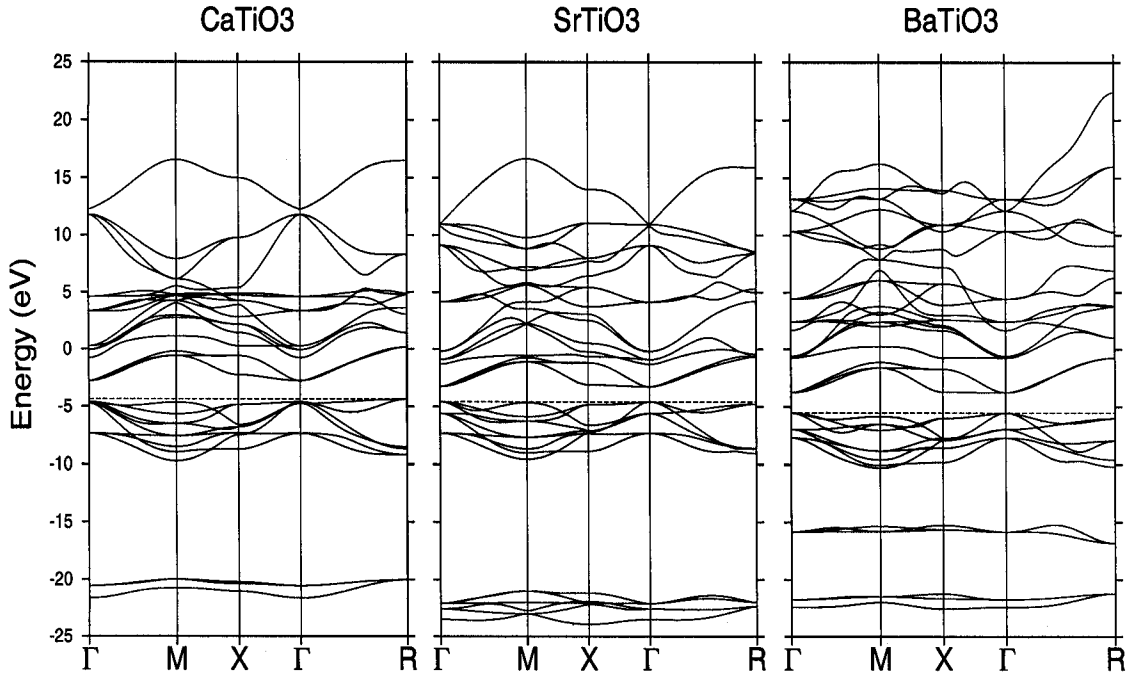


Figure 5.2: Band structures of CaTiO_3 , SrTiO_3 and BaTiO_3 (No scissors operation has been carried out in these calculations).

The electronic configurations of the alkaline-earth atoms are shown in table 5.1.

Since we wish to take into account the shallow core states, to include the transitions from these to the conduction band at large enough optical frequencies, the energy range is about 40 eV (3 Ryd.) and the single-panel LMTO cannot be made to be accurate over this range, we have carried out a two-panel calculation, with the $E_{\nu\ell}^\alpha$ lying in the lower energy range in one panel and in the upper energy range in the other. The minimal basis sets used in the two panels are shown in table 5.2.

Table 5.1: Electronic configurations of the alkaline-earth atoms.

Atom	Deep Core	Shallow Core	Valence	Unoccupied
Ca	$1s^2 2s^2 2p^6 3s^2 3p^6$	-	$4s^2$	3d 4p
Sr	$1s^2 2s^2 2p^6 3s^2 3p^6 3d^{10} 4s^2$	$4p^6$	$5s^2$	4d 5p 4f
Ba	$1s^2 2s^2 2p^6 3s^2 3p^6 3d^{10} 4s^2 4p^6 4d^{10} 5s^2$	$5p^6$	$6s^2$	5d 6p 4f
Ti	$1s^2 2s^2 2p^6 3s^2 3p^6$	-	$3d^2 4s^2$	4p
O	$1s^2$	-	$2s^2 2p^4$	3s 3d

Table 5.2: The minimal basis sets used in the lower and upper energy panels.

CaTiO ₃			
Lower Panel	Ca 4s 4p 3d	Ti 4s 4p 3d	O 2s 2p (3d)
Upper Panel	Ca 4s 4p 3d	Ti 4s 4p 3d	O 3s 2p (3d)
SrTiO ₃			
Lower Panel	Sr 5s 4p 4d (4f)	Ti 4s 4p 3d	O 2s 2p (3d)
Upper Panel	Sr 5s 5p 4d (4f)	Ti 4s 4p 3d	O 3s 2p (3d)
BaTiO ₃			
Lower Panel	Ba 6s 5p 5d (4f)	Ti 4s 4p 3d	O 2s 2p (3d)
Upper Panel	Ba 6s 6p 3d (4f)	Ti 4s 4p 3d	O 3s 2p (3d)

The states in parentheses are unfilled states which have been downfolded in our calculations. The figure 5.2 shows the band structure of the three titanates.

Let us first look at the leftmost figure for CaTiO₃. The Ca 3p core level lies around -27 eV and not shown in this figure. The narrow band around -20 eV is the O 2s band. The nine valence bands just below the Fermi level are derived from hybridized Ti 4s and O 2p. An indirect band-gap appears between the valence band top at the R point and the conduction band minimum at the Γ point. CaTiO₃ shows an indirect band-gap (Γ -R) of 1.6 eV, in the absence of the *scissors* operation. The experimentally reported indirect gap is 3.5 eV (Ueda *et al* 1998). This discrepancy is characteristic of the LDA upon which the TB-LMTO is based. In the conduction band region we have bands originating from (in ascending order of energy) Ti 3d- t_{2g} triplet, a singlet arising from Ca 4s and a doublet from Ti 3d- e_g . Then comes the bands which originate from the Ca 3d- e_g doublet and the Ca 3d- t_{2g} triplet. Finally we have the Ti 4p and Ca 4p based bands and finally the band based on Ca 4s. We note that for CaTiO₃, Ca and Ti 3d based bands overlap and hybridize in the conduction region.

For SrTiO₃, in the lower panel, the Sr 4p level now sits almost atop the O 2s band, giving rise to a rather broad (as compared to CaTiO₃) s-p hybridized band just below -20 eV. The subsequent analysis of the bands is rather similar to CaTiO₃. However, the band-gap is now direct and ~ 1.4 eV. Earlier band structure calculations of Mo *et al* 1999

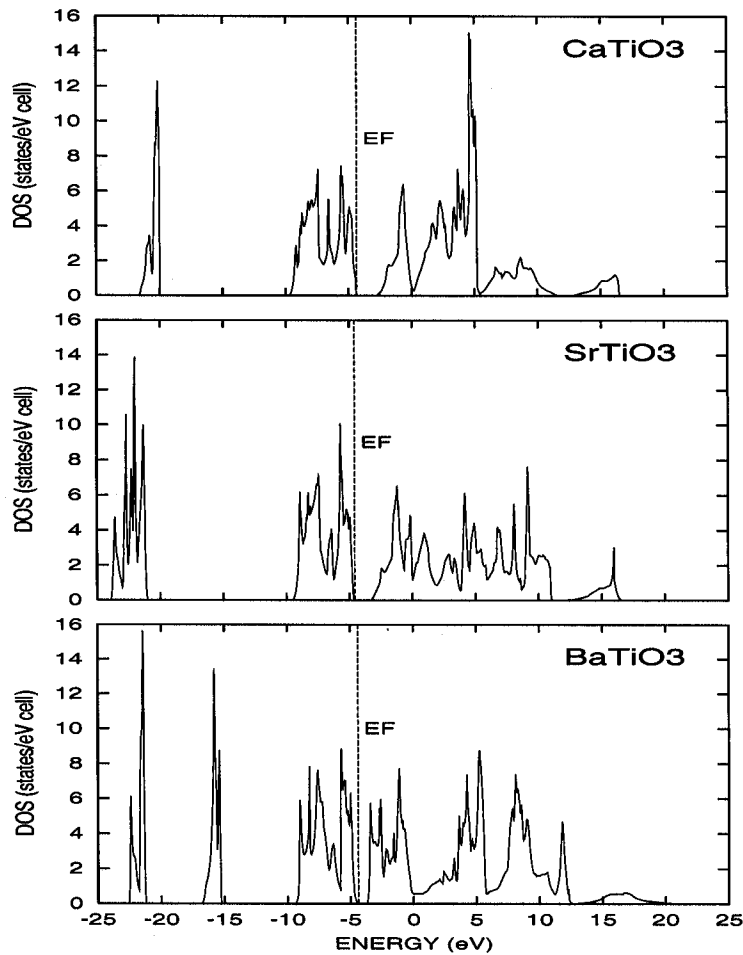


Figure 5.3: Densities of states for the three perovskite titanates.

and Kimura *et al* 1995 yield indirect band-gaps of ~ 1.45 eV and ~ 1.79 eV respectively. The experimental direct band-gap is around 3.2 eV.

For BaTiO_3 , in the lower panel, the Ba 5p shallow core level now crosses and lies above the O 2s band. The band-gap is direct and ~ 1.2 eV. The band structure is almost identical to the pseudopotential calculations of King-Smith and Vanderbilt 1992, 1994, whose band-gap was also direct and ~ 1.8 eV. The experimental band gap turns out to be ~ 3.2 eV (Wemple 1970).

For all three compounds, our calculations show a characteristic flatness of the lowest conduction band along Γ to X. This agrees with earlier works of Cardona 1965, Mattheis

1972, Harrison 1989, Wolfram and Ellialtioglu 1977, 1982 and King-Smith and Vanderbilt 1992, 1994. This observed flatness is related to certain unusual features in the density of states and optical conductivity, which appear to be characteristic of pseudo-two-dimensional systems.

Figure 6.3 shows the densities of states for the three titanates. The densities of states reflect the detailed band structure that we have described above. Earlier works on the density of states were based on different methods. Michel-Calendini and Mesnard 1971, 1973 and Pertosa and Michel-Calendini 1978 have used parameterized tight-binding and adjusted LCAO based methods for BaTiO_3 . Their density of states is in agreement with ours, with the band-gap difference characteristic of LSDA methods like the TB-LMTO. Similarly, Mattheis 1972 used the LCAO and Perkins and Winter 1983 used the extended Hückel basis for SrTiO_3 . Again their band structures and densities of states are in agreement with ours, with the exception of the band-gap. Even earlier works on SrTiO_3 by Zook and Casselman 1975 and Soules *et al* 1972 also show reasonable agreement. For CaTiO_3 we may compare our results with those of Ueda *et al* 1998, which agree reasonably well with our results.

5.3.2 Optical properties

In order to compute the transition rates as given in equation (5.11) one must perform integration over Brillouin zone, which we have done using tetrahedron method. In this method, the zone is divided into tetrahedra of equal volume (although this is not necessary condition), the mesh of \mathbf{k} -points defining the corners of each tetrahedron. The interpolated function is continuous at the boundaries of the tetrahedra and the irreducible Brillouin zone is completely divided into tetrahedra. The result of the interpolation is that the integrand depends only on the corner energies for a given energy band and the volume of the tetrahedra but not on their shape.

Figure 6.4 displays the transition rates $T(E, \omega)$ for the three titanates, shown here as functions of the initial energy of the excited electron and the incident photon energy (frequency). It is clear from the figure that the transition rate is strongly dependent on the energy-frequency variables for all the three compounds. The usual assumption of a

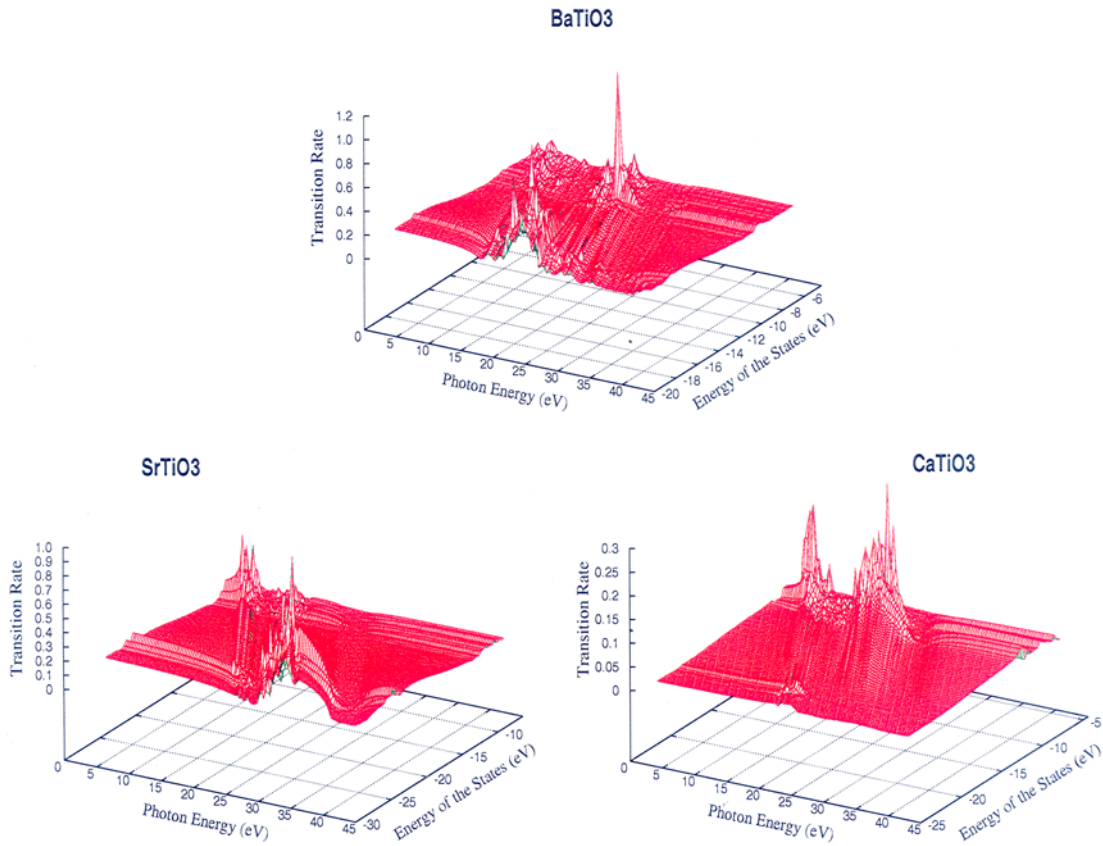


Figure 5.4: Transition rates for the three perovskite titanates shown as functions of initial energies and incident photon energies.

transition matrix weakly dependent on energy and frequency is certainly not valid in any of the three cases Saha *et al* 2000a-c.

In figure 5.5 we compare the imaginary part of the dielectric function with the scaled JDOS/ ω^2 . If the transition rate were independent of energy and frequency, they should be the same. The behaviours of the two are similar, but the relative weights of the structures across the frequency range are clear indications of the energy-frequency dependence of the transition rates.

CaTiO₃ : The effect of the energy-frequency dependence of the transition rate has a large effect on the optical properties of CaTiO₃. If we compare the results reported by

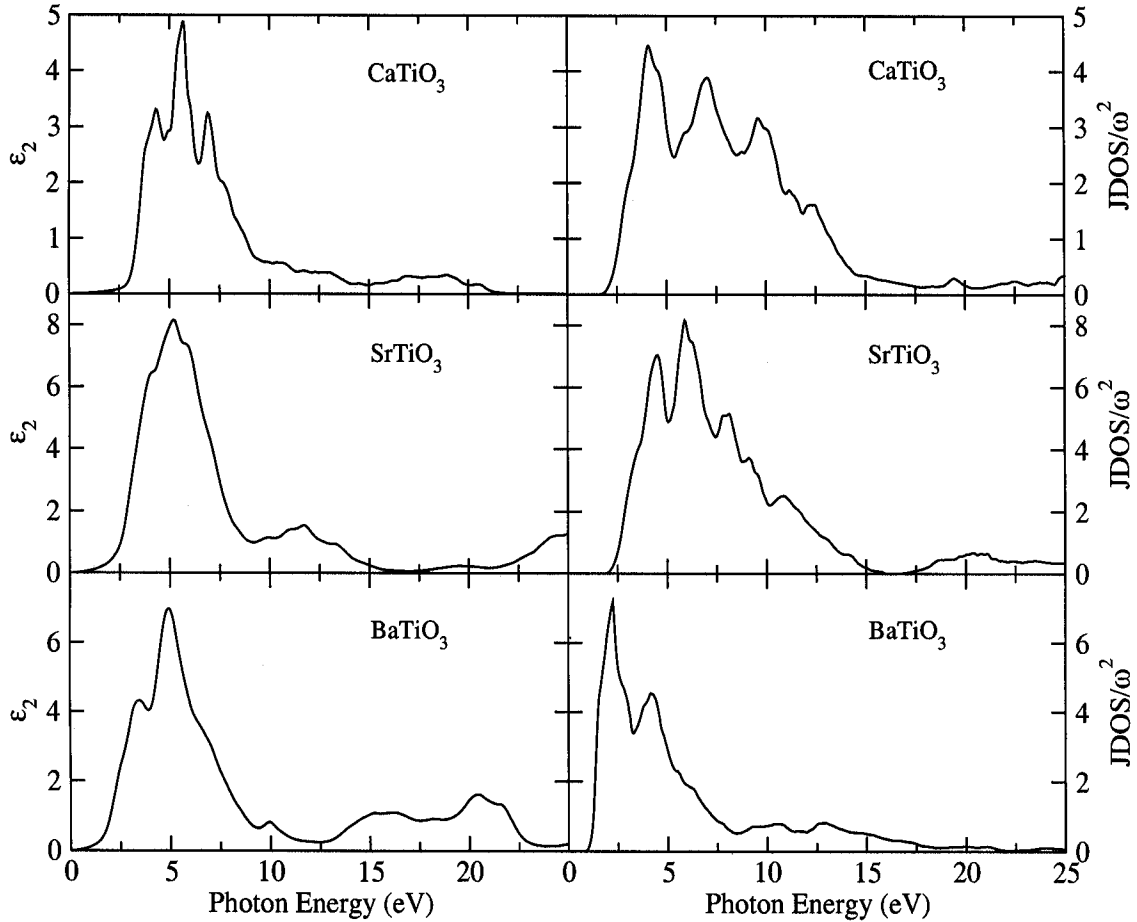


Figure 5.5: Comparison of the calculated imaginary part of the dielectric function (ϵ_2) (left), for the three perovskite titanates, with the same function calculated considering transition rate is constant (right).

Saha *et al* 2000c with our figure 5.6, we note that although in the earlier work the joint density of states does reproduce the peaks at lower-frequencies, the relative heights are not replicated. Looking at the lower panel of the figure, we may assign the peak at 4.5 eV to the transitions : O 2p \rightarrow Ti 3d- t_{2g} at the R and X points. The next and highest peak arises because of the nearby two unresolved peaks due to the transitions : O 2p \rightarrow Ca 4s at the M point (at 6.3 eV) and O 2p \rightarrow Ca 3d- e_g at the M point (at 6.8 eV). The third peak at 7.5 eV may be assigned to the transitions : O 2p \rightarrow Ti 3d- t_{2g} at the R point and O 2p \rightarrow Ca 3d- e_g at the X point. At higher frequencies, the theory does not tally well with experiment. The peak at 10 eV is not reproduced except as a shoulder. The real part

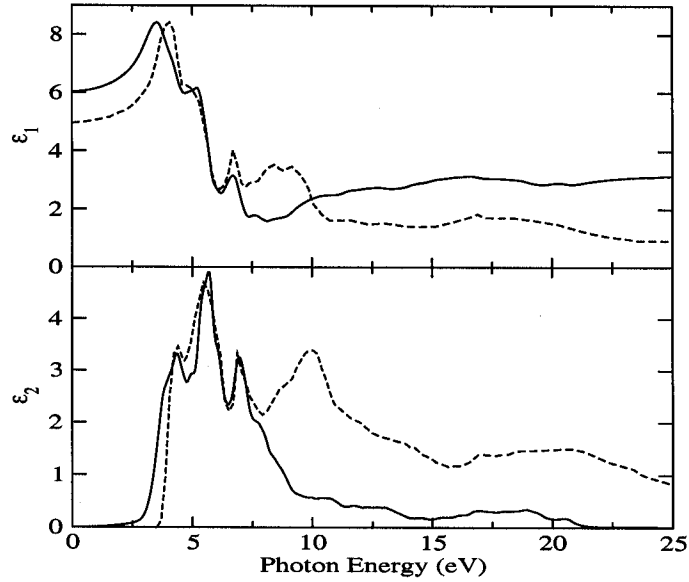


Figure 5.6: Comparison of calculated and experimental real parts $\epsilon_1(\omega)$ (top) and imaginary parts $\epsilon_2(\omega)$ (bottom) of dielectric function of CaTiO_3 as a function of photon energy: dotted curve is experimental (Ueda *et al* 1998, 1999); the continuous curve is theoretical.

of the dielectric function $\epsilon_1(\omega)$ is obtained by a Kramers-Krönig transformation from the imaginary part. This is shown in the top panel of figure 5.6. The discrepancies at high frequencies could be due to the fact that in the scissors type approach we have provided a rigid shift to the conduction bands. In a full fledged many-body GW technique, which is our ultimate aim to produce, the shift due to the self-energy will turn out to be energy (frequency) dependent.

SrTiO₃ : Let us now examine the figure 5.7. As in the case of CaTiO_3 , here too, the effect of energy-frequency dependence of the transition rate leads to the correct relative heights of the peaks in $\epsilon_2(\omega)$ being reported. The shoulder peak at around 4 eV may be attributed to the transitions O 2p at \rightarrow Ti 3d- t_{2g} and O 2p \rightarrow Ti 3d e_g both at the Γ point. The high peak at 5 eV is due to the O 2p \rightarrow Ti 3d- e_g at the Γ point. A third shoulder peak at 6 eV is due to the transition O 2p \rightarrow Ti 3d- e_g , also at the Γ point. As in the case of CaTiO_3 , the structure in the high-frequency part has both peaks lower and shifted to higher frequencies. The cause is the same as discussed above.

BaTiO₃ : Lastly, let us look at figures 5.6-5.8. If we compare the shape of the imaginary

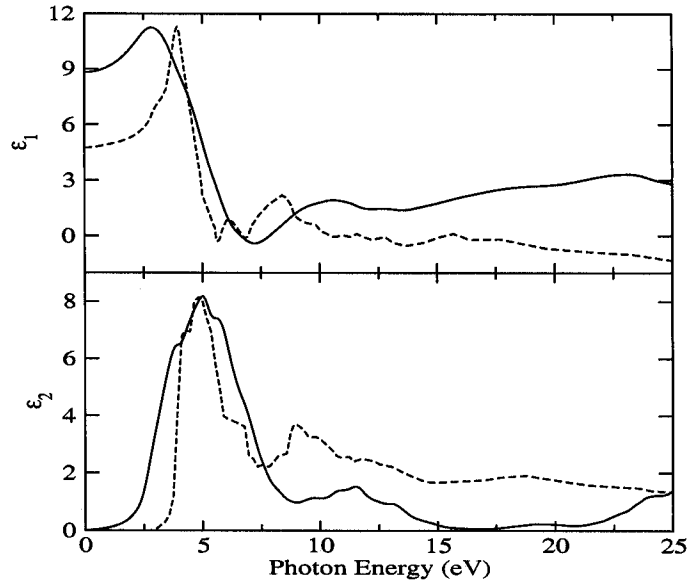


Figure 5.7: Comparison of calculated and experimental real parts $\epsilon_1(\omega)$ (top) and imaginary parts $\epsilon_2(\omega)$ (bottom) of dielectric function of SrTiO_3 as a function of photon energy: dotted curve is experimental (Bäuerle *et al* 1978); the continuous curve is theoretical.

part of the dielectric function $\epsilon_2(\omega)$ obtained by our accurate estimate of the transition rate with that of Saha *et al* 2000c, we note that agreement with experiment of Bäuerle *et al* 1978 is much better when we take the energy-frequency dependences of the transition matrix into account. The relative weights of the low-frequency peaks, at 3.8 and 5 eV are correctly reproduced here. The lower peak is attributed to the transition from the O 2p to the Ti 3d- t_{2g} band and from the O 2p to the Ti 3d- e_g band both at the Γ points. The next higher peak is there because of the transition from the O 2p to the Ti 3d- e_g band at the Γ point. Our present study also indicates a peak around 10 eV, and the features at higher frequencies follow the experimental results closely, although the amplitude seems to have been underestimated as compared to the low-frequency results. In all cases, although the lower-frequency part is much better reproduced, the high-frequency structures in the theoretical result are shifted upwards.

As before, we argue that this is probably an artifact of the rigid shift of the scissors-type approach. A energy-frequency dependent self-energy of the type given by the GW method should provide the necessary correction. In addition, the wrong heights at higher

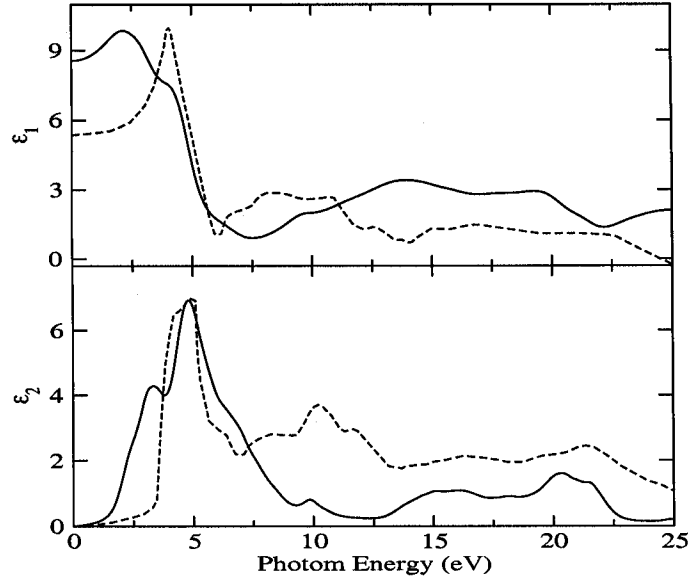


Figure 5.8: Comparison of calculated and experimental real parts $\epsilon_1(\omega)$ (top) and imaginary parts $\epsilon_2(\omega)$ (bottom) of dielectric function of BaTiO₃ as a function of photon energy: dotted curve is experimental (Bäuerle *et al* 1978); the continuous curve is theoretical.

frequencies could also arise from the fact that we have neglected transitions to some of the higher-energy conduction bands. A more complete, perhaps a three panel calculation at higher energies, should correct this. Alternatively, we could use the higher-order NMTOs (Andersen and Saha-Dasgupta 2000), since they span a much larger energy range.

5.4 Application to the defect-chalcopyrite ZnIn₂Te₄

The ternary semiconducting compounds of the types $A^{II}B_2^{III}C_4^{VI}$ and $A^{II}B_3^{III}C_5^{VI}$ have been widely investigated because of their potential applications in electro-optic, optoelectronic, and nonlinear optical devices (Georgobiani *et al* 1985, Schmid *et al* 1993, Nelson *et al* 1994, Marin *et al* 1998, Rincon *et al* 1998, Wasim *et al* 1998, Matsumoto *et al* 1999, Rincon *et al* 2000, Ozaki and Adachi 2001, Rincon 2002, Rincon *et al* 2003). Most of these compounds have the *ordered defect-chalcopyrite* (space group = $S2_4$) or *stanite* (space group = D_{2D}^{11}) structures (Madelung 1985, Hahn *et al* 1995). Detailed experimental studies of physical properties of ZnIn₂Te₄ (Matsumoto *et al* 1999, Ozaki and Adachi 2001) and CuIn₃Te₅, CuGa₃Te₅ and CuIn₃Se₅ (Schmid *et al* 1993, Marin *et*

et al 1998, Nelson *et al* 1994, Wasim *et al* 1998, Rincon *et al* 2000, Rincon 2002, Rincon *et al* 2003) have appeared in literatures in recent times. The technological importance of these compounds have arisen due to the fact that these materials are expected to play an important role in the optimization of the efficiency of solar cells (Yang *et al* 1994).

In the defect-chalcopyrite family ZnIn_2Te_4 is known to have an ideal chalcopyrite structure, i.e. its lattice parameters are simply given by $\alpha = \beta = a/4$, $\gamma = c/8$, and $c = 2a$, as shown in figure 5.9. Although the material has been in the subject of many research efforts, many fundamental properties have not been sufficiently evaluated or are even unknown. So our aim is to investigate the electronic and optical properties of this system from a first-principles NMTO based calculations.

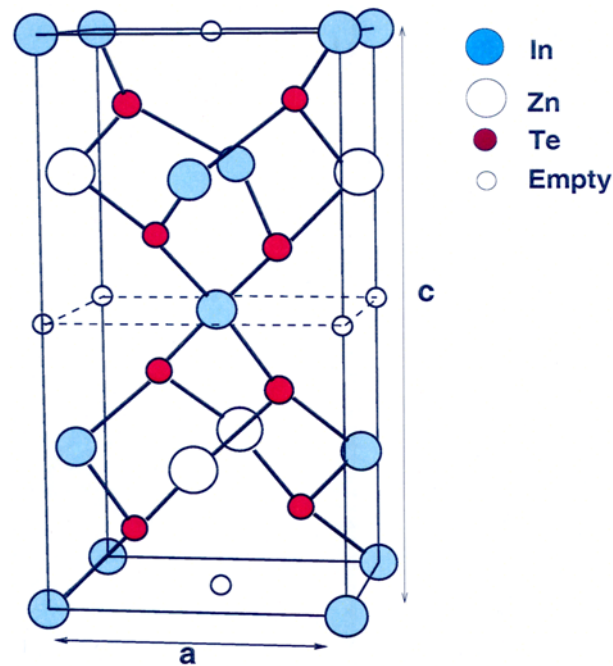


Figure 5.9: Crystal structure of defect-chalcopyrite-type semiconductor ZnIn_2Te_4 . We show the orthorhombic primitive cell with two molecules per cell.

The reason of choosing this system is that, it is not only important for its applications

in technology, but is also of academic interest. This is because this could permit us to understand the role that arrays of vacancies or impurities play in influencing their crystal structure, electrical and optical properties. The academic importance of its study is also associated with the study of nano-materials. There is growing interest in the study of defect- and nano-structures (Myers *et al* 1992, Domain and Becquart 2001). One of the experimental methods for the preparation of nano-structures is to fill in the structural voids in a *host* compound with atoms of a given substance. These structural voids could either be local void clusters or even tubular voids. The host compound helps to form a matrix in which these nano-structures stabilize. We shall first try to understand the properties of the host material and in a subsequent work, we shall extend the present work to include inserted nano-structures within the host.

Recently Matsumoto *et al* 1999 and Ozaki and Adachi 2001 have carried out a detailed experimental and theoretical study of optical properties of amorphous and crystalline ZnIn_2Te_4 . There are few other experimental measurements (Manca *et al* 1974, Neumann *et al* 1990a, Neumann *et al* 1990b, Manca *et al* 1993) on the compound also, but there does not seem to have been any first principles calculations for the electronic structure and optical properties of this material. The band structure calculations by empirical parameterized tight-binding methods has been carried out for ZnIn_2Te_4 by Meloni *et al* 1976 and Ozaki and Adachi 2001. These calculations required fitted parameters. The actual crystal structures also seem to have been simplified. Meloni *et al* 1976 have assumed a pseudo-cubic (space group = V_d^1), rather than the defect-chalcopyrite structure.

The X-ray diffraction studies by Matsumoto *et al* 1999 and Ozaki and Adachi 2001 indicate a structure for this compound as shown in figure 5.9. Their crystal structure determinations agree with the structure studies of Hahn *et al* 1995. An orthorhombic unit cell contains two molecular units. It is formed by stacking two cubic units of the defect-chalcopyrite structure on top of each other and then sliding the top cube along the (110) direction with respect to the bottom a distance equal to half the diagonal. This produces an anti-phase-like boundary between the two cubic cells. There are two Zn, four In and eight Te atoms in the unit cell, together with two vacancies. The table 5.3 gives the coordinates of the inequivalent atoms in the unit cell. Because of the vacancies, this structure does not have the full symmetry of a chalcopyrite structure ($I\bar{4}2d$). The space

Table 5.3: Positions within the unit cell of atomic basis, including the empty spheres to take into account the vacancies within the structure.

Atom type	Positions			Atom type	Positions		
Zn1	a/2	0	c/4	Te1	-a/4	a/4	c/8
Zn2	0	a/2	3c/4	Te2	a/4	a/4	3c/8
In1	a/2	a/2	0	Te3	a/4	-a/4	c/8
In2	0	a/2	a/2	Te4	-a/4	-a/4	3c/8
In3	0	0	c/2	Te5	a/4	a/4	5c/8
In4	a/2	0	3c/4	Te6	-a/4	a/4	7c/8
E1	0	0	0	Te7	-a/4	-a/4	5c/8
E2	a/2	a/2	c/2	Te8	a/4	-a/4	7c/8

group, $\bar{I}42d$ is a *nonsymmorphic space group*. This is incompatible with the structure shown in figure 5.9. The valid space group is $\bar{I}4$.

The positions of Te's are zinc-blende type, i.e. two inter-penetrating fcc lattices shifted one-fourth of the way along a body diagonal. The values of the lattice parameters a and c are taken from experiment to be 6.11 and 12.22 Å respectively as reported by Hahn *et al* 1995 and Ozaki and Adachi 2001.

In the next section, we shall investigate the electronic energy-band structure and optical properties of crystalline ZnIn_2Te_4 . The calculation will be done within the framework of the self-consistent LMTO and NMTO method. We shall also have a qualitative comparison of these results with the available experimental results.

5.4.1 Electronic structure calculations

We first note that for the calculation of the optical properties of the solid we need to span a large energy range, from the occupied valence to the unoccupied conduction states. For ZnIn_2Te_4 this spans a range from -15 to 11 eV. This is shown in figure 5.10. For the usual TB-LMTO self-consistency cycles, we choose the *nodal* energy $E_{\nu\ell}^\alpha$, around which we expand wave function, just below the Fermi level. For example, for ZnIn_2Te_4 this energy is around -5 eV, i.e. in the valence band region. So the band structure based

on TB-LMTO method is quite accurate near the nodal energy. The higher region of the conduction band, which is away from the nodal energy is not accurately reproduced. Is it possible to shift some of the nodal energies to higher values and redo the calculations? If the answer is yes, one may carry out multi-panel calculations in different energy windows. Although in this case, one may require careful downfolding (Andersen 1975) in order to avoid ghost bands. These difficulties are avoided in the recently developed order-N muffin-tin orbitals method (NMTO) (Andersen and Saha-Dasgupta 2000), which expands the wave function in term of a basis which is expressed as a Lagrange interpolation around a discrete set of *nodal* energies $\{\epsilon_n\}$:

$$\Phi_{j\mathbf{k}}(\mathbf{r}) = \sum_{LL'} \sum_{\alpha} c_{L\alpha}^{j\mathbf{k}} \left[\sum_{n=0}^N \phi_{nL'}^{\alpha}(\mathbf{r}) L_{n,LL'}^{(N)}(\mathbf{k}) \right]. \quad (5.23)$$

The $L_{nRL,R'L'}^{(N)}$ are Lagrange matrices which are such that the energy dependent partial wave basis $\phi_L^{\alpha}(\mathbf{r}, E)$ takes the values $\phi_{nL}^{\alpha}(\mathbf{r})$ at the *nodal* energies. Unlike the LMTO, the *nodal* energies are independent of the indices $L\alpha$. By choosing the *nodal* energies across the energy range of interest we can accurately reproduce the bands in that range. It requires a simple one-panel calculation. This was shown for GaAs in the range -15 to 20 eV by Andersen and Saha-Dasgupta 2000.

The right-hand panel in figure 5.10 shows the energy bands obtained from the NMTO using three *nodal* energies spread across the energy range of interest. In comparison with the left-hand panel in figure 5.10 showing the band structure calculated from the TB-LMTO, we note that the largest change occurs in the conduction band, away from the TB-LMTO nodal energies bunched below -5 eV. We have used the von Barth-Hedin exchange (von Barth and Hedin 1972) with 512 \mathbf{k} -points in the irreducible part of the Brillouin zone.

The calculated density of states within TB-LMTO and NMTO are shown in the figure 5.11. It is evident from these two figures that there is significant difference between these two only in the conduction band. From the band structure comparison, this was also evident for the reasons discussed earlier. These densities agree quite well with the experimental XPS measurements of Ozaki and Adachi 2001 and also with their parametrized tight-binding calculations. These results are shown in the figure 5.12. It must be noted here that since these calculations are based on the LDA, we do obtain a lower band-gap.

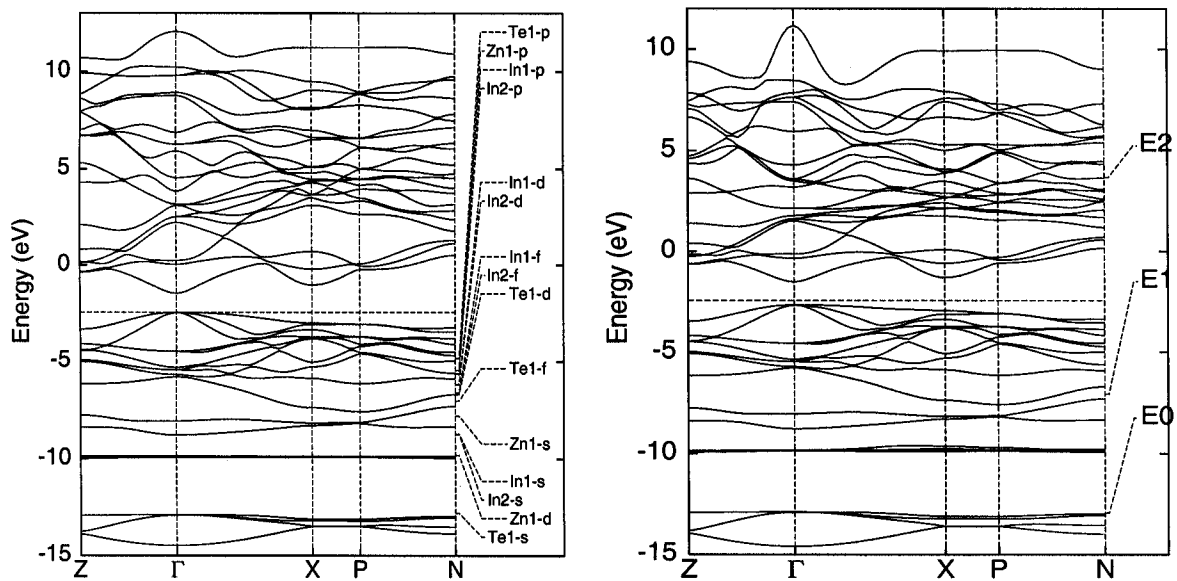


Figure 5.10: The band structure of ZnIn_2Te_4 calculated from the TB-LMTO (left) and the NMTO (right) with three nodal energies across the energy range.

Figure 5.10 shows that, both in the TB-LMTO and the NMTO, a direct band-gap of around 1.33 eV (TB-LMTO) and 1.37 eV (NMTO) occurs at the Γ point. The absorption coefficient measurements by Ozaki and Adachi 2001 also indicate a direct band-gap of around 1.4 eV. Different experimental measurements report values of the band-gap varying between 1.3 and 1.87 eV (Boltivets *et al* 1969, Manca *et al* 1974, Manca *et al* 1993). Since the calculations are based on the LDA, we cannot have much confidence about the conduction bands. This problem can be tackled more accurately, for example, through by quasi-particle band structure within a GW type approximation (Aulbur 2000). These NMTO based calculations are a much better starting point of GW self-consistency iterations than the first or second generation LMTOs (see comments in Andersen and Saha-Dasgupta 2000).

The TB-LMTO band structure gives us insight into the various structures in the density of states. At the lowest energies around -14 eV we have the states arising out of the Te s electrons. The sharp peak at -10 eV is due to the very narrow Zn d bands. The next structures around -8 eV arise from the In s and Zn s electrons. The predominantly

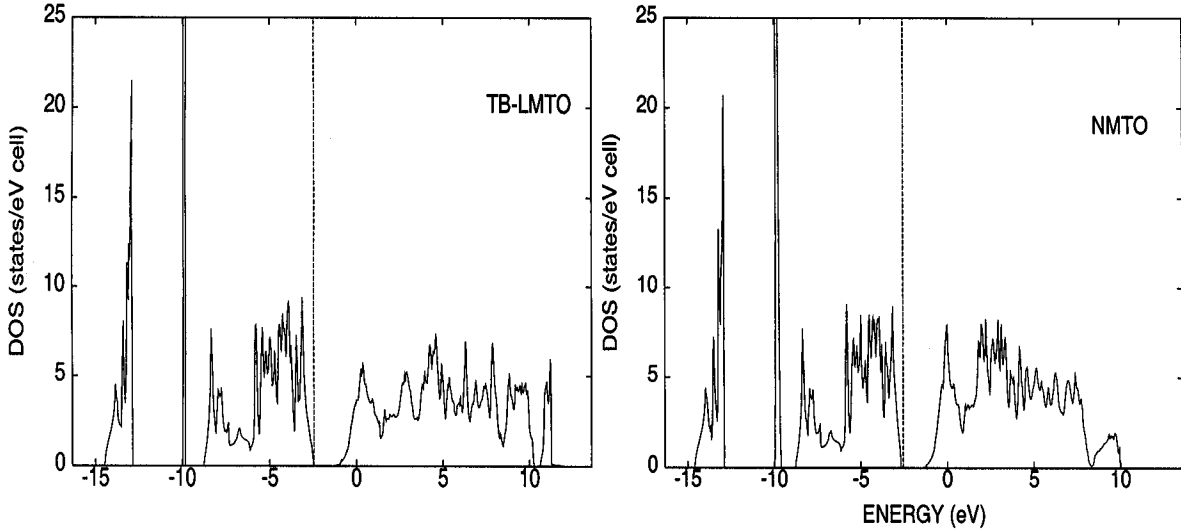


Figure 5.11: Density of states for ZnIn_2Te_4 (left) calculated from the TB-LMTO and (right) calculated from NMTO.

covalently bonded Te sp and In sp states gives rise to bonding and anti-bonding bands around -5 eV and 5 eV respectively. The band-gap lies between these bands.

5.4.2 Optical properties

In section 5.2, we have already described the methodological details of studying optical conductivity within the LMTO basis. However, in the previous subsection we mentioned that one may improve excited states calculations using NMTO. In this section, we shall investigate optical spectra of ZnIn_2Te_4 on the basis of both LMTO and NMTO method. We shall also try to have a comparison of these results with the available experimental data.

We first note that our LDA-based calculations of dielectric functions figure 5.13 give a smaller band-gap than that of experiment. We may apply the *scissors* operator, which involves a rigid shift of the conduction band with respect to the valence band, so that the band-gap matches. This is frequently used by LDA practitioners, but cannot be fully justified. The correct procedure would be to carry out a full GW calculation (Aulbur 2000) which gives rise to an energy dependent self-energy. This shifts the bands unequally at different energies, resulting in a distortion of the shape of the densities of states as well.

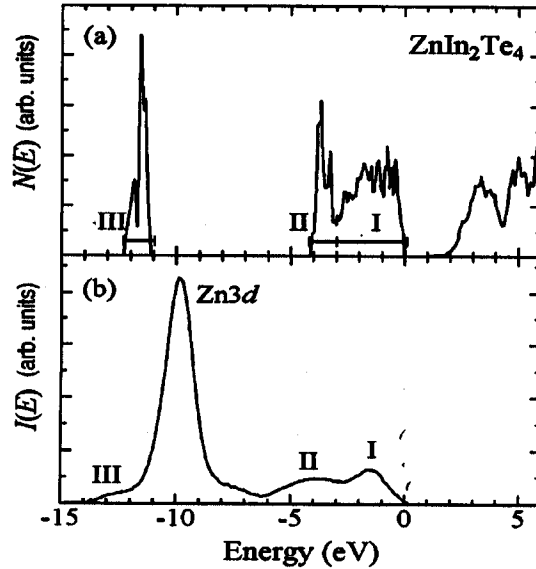


Figure 5.12: (a) Theoretical density of states $N(E)$ and (b) experimental XPS spectrum $I(E)$ taken from Ref. Ozaki and Adachi 2001.

Given this, the agreement of our theoretical calculations with the experimental results of Ozaki and Adachi 2001 available up to 10 eV photon energies, is not bad. In particular if we examine the NMTO calculations of the imaginary part of the dielectric function $\epsilon_2(\omega)$ and compare it with the experimental observation (lower panel in figure 5.13), we note that most of the experimental structures : the shoulder at around 2 eV, the twin peaks between 3 and 4 eV and the lower peak around 5 eV are reasonably well reproduced. The TB-LMTO calculation of $\epsilon_2(\omega)$ is shown at the top of figure 5.13. Although the structures are seen around the same photon energies, the relative weights are in much worse agreement with experiment. The origin of this disagreement is the worse representation of the conduction band, particularly near the upper edge of the gap.

The unit cell of the defect-chalcopyrite structure indicates the asymmetry in the c -direction. There is no reason therefore that the optical response will be same when the polarization is along the a and c -axes. Since the experiment did not align the crystal axis with the polarization of the electric field, we have compared the results with the direction averaged response. For reference we have also shown in figure 5.14 the $\epsilon_2(\omega)$ with polarizations along the a and c axes.

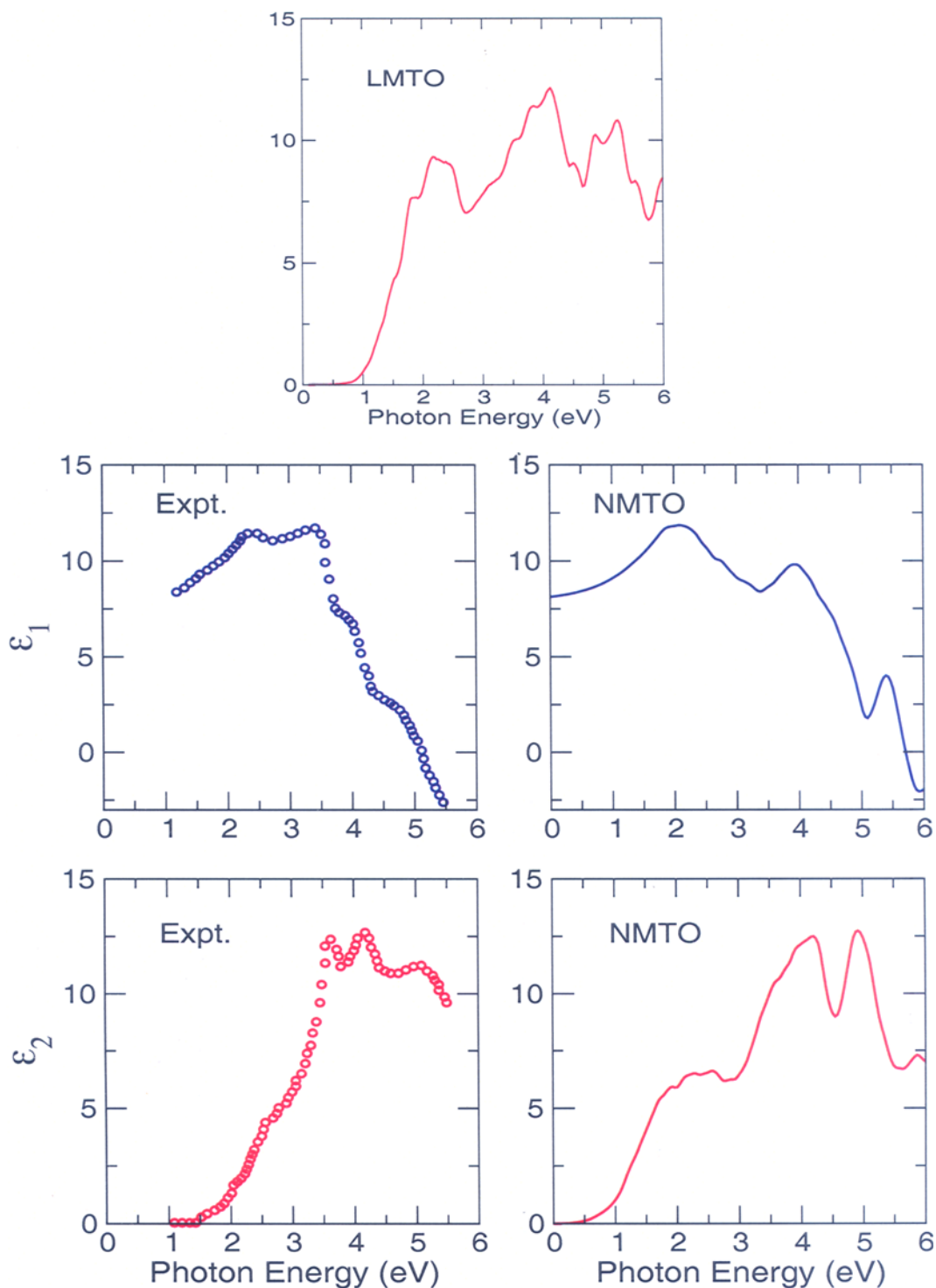


Figure 5.13: (Top) imaginary part (averaged over all photon polarizations) of the dielectric function of ZnIn_2Te_4 from an LMTO calculation, (Right panel) real and imaginary parts of dielectric function based on NMTO calculation, and (Left panel) the experimental results of Ozaki and Adachi 2001. Photon energy is shown in the unit of eV.

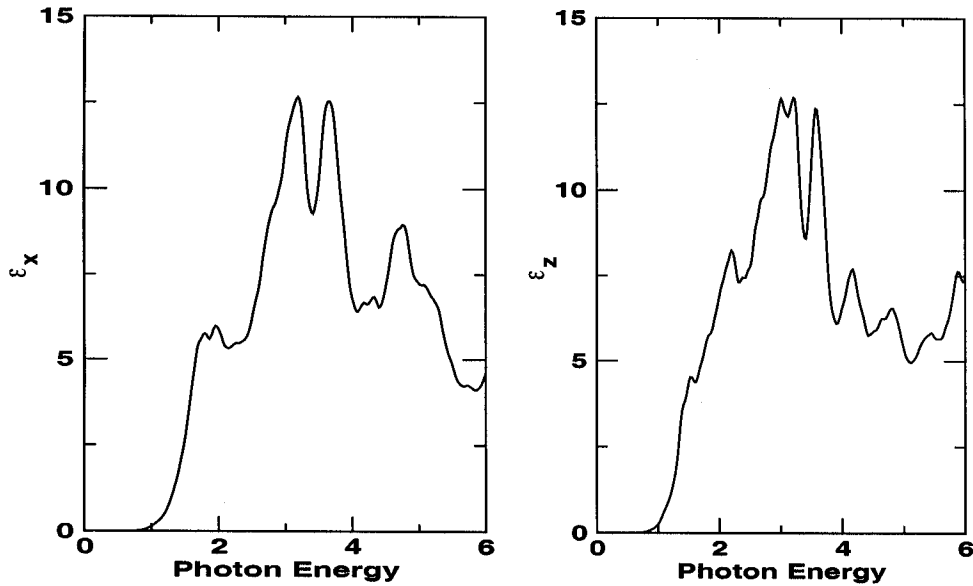


Figure 5.14: The imaginary parts of the dielectric function with incident photon polarizations perpendicular and parallel to the c -axis. Photon energy is shown in the unit of eV.

We shall conclude with the remark on the two directions which we propose to take from here. The first point is to recognize that the NMTO calculations form a reasonable starting point of the more sophisticated many-body GW approaches. The second is related to the reason why we chose to study the defect-chalcopyrite in the first place. We would like to fill the voids in the structure with various “impurities” and study the signal for these in the optical response. These will be the aim of our subsequent work in this area.

5.5 Conclusions

We have proposed here a modified expression for the optical conductivity as a convolution of an energy-frequency dependent transition matrix and the energy-resolved joint density of states. The main motivation was to generalize it to disordered systems, where the traditional reciprocal-space formulation breaks down due to the failure of Bloch’s theorem. In order to gain confidence in our new formulation we have applied it here to the three alkaline-earth perovskite titanates in their paraelectric phases. The results within the LMTO calculations are in reasonable agreement with experimental data. To improve

the theoretical results in their higher frequency region, we also performed NMTO based calculations on defect-chalcopyrite semiconductor ZnIn_2Te_4 . These results show even better agreement with the experimental results. The band-gaps came out from both LMTO and NMTO calculations are close to the experimentally measured value. The agreement of theoretical results with experiment are as good as we can expect from a LDA calculation. This formulation can now form the starting point for a generalization to disordered systems, that is, combining with the ASR to random binary alloys. This we shall elaborately report in the next chapter.

Chapter 6

Optical properties of disordered alloys

6.1 Introduction

The object of our present study is to present a formulation for obtaining the configuration-averaged optical conductivity for random alloys. Because of randomness, there is a need to go beyond the usual reciprocal-space-based formulations for crystalline compounds. Instead of labelling the electronic states by the Bloch wave vector and band index (\mathbf{k}, j) , which is suitable for crystalline compounds, we have to label them by energy and the composite angular momentum $L = (\ell, m, m_s)$. In cases where the disorder is substitutional and *homogeneous*, in the sense that the occupation probabilities of lattice sites by atom species are independent of the site label, we can still label the configuration-averaged quantities by the reciprocal wave vectors. However, the band picture breaks down, and we cannot use the band index labeling of quantum states as in crystalline materials. Substitutional disorder dictates that we begin with a purely real-space representation and we have chosen the minimal basis set of the TB-LMTO method (Andersen 1975). Configuration averaging over various random atomic arrangements has been carried out using the augmented space formalism (ASF) introduced by us earlier for the study of electronic properties of disordered systems (Mookerjee 1973, Kaplan and Gray 1977, Saha *et al* 1996, Dasgupta *et al* 1997, Ghosh *et al* 1999). The ASF goes beyond the usual mean-field approaches and takes into account configuration fluctuations. This formalism has been described in detail in the referenced articles and the interested reader

⁰The contents of this chapter is being published in : (1) **K K Saha** and A Mookerjee, *Phys. Rev. B* **70** 134205 (2004) and (2) **K K Saha** and A Mookerjee, *Phys. Rev. Lett.* (2004) (submitted).

can go into the details in them. The contribution of this work will be to show that the disorder-induced corrections to the averaged current terms in the optical conductivity are directly related either to the disorder-induced self-energy in the propagators or to vertex corrections. Since the self-energy and the vertex corrections can be calculated for realistic binary alloy systems, either within an augmented space recursion (Saha *et al* 1996, Dasgupta *et al* 1997, Ghosh *et al* 1999) or within one of the mean-field approaches (Kaplan and Gray 1977), this formulation will form the basis of subsequent calculations in real alloys.

6.2 The optical conductivity

For the mathematical formulation we shall start with the equation (5.3) of the previous chapter.

$$S_{\mu\nu}(\omega) = \text{Im} \int_{-\infty}^{\infty} dt e^{izt} \langle \Phi_0 | j_{\mu}(\tau) j_{\nu}(0) | \Phi_0 \rangle, \quad z = \omega + i0^+.$$

In case there is no anisotropy, an expression for the correlation function, at $T = 0$ K, can be obtained via the Kubo-Greenwood expression,

$$S(\omega) = \frac{1}{3\pi} \sum_{\gamma} \int dE \text{Tr} \left[\mathbf{j}_{\gamma} \text{Im}\{\mathbf{G}^v(E)\} \mathbf{j}_{\gamma}^{\dagger} \text{Im}\{\mathbf{G}^c(E + \omega)\} \right]. \quad (6.1)$$

We have assumed isotropy of the response so that the tensor $S_{\mu\nu}$ is diagonal and we have defined $S(\omega)$ as the direction averaged quantity $\frac{1}{3} \sum_{\mu} S_{\mu\mu}(\omega)$. \mathbf{j}_{γ} is $\hat{e}_{\gamma} \cdot \mathbf{j}$, and \hat{e}_{γ} is the direction of polarization of the incoming photon. The operators $\mathbf{G}^v(E)$ and $\mathbf{G}^c(E)$ are the resolvents of the Hamiltonian projected onto the subspaces spanned by the occupied and the unoccupied one-electron states.

The trace is invariant in different representations. For crystalline systems, usually the Bloch basis $\{|\mathbf{k}, j\rangle\}$ is used. For disordered systems, prior to configuration-averaging, it is more convenient to use the real-space based screened (or tight-binding) muffin-tin orbitals as a basis $\{|RL\rangle\}$.

If we define

$$\mathcal{S}_{\gamma}(z_1, z_2) = \text{Tr} \left[\mathbf{j}_{\gamma} \mathbf{G}^v(z_1) \mathbf{j}_{\gamma}^{\dagger} \mathbf{G}^c(z_2) \right], \quad (6.2)$$

then the above equation becomes

$$S(\omega) = \frac{1}{12\pi} \sum_{\gamma} \int dE \left[\mathcal{S}_{\gamma}(E^{-}, E^{+} + \omega) + \mathcal{S}_{\gamma}(E^{+}, E^{-} + \omega) - \mathcal{S}_{\gamma}(E^{+}, E^{+} + \omega) - \mathcal{S}_{\gamma}(E^{-}, E^{-} + \omega) \right], \quad (6.3)$$

where

$$f(E^{\pm}) = \lim_{\delta \rightarrow 0} f(E \pm i\delta).$$

We have used the Herglotz property of the Green operator,

$$\mathbf{G}(E + i\delta) = \mathbf{G}^r(E) - i \operatorname{sgn}(\delta) \mathbf{G}^i(E).$$

For disordered materials, we shall be interested in obtaining the configuration-averaged response functions. This will require the configuration averaging of quantities such as $\mathcal{S}_{\gamma}(z_1, z_2)$.

6.3 Configuration averaging

Any description of a disordered system must be from a statistical point of view, since the properties of these systems are random variables and any particular *configuration* is of little interest¹. Consequently, the study of configuration-averaged properties of disordered systems has received much attention.

Configuration averaging for response functions in disordered materials has had some history. The Ziman-Faber theory (Ziman 1961, Bradley *et al* 1962, Faber and Ziman 1965), much in use for liquids, is valid for electrons, weakly scattered from a dilute distribution of impurities. The extended version of this theory was proposed by Evans *et al* 1980, but this too overlooks multiple scattering effects, as pointed out by Roth and Singh 1980. An effective medium approach (EMA) was proposed by Roth 1974 and developed further by Asano and Yonezawa 1980, Singh and Roth 1980, and Roth and Singh 1980. This approach does take into account multiple scattering effectively and, as we shall see, will have close similarities with the approach we propose in this chapter. Velický 1969

¹This statement has to be modified in some situations, like localized states in band tails, where unlikely configurations play an important role and configuration averaging is not meaningful.

has developed an expression for configuration-averaged response functions in random alloys for simple tight-binding models with one orbital per site and diagonal disordered within the coherent-potential approximation (CPA). Brouers and Vedyayev 1972 have extended the formalism to transition-noble metal alloys. The CPA-like mean-field approach has been applied to response functions by Niizeki and co-workers (Hoshino and Watabe 1977, Niizeki 1977a-c, Niizeki and Hoshino 1977), who extended the pioneering work of Velický 1969 to longer-ranged random potentials. Mookerjee 1973 has introduced the ASF to tackle configuration averaging. Within this formalism, he studied the role of macroscopic conservation laws on the response functions, leading to a Ward identity between the vertex corrections and the self-energy (Mookerjee 1976). Within the CPA, vertex corrections were obtained by ingenious diagram summations by Leath 1970. There have been CPA calculations by Harris and Plischke 1972 and Nauciel-Bloch and Riedinger 1974. In a series of papers, Mookerjee and co-workers (Mookerjee 1975, Mookerjee *et al* 1985, Mookerjee and Thakur 1988) have applied the ASF to conductivity and optical conductivity in random alloys. This will form the background of our present development.

The ASF has been described in chapter 1. Within the ASF, the configuration-averaged Green function is given by (Ghosh *et al* 1999) :

$$\ll \mathbf{G}(z) \gg = \langle 1 | (z\tilde{\mathbf{I}} - \tilde{\mathbf{H}}^{\text{eff}})^{-1} | 1 \rangle, \quad (6.4)$$

where

$$\tilde{\mathbf{H}}^{\text{eff}} = \sum_R \left\{ \tilde{\mathbf{A}} \mathcal{P}_R \otimes \tilde{\mathbf{I}} + \tilde{\mathbf{B}} \mathcal{P}_R \otimes \mathcal{P}_R^\dagger + \tilde{\mathbf{F}} \mathcal{P}_R \otimes (\mathcal{T}_R^{\uparrow\dagger} + \mathcal{T}_R^{\downarrow\dagger}) + \sum_{R'} \tilde{\mathbf{V}}_{RR'} \mathcal{T}_{RR'} \otimes \tilde{\mathbf{I}} \right\}$$

where

$$\begin{aligned} \tilde{\mathbf{A}} &\equiv \tilde{A}_L \delta_{LL'} = A(C_L/\Delta_L)/A(1/\Delta_L) \delta_{LL'}, \\ \tilde{\mathbf{B}} &\equiv \tilde{B}_L \delta_{LL'} = B[(C_L - z)/\Delta_L]/A(1/\Delta_L) \delta_{LL'}, \\ \tilde{\mathbf{F}} &\equiv \tilde{F}_L \delta_{LL'} = F[(C_L - z)/\Delta_L]/A(1/\Delta_L) \delta_{LL'}, \\ \tilde{\mathbf{V}} &\equiv \tilde{V}_{LL'}(R - R') = A(1/\Delta_L)^{-1/2} S_{LL'}(R - R') A(1/\Delta_L)^{-1/2} \end{aligned} \quad (6.5)$$

$\mathcal{P}_R = |R\rangle\langle R|$ and $\mathcal{T}_{RR'} = |R\rangle\langle R'|$ are projection and transfer operators in real-space, and L is a composite angular momentum index $\{\ell, m, m_s\}$. C, Δ are the TB-LMTO potential

parameters and S is the structure matrix, in the most tight-binding (α) representation (Andersen 1975). The following functions are :

$$\begin{aligned} A(y) &= x_A y_A + x_B y_B, \quad \text{i.e., the average of } y, \\ B(y) &= (x_B - x_A)(y_A - y_B), \\ F(y) &= \sqrt{x_B x_A}(y_A - y_B), \end{aligned}$$

and

$$|1\rangle = A(\Delta_L^{-1/2})|\{\emptyset\}\rangle + F(\Delta_L^{-1/2})|\{R\}\rangle, \quad |1\rangle = \frac{|1\rangle}{\| |1\rangle \|}.$$

We can reformulate the above in a second quantized formalism. This follows the ideas put forward by Schultz and Shapero 1973, which were extended in the ASF by Mookerjee 1975. For the real-space part, this is straightforward, with a *vacuum* state described as that one which contains no electron-like excitations, and the fermion creation and annihilation operators are a_{RL}^\dagger and a_{RL} for electrons at the site R with angular momentum indices L . For the configuration-space part, we shall follow the ideas of reference Schultz and Shapero 1973 and consider the *reference* state to be the vacuum. Each *spin flip*² at any site from up to down is then a creation of a configuration fluctuation. Since each site can have only two configurations, two up to down *spin flips* cannot take place at a site. These excitations are then *local* and *fermion-like*. Each spin flip from down to up is a destruction of such a *local pseudo-fermion*. The Fock space is then spanned by all configuration states labelled by the cardinality sequences. The corresponding fermion-like creation and annihilation operators are b_R^\dagger and b_R . These create and annihilate configuration fluctuations over the reference state. We should note that the configuration fluctuations are local and quenched. In second quantized form, the Hamiltonian becomes

$$\begin{aligned} \widetilde{\mathbf{H}} &= \widetilde{\mathbf{H}}_0 + \widetilde{\mathbf{H}}_1, \\ \widetilde{\mathbf{H}}_0 &= \sum_{RL} \widetilde{A}_L a_{RL}^\dagger a_{RL} + \sum_{RL} \sum_{R'L'} \widetilde{V}_{RL,R'L'} a_{RL}^\dagger a_{R'L'}, \\ \widetilde{\mathbf{H}}_1 &= \sum_{RL} \left\{ \widetilde{B}_L a_{RL}^\dagger a_{RL} b_R^\dagger b_R + \widetilde{F}_L a_{RL}^\dagger a_{RL} (b_R + b_R^\dagger) \right\}, \end{aligned} \quad (6.6)$$

where

$$\{b_R, b_{R'}^\dagger\} = \delta_{RR'},$$

²These spins denote configurations rather than electron spins.

$$\{b_R, b_{R'}\} = 0 = \{b_R^\dagger, b_{R'}^\dagger\},$$

and the contraction

$$b(x') \cdot b(x)^\dagger = i\theta(t' - t) \delta_{RR'},$$

where

$$b(x) = b_R(t) = \exp(it\tilde{\mathbf{H}}_0) b_R \exp(-it\tilde{\mathbf{H}}_0)$$

so that

$$\begin{aligned} \gamma(x, x') &= -i \langle \{\emptyset\} | \{T b(x') b^\dagger(x)\} | \{\emptyset\} \rangle \\ &= -i\theta(t' - t) \delta_{RR'} \delta(t - t'). \end{aligned} \quad (6.7)$$

This *pseudo-fermion* formalism has been described earlier by Mookerjee (Mookerjee 1975). The readers are referred to that article for further details.

6.4 Averaged Green function in the pseudo-fermion formalism

In this section, we shall develop a multiple scattering formalism for the configuration-averaged Green function for a random binary alloy. The scattering is by configuration fluctuations and within the second-quantized formalism just described, the scattering diagrams are Feynman diagrams. The formalism is very close to the Yonezawa-Matsubara scattering diagrams (Asano and Yonezawa 1980) and one can establish a one-to-one correspondence between them in the special case of diagonal disorder.

The augmented space theorem then states that

$$\ll \mathbf{G}(x, x') \gg = -i \sum_{n=0}^{\infty} \frac{(-i)^n}{n!} \int \dots \int dt_1 dt_2 \dots dt_n \frac{\langle 0 | \{T \tilde{\mathbf{H}}_1(t_1) \dots \tilde{\mathbf{H}}_n(t_n) a(x) a^\dagger(x')\} | 0 \rangle}{\langle 0 | \tilde{\mathbf{S}} | 0 \rangle},$$

where it is understood that the boldface operators are expressed by the matrix representation in $\{L\}$ space and

$$\begin{aligned} a(x) &= a_{RL}(t) = \exp(it\tilde{\mathbf{H}}_0) a_{RL} \exp(-it\tilde{\mathbf{H}}_0), \\ \tilde{\mathbf{S}} &= \tilde{\mathbf{U}}(\infty, -\infty) \quad \text{and} \quad |0\rangle = |0 \otimes \{\emptyset\}\rangle, \end{aligned}$$

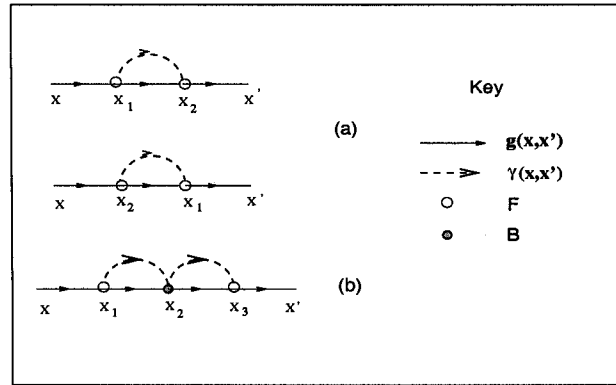


Figure 6.1: The scattering diagrams for (a) the two topologically identical diagrams for $n = 2$ and (b) one of the $3!$ topologically identical diagrams for $n = 3$.

and

$$\tilde{\mathbf{U}}(t, t') = \tilde{\mathbf{I}} - \int_{-\infty}^t dt'' \tilde{\mathbf{H}}_1(t'') \tilde{\mathbf{U}}(t'', t').$$

We may now apply Wick's theorem and Feynman's rules and generate a diagrammatic expansion for the averaged Green function $\ll \mathbf{G}(x, x') \gg$ in terms of the VCA Green function,

$$\mathbf{g}(x, x') = -i \langle 0 | \{ T a(x) a^\dagger(x') \} | 0 \rangle.$$

Let us examine a few terms in the series.

(i) For $n = 1$, the term in the expansion is

$$-i \int dt_1 \langle 0 | \{ T \tilde{\mathbf{H}}_1(t_1) a(x) a^\dagger(x') \} | 0 \rangle_{\text{conn}}.$$

The contribution of this term is zero, since all three terms arising out of $\tilde{\mathbf{H}}_1$ [see equation (6.6)] vanish because $\langle \{ \emptyset \} | b^\dagger(x) b(x) | \{ \emptyset \} \rangle$, $\langle \{ \emptyset \} | b^\dagger(x) | \{ \emptyset \} \rangle$, and $\langle \{ \emptyset \} | b(x) | \{ \emptyset \} \rangle$ are all zero.

(ii) For $n = 2$, the only nonvanishing terms come from

$$i^2 \int dt_1 \int dt_2 \langle 0 | \{ T \tilde{\mathbf{H}}_1(t_1) \tilde{\mathbf{H}}_1(t_2) a(x) a^\dagger(x') \} | 0 \rangle_{\text{conn}}$$

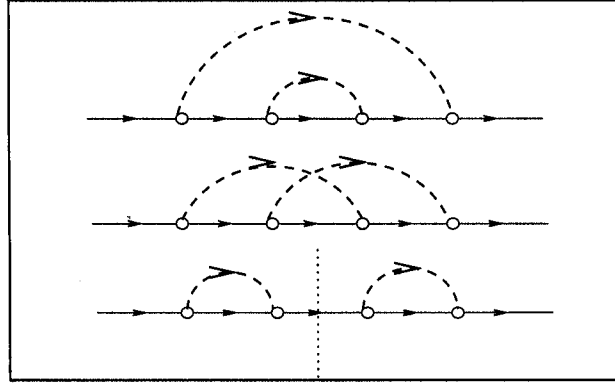


Figure 6.2: The topologically distinct scattering diagrams for $n = 4$. Top and middle are nonseparable, the bottom is separable. The middle diagram is a skeleton one.

$$\begin{aligned}
 &= F^2 \int dx_1 \int dx_2 \langle 0 | \{ T a^\dagger(x_1) a(x_1) a^\dagger(x_2) a(x_2) a(x) a^\dagger(x') \} | 0 \rangle_{\text{conn}} \\
 &\quad \times \langle \{ \emptyset \} | T (b^\dagger(x_1) + b(x_1)) (b^\dagger(x_2) + b(x_2)) | \{ \emptyset \} \rangle_{\text{conn}} \\
 &= F^2 \left[\mathbf{g}(x, x_1) \mathbf{g}(x_1, x_2) \mathbf{g}(x_2, x') \gamma(x_1, x_2) + \mathbf{g}(x, x_2) \mathbf{g}(x_2, x_1) \mathbf{g}(x_1, x') \gamma(x_2, x_1) \right].
 \end{aligned}$$

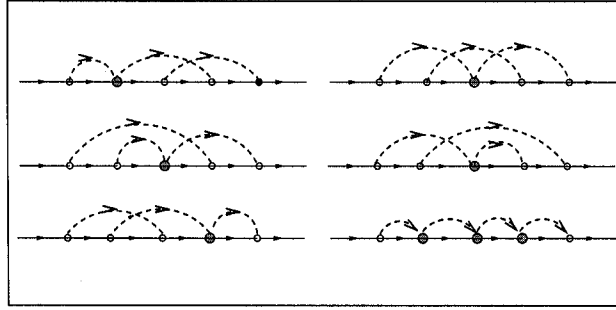
Figure 6.1 (a) shows a pictorial representation of the two terms, which are topologically identical and therefore have identical contributions. This cancels the $(1/2!)$ term in the expansion for $\ll \mathbf{G}(x, x') \gg$. The F vertex [see equation (6.6)] has a contribution $F_{LL'}$ which is diagonal in L space $F_{LL'} = F_L \delta_{LL'}$, where

$$F_L = \sqrt{x_B x_A} \left\langle \frac{1}{\Delta_L} \right\rangle^{-1} \left[\frac{C_L^A}{\Delta_L^A} - \frac{C_L^B}{\Delta_L^B} - z \left(\frac{1}{\Delta_L^A} - \frac{1}{\Delta_L^B} \right) \right].$$

(iii) Figure 6.1 (b) shows one of the topologically identical diagrams (there are $3! = 6$ such diagrams) for $n = 3$. Note that it involves the scattering vertex B . This arises from the first term in the expression for $\widetilde{\mathbf{H}}_1$ in equation (6.6). Its contribution is also diagonal in L space $B_{LL'} = B_L \delta_{LL'}$, where

$$B_L = \frac{(x_B - x_A)}{\sqrt{x_B x_A}} F_L.$$

This scattering vertex cannot sit either in the leftmost or in the rightmost positions, because one of the associated pseudo-fermion propagators vanishes.

Figure 6.3: Skeleton diagrams for order $n = 5$.

- (iv) For $n = 4$, there are two topologically distinct nonseparable diagrams³: the double tent and the crossed tent diagrams shown as the two top diagrams in figure 6.2. The inner tent in the top diagram goes on to renormalize the interior Green function from $\mathbf{g}(x, x')$ to $\ll \mathbf{G}(x, x') \gg$. As such, the middle diagram is the only *skeleton* diagram at this order. There is one separable diagram (the bottom diagram in figure 6.2). This can be broken into two, as shown, by the dotted line. The rightmost diagram renormalizes the rightmost electron line.
- (v) The nonseparable topologically distinct diagrams for $n = 5$ are shown in figure 6.3. We note that all odd-order diagrams must have an odd number of B vertices.

The skeleton diagrams provide the expression for the self-energy for the Dyson equation which follows :

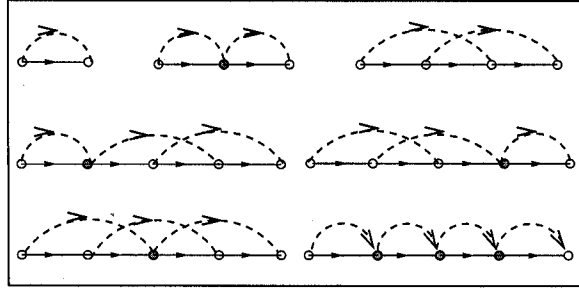
$$\ll \mathbf{G}(x, x') \gg = \mathbf{g}(x, x') + \int dy \int dy' \mathbf{g}(x, y) \boldsymbol{\Sigma}(y, y') \ll \mathbf{G}(y', x') \gg .$$

For homogeneous disorder, we have shown earlier that we have translational symmetry in the full augmented space (Ghosh *et al* 1999). We can then take the Fourier transform of the above equation to get

$$\mathbf{G}(\mathbf{k}, E) = \mathbf{g}(\mathbf{k}, E) + \mathbf{g}(\mathbf{k}, E) \boldsymbol{\Sigma}(\mathbf{k}, E) \mathbf{G}(\mathbf{k}, E). \quad (6.8)$$

The diagrams for the self-energy are shown in figure 6.4. In the above equation, each term is a matrix in $\{L\}$ space.

³A nonseparable diagram cannot be broken into two along a electron line without also breaking a pseudo-fermion line.

Figure 6.4: The skeleton diagrams for the self-energy $\Sigma(z)$.

6.5 Averaged optical conductivity in the pseudo-fermion formalism

We now go back to equation (6.2) and discuss the configuration averaging of the two-particle Green functions of the kind $\mathcal{S}_\gamma(z_1, z_2)$. The augmented space theorem immediately implies that

$$\ll \mathcal{S}_\gamma(z_1, z_2) \gg = \text{Tr} \langle \{\emptyset\} | [\tilde{\mathbf{j}}_\gamma \tilde{\mathbf{G}}^v(z_1) \tilde{\mathbf{j}}_\gamma^\dagger \tilde{\mathbf{G}}^c(z_2)] | \{\emptyset\} \rangle. \quad (6.9)$$

The first thing to note about equation (6.9) is that the right-hand side is an average of four random functions whose fluctuations are correlated. The average of the product then involves the product of the averages and other contributions which come from averages taken in pairs, triplets, and all four random functions.

6.5.1 Disorder-induced renormalization of the current terms

At this stage, in order to simplify notation, we shall omit the L index. However, we have to remember that all terms labelled by indices R or \mathbf{k} are matrices in $\{L\}$ space, so the order of multiplication of various terms in the expression has to be preserved. We shall also omit the γ index of the current term indicating the required projection onto a direction. If required, we can put them back in the final expression.

The real-space representation of the random current operator, can take the values $\mathbf{j}_{RR'}^{\text{AA}}$, $\mathbf{j}_{RR'}^{\text{AB}}$, $\mathbf{j}_{RR'}^{\text{BA}}$, or $\mathbf{j}_{RR'}^{\text{BB}}$ with probabilities x_A^2 , $x_A x_B$, $x_B x_A$, and x_B^2 , respectively. We may

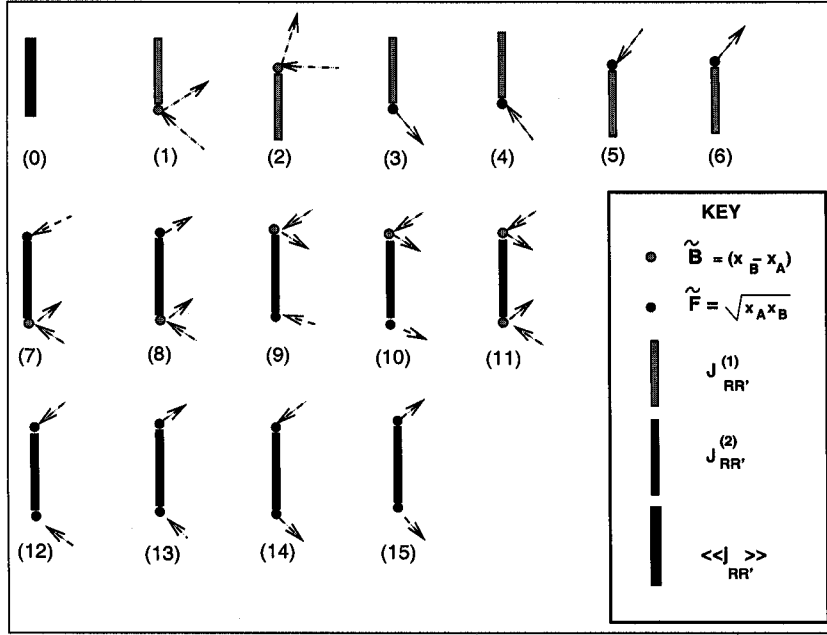


Figure 6.5: The scattering vertices associated with the random current terms.

rewrite $\mathbf{j}_{RR'}$ as

$$\mathbf{j}_{RR'} = \mathbf{j}_{RR'}^{AA} n_R n_{R'} + \mathbf{j}_{RR'}^{AB} n_R (1 - n_{R'}) + \mathbf{j}_{RR'}^{BA} (1 - n_R) n_{R'} + \mathbf{j}_{RR'}^{BB} (1 - n_R)(1 - n_{R'}).$$

Following the same augmented space procedure as for the single-particle Green functions, we get

$$\begin{aligned} \tilde{\mathbf{j}} = \sum_R \sum_{R'} \left[\langle\langle \mathbf{j} \rangle\rangle_{RR'} a_R^\dagger a_{R'} + (x_B - x_A) \mathbf{j}_{RR'}^{(1)} a_R^\dagger a_{R'} (b_R^\dagger b_R + b_{R'}^\dagger b_{R'}) \right. \\ \left. + \sqrt{x_A x_B} \mathbf{j}_{RR'}^{(1)} a_R^\dagger a_{R'} (b_R + b_R^\dagger + b_{R'}^\dagger + b_{R'}) \right. \\ \left. + (x_B - x_A) \sqrt{x_A x_B} \mathbf{j}_{RR'}^{(2)} a_R^\dagger a_{R'} \{ b_R^\dagger b_R (b_{R'}^\dagger + b_{R'}) + b_{R'}^\dagger b_{R'} (b_R^\dagger + b_R) \} \right. \\ \left. + (x_B - x_A)^2 \mathbf{j}_{RR'}^{(2)} a_R^\dagger a_{R'} b_{R'}^\dagger b_{R'} b_R^\dagger b_R + x_A x_B \mathbf{j}_{RR'}^{(2)} a_R^\dagger a_{R'} \{ (b_R^\dagger + b_R) (b_{R'}^\dagger + b_{R'}) \} \right] \end{aligned} \quad (6.10)$$

where

$$\begin{aligned} \mathbf{j}_{RR'}^{(1)} &= x_A (\mathbf{j}_{RR'}^{AA} - \mathbf{j}_{RR'}^{AB}) - x_B (\mathbf{j}_{RR'}^{BB} - \mathbf{j}_{RR'}^{BA}), \\ \mathbf{j}_{RR'}^{(2)} &= \mathbf{j}_{RR'}^{AA} + \mathbf{j}_{RR'}^{BB} - \mathbf{j}_{RR'}^{AB} - \mathbf{j}_{RR'}^{BA} \end{aligned}$$

Figure 6.5 shows 15 different scattering vertices arising from terms in equation (6.10). The first in the figure is the averaged current. The rule for obtaining the diagrams for the correlation function $S_\gamma(z_1, z_2)$ is as follows : Take any two current diagrams from figure 6.5 and two propagators and join them end to end. Now join the configuration fluctuation lines (shown as dashed arrows) in all possible ways. One such diagram is shown in figure 6.6.

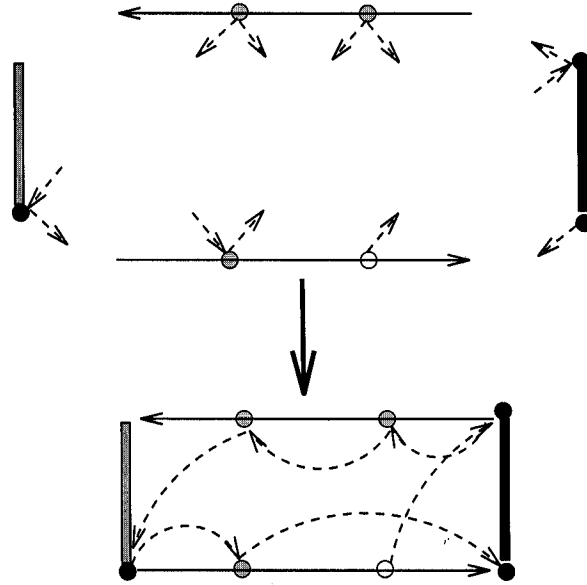
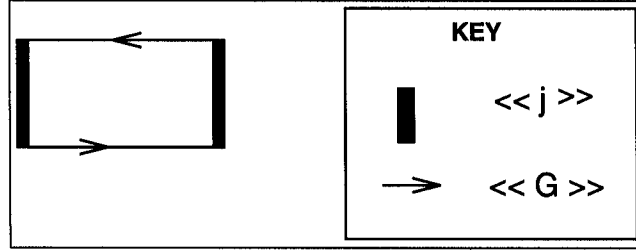


Figure 6.6: The construction of scattering diagrams for $S_\gamma(z_1, z_2)$.

The dominant contribution comes from the diagram shown in figure 6.7. Here the two current terms are the averaged current, and all configuration-fluctuation decorations renormalize only the two electron propagators. In this diagram the bold propagators are the fully renormalized electron propagators and the contribution of this term is

$$\int_{\text{BZ}} \frac{d^3\mathbf{k}}{8\pi^3} \ll \mathbf{j}(\mathbf{k}) \gg \ll \mathbf{G}^v(\mathbf{k}, z_1) \gg \ll \mathbf{j}(\mathbf{k}) \gg^\dagger \ll \mathbf{G}^c(\mathbf{k}, z_2) \gg \quad (6.11)$$

We now focus on the main correction terms to the expression in equation (6.11). These are the correction terms to the averaged current which are closely related to the self-energies. They arise from a set of diagrams in which no disorder propagator (shown as dashed lines) joins either two electron propagators or two of the current lines directly.

Figure 6.7: The diagram for $[\ll j \gg \ll G^v \gg \ll j \gg \ll G^c \gg]$

These diagrams are made out of a left *renormalized* current diagram chosen out of the diagrams (1)-(4) in figure 6.8 and one right *renormalized* current diagram from (5)-(8) connected by two *renormalized* propagators, the bottom one being a valence and the top a conduction electron propagator.

Let us now obtain expressions for the renormalized currents. A careful look at the self-energy diagrams (see the bottom of figure 6.8 and the example diagram shown there) shows that all self-energy diagrams have the structure

$$\Sigma(\mathbf{k}, z) = \mathbf{F}(z) \Phi(\mathbf{k}, z) \mathbf{F}(z)$$

where $\Phi(\mathbf{k}, z)$ is the Fourier transform of $\Phi_{RR'}(z) = \sum_{R_1 R_2} \mathbf{G}_{RR_1}(z) \mathbf{P}_{R_1 R_2}^{RR'}(z) \mathbf{G}_{R_2 R'}(z)$.

While the contribution of the diagram labelled (1) in figure 6.8 is

$$\mathbf{j}^{(1)}(\mathbf{k}) \tilde{\mathbf{F}}(z_1) \Phi(\mathbf{k}, z_1) \mathbf{F}(z_1) \quad (6.12)$$

where

$$F_{LL'}(z) = \sqrt{x_A x_B} \frac{1}{f_L(z)} \delta_{LL'} \quad \tilde{F}_{LL'} = \sqrt{x_A x_B} \delta_{LL'}$$

the expression for (6.12) becomes

$$\mathbf{j}^{(1)}(\mathbf{k}) \tilde{\mathbf{F}}(z_1) \mathbf{F}^{-1}(z_1) \Sigma(\mathbf{k}, z_1) = \mathbf{j}^{(1)}(\mathbf{k}) \mathbf{f}(z_1) \Sigma(\mathbf{k}, z_1).$$

The contributions of the other diagrams in the left column of figure 6.8 are

$$\begin{aligned} \Sigma(\mathbf{k}, z_2) \mathbf{F}^{-1}(z_2) \tilde{\mathbf{F}}(z_2) \mathbf{j}^{(1)}(\mathbf{k}) &= \Sigma(\mathbf{k}, z_2) \mathbf{f}(z_2) \mathbf{j}^{(1)}(\mathbf{k}), \\ \tilde{\mathbf{F}}(z_1) \mathbf{j}^{(1)}(\mathbf{k}) \mathbf{F}^{-1}(z_1) \Sigma(\mathbf{k}, z_1) &= \mathbf{j}^{(1)}(\mathbf{k}) \mathbf{f}(z_1) \Sigma(\mathbf{k}, z_1), \\ \Sigma(\mathbf{k}, z_2) \mathbf{F}^{-1}(z_2) \mathbf{j}^{(1)}(\mathbf{k}) \tilde{\mathbf{F}}(z_2) &= \Sigma(\mathbf{k}, z_2) \mathbf{f}(z_2) \mathbf{j}^{(1)}(\mathbf{k}). \end{aligned}$$

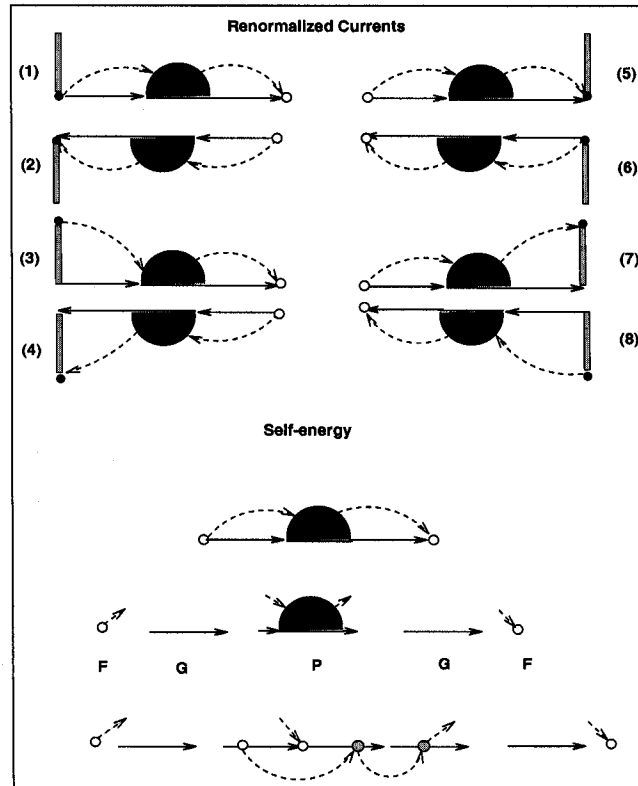


Figure 6.8: Relation between the renormalized currents and the self-energy.

From the forms of $\mathbf{F}(z)$ and $\tilde{\mathbf{F}}(z)$, we note that :

$$\mathbf{j}^{(1)}(\mathbf{k}) \tilde{\mathbf{F}}(z) \mathbf{F}(z) = \tilde{\mathbf{F}}(z) \mathbf{j}^{(1)}(\mathbf{k}) \mathbf{F}(z) = \mathbf{j}_{LL'}^{(1)}(\mathbf{k}) f_{L'}(z).$$

Similarly, the contributions of the diagrams in the right column in figure 6.8 are

$$\begin{aligned} \Sigma(\mathbf{k}, z_1) f(z_1) \mathbf{j}^{(1)}(\mathbf{k}), & \quad \mathbf{j}^{(1)}(\mathbf{k}) f(z_2) \Sigma(\mathbf{k}, z_2), \\ \Sigma(\mathbf{k}, z_1) f(z_1) \mathbf{j}^{(1)}(\mathbf{k}), & \quad \mathbf{j}^{(1)}(\mathbf{k}) f(z_2) \Sigma(\mathbf{k}, z_2). \end{aligned}$$

Closely related to the above diagrams is a group of diagrams which describe joint fluctuations of one current and two propagators. Two such diagrams labelled (9) and (10) in figure 6.9 can also be expressed in terms of the self-energy :

$$\begin{aligned} \Sigma(\mathbf{k}, z_2) f(z_2) \mathbf{j}^{(2)}(\mathbf{k}) f(z_1) \Sigma(\mathbf{k}, z_1), \\ \Sigma(\mathbf{k}, z_1) f(z_1) \mathbf{j}^{(2)}(\mathbf{k}) f(z_2) \Sigma(\mathbf{k}, z_2). \end{aligned}$$

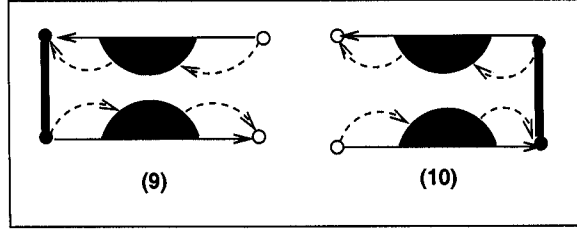


Figure 6.9: Few more renormalized currents.

If we now gather all the contributions from these diagrams, we may define a renormalized current term as follows :

$$\begin{aligned} \mathbf{J}^{\text{eff}}(\mathbf{k}, z_1, z_2) = & \ll \mathbf{j}(\mathbf{k}) \gg + 2 \left[\Sigma(\mathbf{k}, z_2) \mathbf{f}(z_2) \mathbf{j}^{(1)\dagger}(\mathbf{k}) + \mathbf{j}^{(1)\dagger}(\mathbf{k}) \mathbf{f}(z_1) \Sigma(\mathbf{k}, z_1) \right] \\ & + \Sigma(\mathbf{k}, z_2) \mathbf{f}(z_2) \mathbf{j}^{(2)}(\mathbf{k}) \mathbf{f}(z_1) \Sigma(\mathbf{k}, z_1). \end{aligned} \quad (6.13)$$

The contribution of these disorder-renormalized currents and propagators to the correlation function is

$$\begin{aligned} \ll \mathcal{S}_{(1)}(z_1, z_2) \gg = & \\ \int_{\text{BZ}} \frac{d^3\mathbf{k}}{8\pi^3} \text{Tr} \left[\mathbf{J}^{\text{eff}}(\mathbf{k}, z_1, z_2) \ll \mathbf{G}^v(\mathbf{k}, z_1) \gg \mathbf{J}^{\text{eff}}(\mathbf{k}, z_1, z_2)^\dagger \ll \mathbf{G}^c(\mathbf{k}, z_2) \gg \right]. \end{aligned} \quad (6.14)$$

We now turn to terms which involve joint fluctuations between the two current terms and one propagator. We shall show that the corrections due to these terms are also related to the self-energy. Such diagrams are shown in figure 6.10. Contribution of these diagrams is given by

$$\begin{aligned} \ll \mathcal{S}_{(2)}(z_1, z_2) \gg = & 4 \int_{\text{BZ}} \frac{d^3\mathbf{k}}{8\pi^3} \text{Tr} \left[\mathbf{j}^{(1)}(\mathbf{k}) \mathbf{f}(z_1) \Sigma(\mathbf{k}, z_1) \mathbf{f}(z_1) \mathbf{j}^{(1)\dagger}(\mathbf{k}) \ll \mathbf{G}(\mathbf{k}, z_2) \gg \right. \\ & \left. + \mathbf{j}^{(1)\dagger}(\mathbf{k}) \mathbf{f}(z_2) \Sigma(\mathbf{k}, z_2) \mathbf{f}(z_2) \mathbf{j}^{(1)}(\mathbf{k}) \ll \mathbf{G}(\mathbf{k}, z_1) \gg \right] \end{aligned} \quad (6.15)$$

These terms have a slightly different structure than those shown in figure 6.7. However, they still depend only on the self-energy.

Intuitively, we expect these to be the dominant disorder scattering correction to the averaged current. It is important to note that this correction can be obtained from the self-energy and is therefore eminently computationally feasible in the case of realistic alloys, once we have a feasible method for obtaining the self-energy.

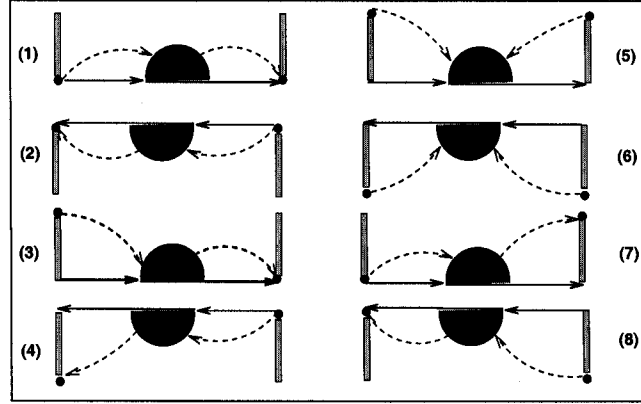


Figure 6.10: The scattering diagrams associated with joint fluctuations of the random current terms and one propagator.

6.5.2 Corrections to the current term related to the vertex corrections

For the sake of completeness, we shall also indicate the contribution of those scattering diagrams to the current which cannot be directly related to the self-energy, but rather to vertex corrections. We expect these corrections to be less dominant.

These diagrams are shown in the left column of figure 6.11. They are not related to the self-energies, but rather to specific vertex correction diagrams between the two propagators. There are three categories of diagrams : ones that involve $\tilde{\mathbf{F}}$ vertices [labelled (11)-(13)], ones that involve $\tilde{\mathbf{B}}$ [labelled (14)-(16)] type vertices and those that involve both [labelled (17)-(18)].

The first category of diagrams (11)-(13) contributes the following :

$$\tilde{\mathbf{F}}(z_1) \mathbf{F}^{-1}(z_1) \mathbf{j}^{(2)}(\mathbf{k}) \tilde{\mathbf{F}}(z_2) \mathbf{F}^{-1}(z_2) \Lambda^{(F)}(\mathbf{0}, \mathbf{k}; z_1, z_2) \Rightarrow \text{diagram (11)},$$

$$\tilde{\mathbf{F}}(z_1) \mathbf{F}^{-1}(z_1) \mathbf{j}^{(2)}(\mathbf{k}) \tilde{\mathbf{F}}(z_2) \mathbf{F}^{-1}(z_2) \Lambda^{(F)}(\mathbf{k}, \mathbf{0}; z_1, z_2) \Rightarrow \text{diagram (12)},$$

$$\tilde{\mathbf{F}}(z_1) \mathbf{F}^{-1}(z_1) \mathbf{j}^{(2)}(\mathbf{k}) \tilde{\mathbf{F}}(z_2) \mathbf{F}^{-1}(z_2) \Lambda^{(F)}(\mathbf{k}, \mathbf{k}; z_1, z_2) \Rightarrow \text{diagram (13)}.$$

Inserting the expressions for $\mathbf{F}(z)$ and $\tilde{\mathbf{F}}$, we get a total contribution,

$$\mathbf{J}_1 = \mathbf{f}(z_1) \mathbf{j}^{(2)}(\mathbf{k}) \mathbf{f}(z_2) \left\{ \Lambda^{(F)}(\mathbf{0}, \mathbf{k}, z_1, z_2) + \Lambda^{(F)}(\mathbf{k}, \mathbf{0}, z_1, z_2) + \Lambda^{(F)}(\mathbf{k}, \mathbf{k}, z_2, z_1) \right\} \quad (6.16)$$

Here, the vertex correction term $\Lambda^{(F)}$ involves only F -like vertices in all four legs. Simi-

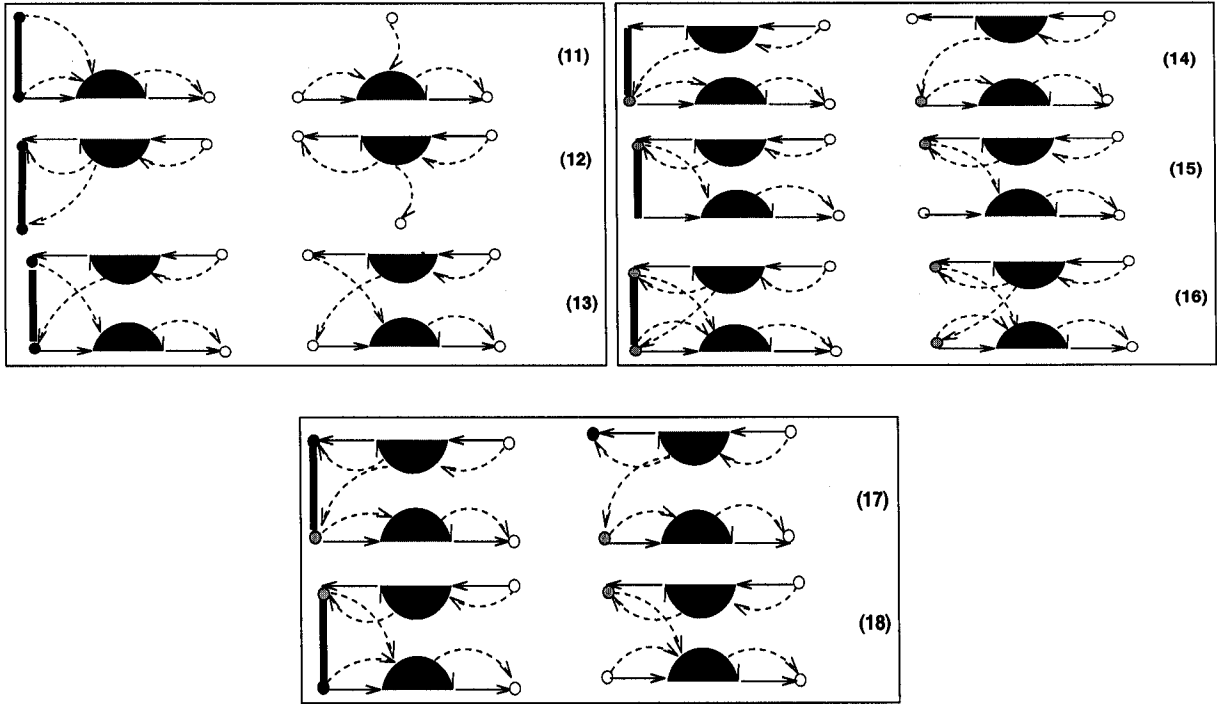


Figure 6.11: Renormalized currents (left column) derived from vertex corrections (right column).

larly, for the other two sets of diagrams we get

$$\begin{aligned}
 \tilde{\mathbf{B}}(z_1) \mathbf{B}^{-1}(z_1) \mathbf{j}^{(1)}(\mathbf{k}) \mathbf{F}^{-1}(z_2) \Lambda^{(B)}(\mathbf{k}, \mathbf{k}; z_1, z_2) &\Rightarrow \text{diagram (14),} \\
 \mathbf{F}^{-1}(z_1) \mathbf{j}^{(2)}(\mathbf{k}) \tilde{\mathbf{B}}(z_2) \mathbf{B}^{-1}(z_2) \Lambda^{(B)}(\mathbf{k}, \mathbf{k}; z_1, z_2) &\Rightarrow \text{diagram (15),} \\
 \tilde{\mathbf{B}}(z_1) \mathbf{B}^{-1}(z_1) \mathbf{j}^{(2)}(\mathbf{k}) \tilde{\mathbf{B}}(z_2) \mathbf{B}^{-1}(z_2) \Lambda^{(B)}(\mathbf{k}, \mathbf{k}; z_1, z_2) &\Rightarrow \text{diagram (16).}
 \end{aligned}$$

The total contribution will be

$$\mathbf{J}_2 = \left\{ \frac{2}{\sqrt{x_A x_B}} \mathbf{f}(z_1) \mathbf{j}^{(1)}(\mathbf{k}) \mathbf{f}(z_2) + \mathbf{f}(z_1) \mathbf{j}^{(2)}(\mathbf{k}) \mathbf{f}(z_2) \right\} \Lambda^{(B)}(\mathbf{k}, \mathbf{k}; z_1, z_2) \quad (6.17)$$

$\Lambda^{(B)}$ involves only B -like vertices in its left-hand side legs. Finally, for the last two diagrams,

$$\begin{aligned}
 \tilde{\mathbf{B}}(z_1) \mathbf{B}^{-1}(z_1) \mathbf{j}^{(2)}(\mathbf{k}) \tilde{\mathbf{F}}(z_2) \mathbf{F}^{-1}(z_2) \Lambda^{(FB)}(\mathbf{k}, \mathbf{k}; z_1, z_2) &\Rightarrow \text{diagram (17),} \\
 \tilde{\mathbf{F}}(z_1) \mathbf{F}^{-1}(z_1) \mathbf{j}^{(2)}(\mathbf{k}) \tilde{\mathbf{B}}(z_2) \mathbf{B}^{-1}(z_2) \Lambda^{(FB)}(\mathbf{k}, \mathbf{k}; z_1, z_2) &\Rightarrow \text{diagram (18).}
 \end{aligned}$$

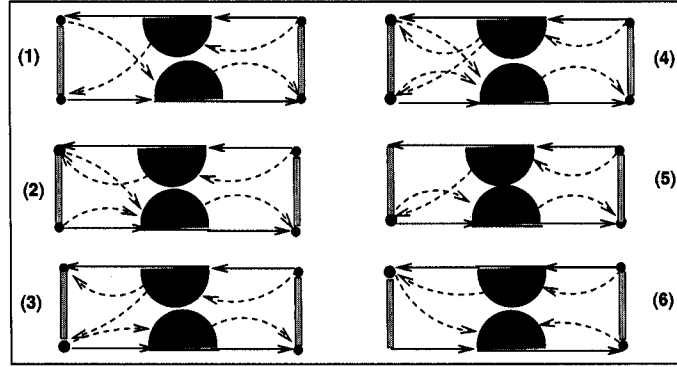


Figure 6.12: Some of the scattering diagrams associated with joint fluctuations of the random current terms and two propagators.

Their contribution is

$$\mathbf{J}_3 = 2 \mathbf{f}(z_1) \mathbf{j}^{(2)}(\mathbf{k}) \mathbf{f}(z_2) \Lambda^{(FB)}(\mathbf{k}, \mathbf{k}; z_1, z_2) \quad (6.18)$$

Collecting together terms

$$\Delta \mathbf{J} = \mathbf{J}_1 + \mathbf{J}_2 + \mathbf{J}_3$$

The contribution of these disorder-renormalized currents and propagators to the correlation function is

$$\begin{aligned} \ll \mathcal{S}_{(3)}(z_1, z_2) \gg = \\ \int_{\text{BZ}} \frac{d^3 \mathbf{k}}{8\pi^3} \text{Tr} \left[\Delta \mathbf{J}(\mathbf{k}, z_1, z_2) \ll \mathbf{G}^v(\mathbf{k}, z_1) \gg \Delta \mathbf{J}(\mathbf{k}, z_1, z_2)^\dagger \ll \mathbf{G}^c(\mathbf{k}, z_2) \gg \right] \end{aligned} \quad (6.19)$$

Finally, figure 6.12 shows the diagrams with joint fluctuations of two current terms and two propagators. These are also built out of vertex corrections. Note that each of the six diagrams can be broken up into a left and right part. For the diagrams shown in figure 6.12 all the right parts are the same. Thirty other similar diagrams can be produced by replacing the right part with the five different left parts mirror-imaged. The contribution of these diagrams is then, if

$$\mathbf{K}(\mathbf{k}, z_1, z_2) = \mathbf{f}(z_2) \mathbf{j}^{(2)}(\mathbf{k}) \mathbf{f}(z_1) + \mathbf{b}(z_2) \mathbf{j}^{(2)}(\mathbf{k}) \mathbf{f}(z_1) + \mathbf{f}(z_2) \mathbf{j}^{(2)}(\mathbf{k}) \mathbf{b}(z_1) + \mathbf{b}(z_2) \mathbf{j}^{(2)}(\mathbf{k}) \mathbf{b}(z_1)$$

where

$$\mathbf{b}(z) = \frac{x_B - x_A}{\sqrt{x_A x_B}} \mathbf{f}(z),$$

$$\ll \mathcal{S}_{(4)}(z_1, z_2) \gg = \int_{\text{BZ}} \frac{d^3\mathbf{k}}{8\pi^3} \text{Tr} \left[\mathbf{K}(\mathbf{k}, z_1, z_2) \otimes \mathbf{K}^\dagger(\mathbf{k}, z_1, z_2) \Lambda(\mathbf{k}, \mathbf{k}, z_1, z_2) \right]. \quad (6.20)$$

6.5.3 The vertex correction

We shall now examine the scattering diagrams we have left out, namely those in which disorder lines connect both the propagators directly. These lead to vertex corrections due to electron-electron and electron-hole correlated propagation. We should note that since these corrections are related to the vertex corrections and we shall indicate how to obtain them within a ladder approximation, we need not sacrifice these terms in a calculation for a realistic alloy if we do not wish to do so. However, in most cases we expect their contribution to be relatively small. Figure 6.13 shows a few of these diagrams. In general, we obtain a Bethe-Salpeter equation for the averaged two-particle propagator. We shall consider only one special class of vertex diagrams in this work, namely the scattering diagrams which are built out of repeated vertices shown on the first line of figure 6.13. These are called the ladder diagrams and can be summed up to all orders. This is the disorder scattering version of the random-phase approximation (RPA) for electron-electron scattering. There is another form of diagrams shown on the second line of figure 6.13 with ladder insertions between the crossed vertices. These are known as maximally crossed diagrams. These diagrams lead to the localization effect.

Here we shall sum the ladder diagrams to all orders. The contribution of the ladder diagram shown as the second diagram on the top line in figure 6.14 is

$$\begin{aligned} & \sum_{R_1 R_2} \sum_{R_3 R_4} \sum_{R_5} \sum_{L_1 L_2} \sum_{L_3 L_4} \sum_{L_5 L_6} J_{R_5 L_6, R_1 L_1}^{\text{eff}} G_{R_1 L_1, R_2 L_2}(z_1) W_{L_2}^{L_5} G_{R_2 L_2, R_3 L_3}(z_1) \\ & \quad \times J_{R_3 L_3, R_4 L_4}^{\text{eff}} G_{R_4 L_4, R_2 L_5}(z_2) G_{R_2 L_5, R_5 L_6}(z_2) \end{aligned}$$

where $G_{RLR'L'}(z) = \ll G_{RLR'L'}^{v/c}(z) \gg$ and

$$W_{L'}^L = F_L(z_2) \left[\delta_{LL'} + 2 \sum_{L''} \left[B_{L''}(z_1) G_{RL'', RL'}(z_1) + B_{L''}(z_2) G_{RL'', RL'}(z_2) \right] \right] F_{L'}(z_1).$$

Homogeneity in augmented space means that this is independent of R and it allows

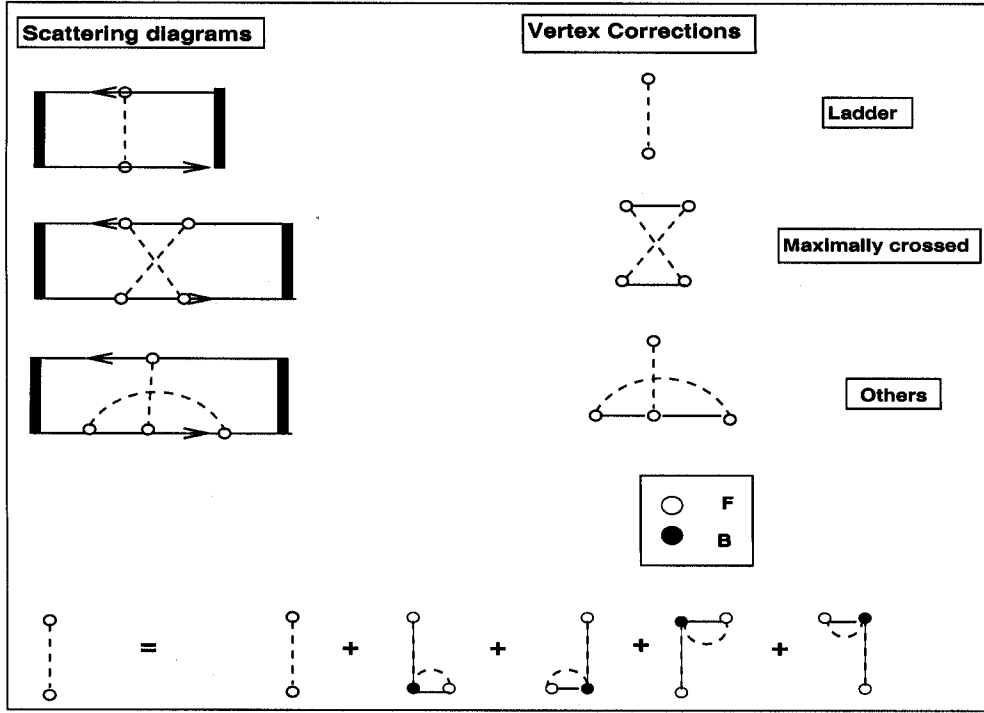


Figure 6.13: The scattering diagrams leading to vertex corrections.

us to take the Fourier transforms leading to

$$\begin{aligned}
 \left[\int_{\text{BZ}} \frac{d^3\mathbf{k}}{8\pi^3} \mathbf{G}(\mathbf{k}, z_2) \mathbf{J}^{\text{eff}}(\mathbf{k}, z_1, z_2) \mathbf{G}(\mathbf{k}, z_1) \right] \mathbf{W} \left[\int_{\text{BZ}} \frac{d^3\mathbf{k}'}{8\pi^3} \mathbf{G}(\mathbf{k}', z_1) \mathbf{J}^{\text{eff}\dagger}(\mathbf{k}', z_1, z_2) \mathbf{G}(\mathbf{k}', z_2) \right] \\
 = \mathbf{\Gamma}(z_1, z_2) \mathbf{W} \hat{\mathbf{\Gamma}}(z_1, z_2)
 \end{aligned} \tag{6.21}$$

We define

$$\begin{aligned}
 \int_{\text{BZ}} \frac{d^3\mathbf{k}}{8\pi^3} \mathbf{G}(\mathbf{k}, z_2) \mathbf{J}^{\text{eff}}(\mathbf{k}, z_1, z_2) \mathbf{G}(\mathbf{k}, z_1) &= \mathbf{\Gamma}(z_1, z_2) \\
 \int_{\text{BZ}} \frac{d^3\mathbf{k}'}{8\pi^3} \mathbf{G}(\mathbf{k}', z_1) \mathbf{J}^{\text{eff}\dagger}(\mathbf{k}', z_1, z_2) \mathbf{G}(\mathbf{k}', z_2) &= \hat{\mathbf{\Gamma}}(z_1, z_2).
 \end{aligned}$$

Let us now look at the contribution of the set of ladder diagrams. Each one of them has the same structure as equation (6.21). We may then sum up the series as follows.

Let us define

$$\lambda_{L_3 L_4}^{L_1 L_2}(z_1, z_2) = \int_{\text{BZ}} \frac{d^3\mathbf{k}}{8\pi^3} G_{L_3 L_4}(\mathbf{k}, z_1) G_{L_2 L_1}(\mathbf{k}, z_2),$$

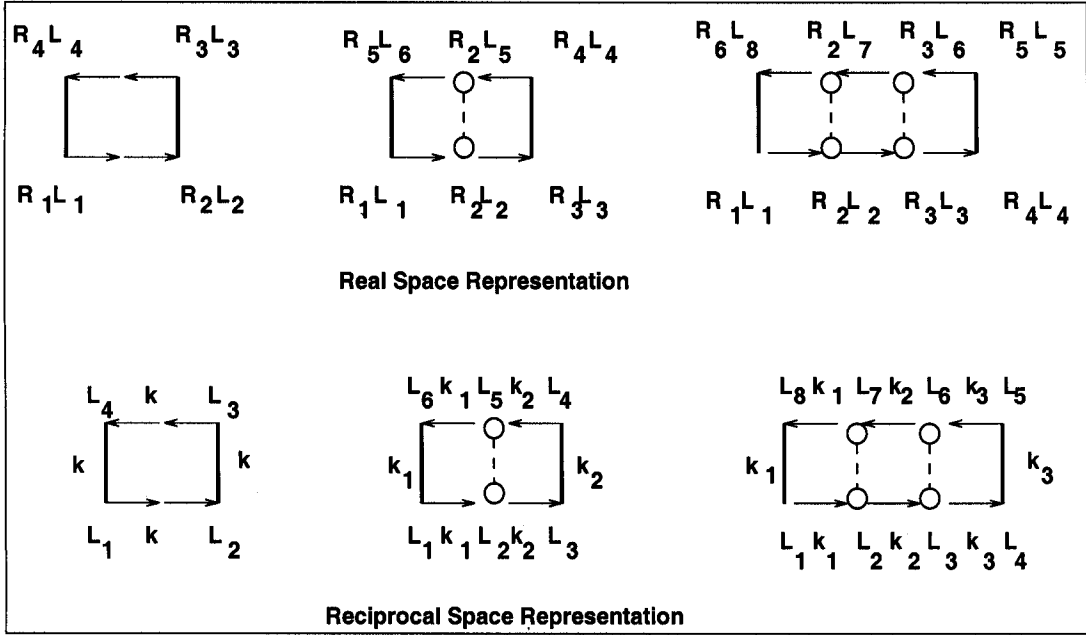


Figure 6.14: The ladder scattering diagrams for the vertex correction in real-space and reciprocal-space representations.

$$\omega_{L_3 L_4}^{L_1 L_2} = W_{L_3}^{L_1} \delta_{L_1 L_2} \delta_{L_3 L_4}.$$

These supermatrices in $\{L\}$ space are written as $\underline{\lambda}$ and $\underline{\omega}$. The full ladder vertex may now be written as

$$\begin{aligned} \underline{\underline{\Lambda}}(z_1, z_2) &= \underline{\omega} + \underline{\omega} \underline{\lambda}(z_1, z_2) \underline{\omega} + \underline{\omega} \underline{\lambda}(z_1, z_2) \underline{\omega} \underline{\lambda}(z_1, z_2) \underline{\omega} + \dots \\ &= \underline{\omega} \left(\underline{I} - \underline{\lambda}(z_1, z_2) \underline{\omega} \right)^{-1} \end{aligned} \quad (6.22)$$

The ladder diagram vertex correction now can be written as

$$\begin{aligned} \ll S_{\text{ladder}}(z_1, z_2) \gg &= \text{Tr} \sum_{L_1 L_2} \sum_{L_3 L_4} \Gamma_{L_2}^{L_1}(z_1, z_2) \Lambda_{L_2 L_4}^{L_1 L_3} \hat{\Gamma}_{L_4}^{L_3}(z_1, z_2) \\ &= \text{Tr} \Gamma(z_1, z_2) \otimes \hat{\Gamma}(z_1, z_2) \Lambda(z_1, z_2). \end{aligned} \quad (6.23)$$

6.5.4 Comments and remarks

Starting from the pseudo-fermion picture in the augmented space method, we have obtained an expression for the configuration-averaged optical conductivity. The disorder

scattering renormalizes both the electron propagators as well as the current terms. We have shown that the dominant corrections to the averaged current can be related to the self-energy. For the sake of completeness, we have also shown that the remaining correction terms are related to the vertex corrections. We have also indicated how to obtain the vertex corrections within the ladder approximation. Once we set up a computationally feasible technique for the computation of the self-energy and the ladder approximation to the vertex correction, all the correction terms can be easily obtained. Biswas *et al* 1997 have suggested the augmented space recursion as a feasible technique for obtaining $\Sigma(\mathbf{k})$ and have applied it for obtaining the complex band structure and density of states of a series of realistic metallic alloys, namely AgPd and AuFe and most recently NiPt (Saha *et al* 2004) among others. We propose to use that technique and the results derived here to obtain the configuration-averaged optical conductivity in disordered metallic alloys. We intend to study, through numerical calculations, the relative importance of the contribution of the different correction terms.

6.6 Applications to CuAu (50-50) and NiPt (50-50) alloys

We shall now apply our methodology to study the optical properties of disordered CuAu and NiPt (50-50) alloys from a first principles approach. We have chosen these two alloy systems because of several reasons : for CuAu, the bunch of d-like states sits about 1 eV below the Fermi level. For low photon energies, therefore, optical conductivity is dominated by the intraband transitions within s-p like states, which are extended and rather free electron-like. As a consequence, the optical conductivity for low photon energies below $\simeq 1$ eV should have a Drude like behaviour. For higher photon energies interband transitions between the occupied d-states and the higher unoccupied states begin to take over. In sharp contrast, the Fermi energy of NiPt almost straddles the d-like peak. For this alloy the Drude behaviour should be confined to a very narrow low photon energy range. This contrasting behaviour should be reflected in our results. Moreover, in both the two alloy systems there is a large size mismatch between the constituents. This indicates that the standard single site mean-field theories would be inadequate to capture the effect of this large size-mismatch.

Table 6.1: Lowest energy and Vegard's Law lattice constants for CuAu and NiPt.

Alloy	Lowest energy lattice const (Å)	Vegard's Law lattice const (Å)
Cu ₅₀ Au ₅₀	7.31	7.26
Ni ₅₀ Pt ₅₀	7.09	7.03

Earlier theoretical work on optical conductivity for random alloys began with Velický 1969 based on the single site coherent potential approximation (CPA) in an empirical tight-binding model alloy. Butler 1985 extended the ideas and combined the CPA with the first-principles Korringa-Kohn-Rostocker (KKR) technique. Banhart 1999 used the KKR-CPA to study the optical conductivity of AgAu alloys. This alloy system has close resemblance to CuAu. Banhart found discrepancies of his theoretical results with experiment (Nielsson 1970, Rivory 1977) and argued that various factors could be responsible : use of the density functional and the single-site mean-field approximations in theory and effects of surfaces, their roughness, possible adsorbates and presence of large stresses in the samples, in the experiments. There have been a few more theoretical studies of optical properties of random alloys : Rhee *et al* 2000 on CoAl, Uba *et al* 2001 on CoPt and Rhee *et al* 2003 on Ni₃Al. These works all base their approach on a large super-cell method to take care of the disorder. The method is brute force and less satisfactory than the CPA or ASR.

We have begun our study with the self-consistent TB-LMTO-ASR calculations of the electronic structure of CuAu and NiPt (50-50) alloys. We have minimized the energy with respect to the variation in the average lattice constant for both the alloys. The table 6.1 shows the lowest energy lattice constants and compares them with the averaged or Vegard's law results. As expected, because of the large size difference between the constituents there is a "bowing" effect which is most prominent at the 50-50 alloys. The lowest energy lattice constant for both the alloys is greater than the Vegard's law predictions.

Figure 6.15 shows the comparison between scaled the joint density of states (JDOS)

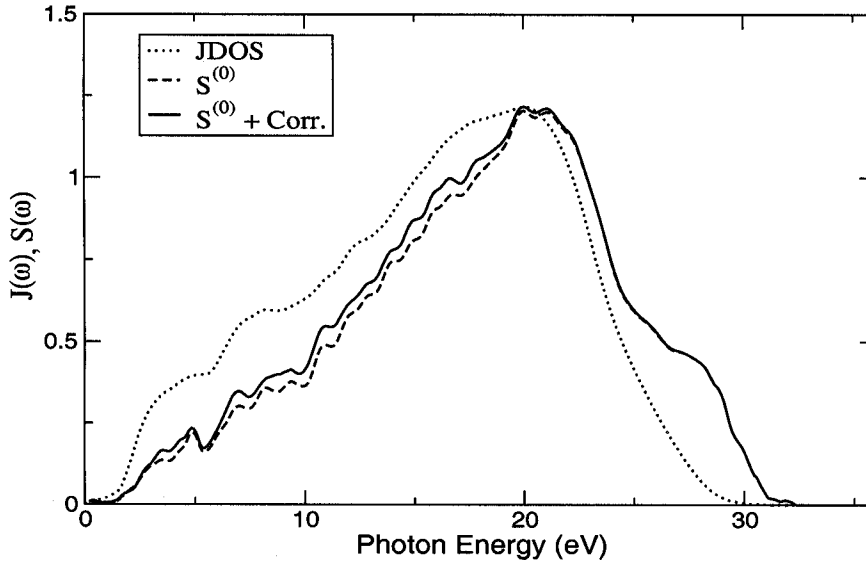


Figure 6.15: The configuration-averaged joint density of states and correlation function for CuAu (50-50) alloy shown as a function of the photon energy.

and the averaged correlation function for a CuAu (50-50) alloy. From the figure it is clear that the transition rate is dependent both on the initial and the final energies, throughout the frequency range of interest. That is :

$$S(\omega) \neq |T|^2 J(\omega)$$

where

$$J(\omega) = \int dE \int \frac{d^3\mathbf{k}}{8\pi^3} \text{Tr} \langle \mathbf{G}^c(\mathbf{k}, E) \mathbf{G}^v(\mathbf{k}, E + \omega) \rangle$$

The figure 6.15 also shows that the disorder corrections to the current and the vertex correction are rather small and become negligible beyond photon energies of the order of 22 eV.

Figure 6.16 to the left shows the optical conductivity $\sigma(\omega)$ for CuAu (50-50) alloy. The inset shows the configuration-averaged density of states for the same alloy. The edge of the d-band complex is clearly seen to lie about 1 eV below the Fermi energy. The optical conductivity rapidly decreases as we increase the photon energy from zero upwards. This decrease continues until about 1 eV and then the conductivity rises again and has considerable structure as also shown in the correlation function for these photon energies (figure 6.15).

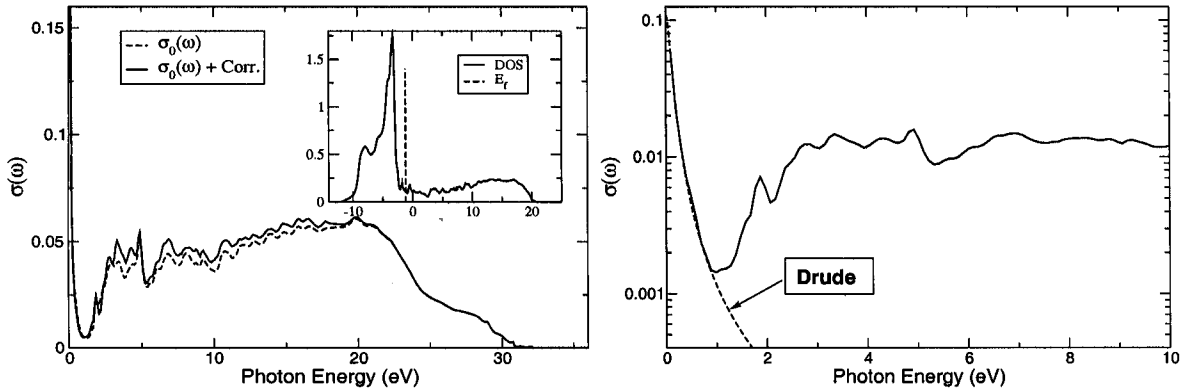


Figure 6.16: Averaged optical conductivity, $\sigma_0(\omega) = S^{(0)}/\omega$, and the density of states for a CuAu (50-50) alloy (left). The corrections to the optical conductivity have been considered as discussed in section 6.5. Same curve with the Drude fit at low photon energies (right).

The right figure 6.16 shows the optical conductivity with a Drude fit [$\sigma^D(\omega) = \sigma(0)/(1 + (\omega\tau)^2)$, with $\sigma(0) = 0.11$, $\tau = 9.78$] for the lower photon energies. The Drude fit is good for photon energies below 1 eV. From this information we may deduce that for low photon energies the conductivity arises due to intraband transition between the s-p states, which are free electron like and lead to a Drude type behaviour. Above 1 eV there is an onset of interband transition between the d and the conduction states and this leads to a sharp increase of optical conductivity and structure reflecting the structures in the d-like states.

The interband contribution to the imaginary part of the dielectric function $\epsilon_2(\omega)$ may be obtained from the optical conductivity data, by subtracting away the Drude contribution and dividing the result by ω : $\epsilon_2(\omega) = (\sigma(\omega) - \sigma^D(\omega))/\omega$. Below the onset of the interband transitions, this quantity vanishes. It then reaches a maximum at around 3 eV before decreasing. We have experimental data on AgAu (50-50) (Nielsson 1970), whose density of states closely resembles CuAu. The experimental data are in good qualitative agreement with figure 6.17. The general shape with a shoulder around 1 eV, a maximum and around 3 eV is clearly reproduced.

The figure 6.18 shows the joint density of states and the averaged correlation function for the NiPt (50-50) alloy. The energy-frequency dependence of the effective transition

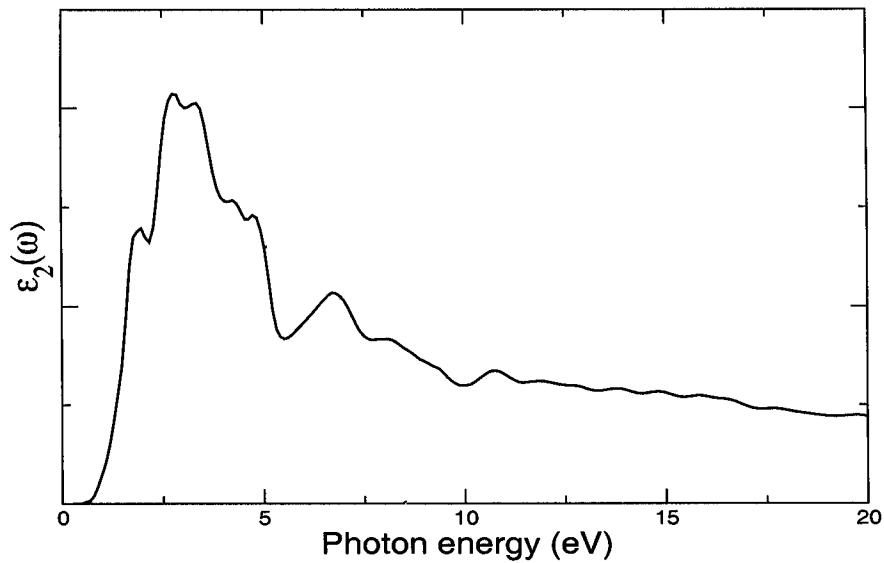


Figure 6.17: Interband contribution to the imaginary part of the dielectric function for CuAu (50-50) alloy.

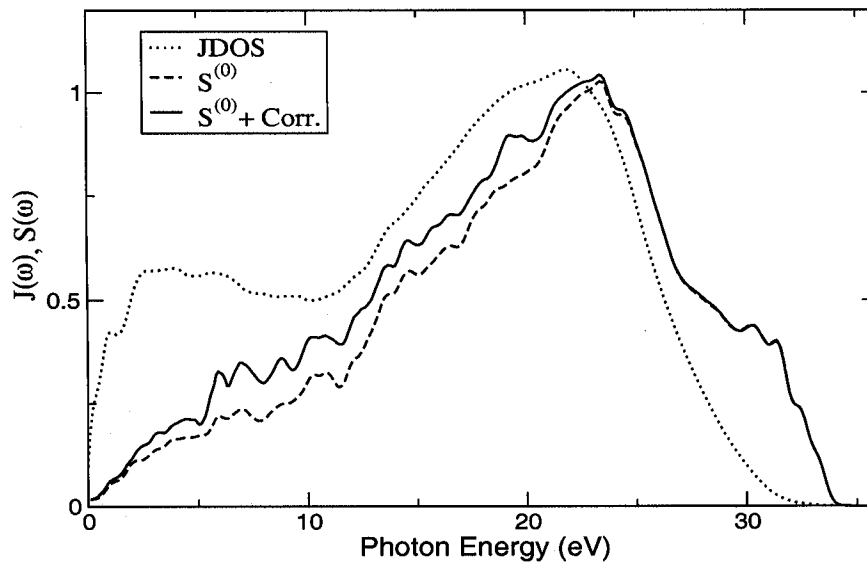


Figure 6.18: The configuration-averaged joint density of states and correlation function for NiPt (50-50) alloy shown as a function of photon energy.

rate is considerably more pronounced than for CuAu. Disorder correction to the current terms and vertex corrections are also more in the low photon energy region. They become negligible for high photon energies.

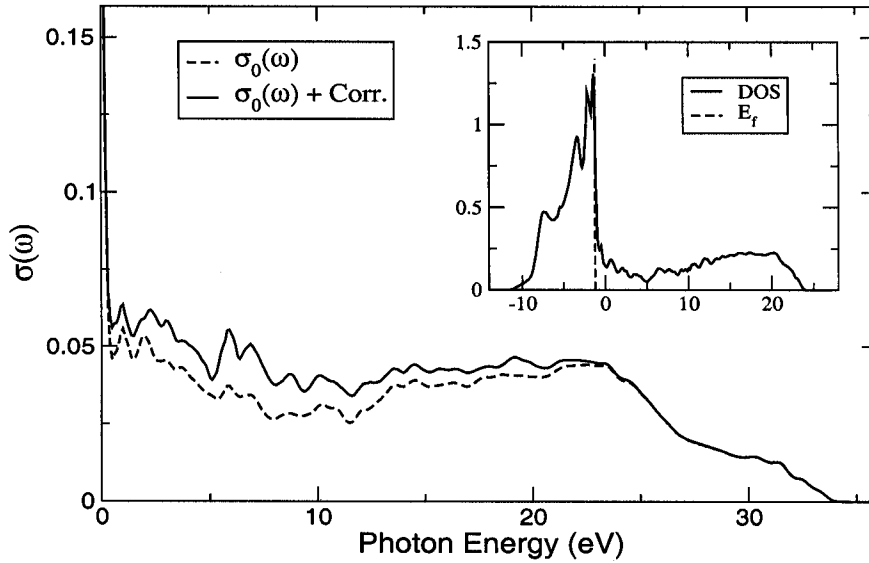


Figure 6.19: Averaged optical conductivity and the density of states for NiPt (50-50) alloy.

Figure 6.19 shows the density of states and the averaged optical conductivity for NiPt. Although the density of states for NiPt qualitatively resembles that for CuAu, unlike the latter, the Fermi level sits right atop the high peak due to the d-like states. The interband transitions between the d-states and the conduction band is expected to start for very small photon energies, with a Drude contribution confined to a very narrow energy range near zero. The optical conductivity falls sharply in a very narrow energy range and recovers almost immediately. This is expected from the density of states picture. Since the Drude fit is in a very narrow range indeed we do not show it explicitly in the figure.

In figure 6.20 we show the interband contribution to imaginary part of the dielectric function for NiPt (50-50) alloy. The interband contribution begins at a very low photon-energy as expected and attains a maximum around 1 eV. This is in contrast to the behaviour of CuAu, where Drude behaviour persists over a longer energy interval. We were unable to locate experimental data for this alloy system for comparison.

6.7 Conclusion

A computationally feasible TB-LMTO-ASR based first principle theory has been presented to study the configuration-averaged optical conductivity in random alloys. We

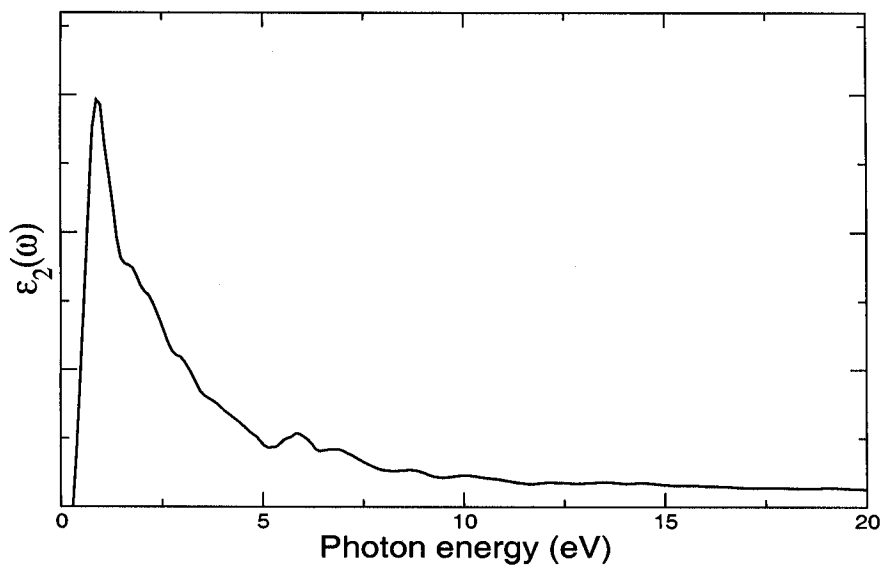


Figure 6.20: Interband contribution to the imaginary part of the dielectric function for NiPt (50-50) alloy.

have shown that the disorder scattering renormalizes the electron and hole propagators as well as the transition amplitudes. The corrections to the transition amplitude have been found to be related to the self-energy of the propagators and the vertex corrections within the ladder approximation. The frequency dependent transport quantities of two disordered metallic alloys have been investigated applying our theory. We have found that the energy-frequency dependence to the effective transition rate is more pronounced for NiPt than that of CuAu. Same tendency was observed in disordered correction to the current terms and vertex corrections in the low photon energy region. We have also found that the conductivity occurs because of both intraband and interband transitions. So the imaginary part of the dielectric function calculated from the conductivity splits into intra and interband contributions. For CuAu the intraband transition takes place up to $\simeq 1$ eV photon energy and in this region the conductivity curve follows Drude law of free electron model. For NiPt alloy the Drude behaviour is confined to a very narrow energy range, as the Fermi energy straddles the d-like peak in density of states. We have compared our results with available theoretical and experimental results and achieved a very impressive agreement with them.

Chapter 7

An assessment and future plans

7.1 Concluding remarks

In this chapter, we shall assess our work : that is, enumerate what was our initial plan of work, assess how much we have completed, indicate what were the limitations of our work and prescribe how to overcome these limitations, and finally lay out our future plan.

Our aim was to systematically develop a theoretical scheme to study optical conductivity of compounds and disordered alloys based on recursion method. We have used TB-LMTO as well as the improved version of the LMTO method (namely NMTO basis) for the ordered calculations and then used ASR to generalize it to disordered systems. In the following, we would like to briefly describe the steps we followed to reach to our goal :

In chapter 2 we have shown that recursion calculations can be carried out much faster and for many more recursive steps exactly, if we perform the recursion on a subspace of the original augmented space reduced by using the symmetries of both the underlying lattice and random configurations on the lattice. This allowed us to obtain results for disordered binary alloys with enhanced accuracy required for first principles, self-consistent, density functional based calculations.

In chapter 3 we have presented ASR formulation in reciprocal-space. In this formulation the real-space part was taken into account *exactly* and there was no truncation of this in the recursion. We found the results to be more accurate than recursion in real-space. We have also shown that the operation of the effective Hamiltonian is entirely in configuration space, which makes the computation easier and faster. However, we failed

to carry out symmetry reduction in this reciprocal-space formulation because we were not confident about the way in which the phase factor $e^{-i\mathbf{k}\cdot\chi}$ (\mathbf{k} is the symmetric \mathbf{k} -point in the Brillouin zone and χ is the real-space nearest neighbour vector) at different symmetric lattice positions changes with symmetry operations. We hope to think more about this in the near future. We have developed parallel codes (MPI programs) for computations in a Beowulf cluster machine.

Since we require the off-diagonal elements of the Green function for our calculations of optical conductivity, we have generalized the recursion to block recursion and block tridiagonalized the Hamiltonian. The generalization has been described (both real and reciprocal-space representation) in detail in chapter 4. The termination procedure used by us is rather brute force. In the termination process we have repeatedly inverted a 9×9 (for spd orbitals) matrix for 10^4 times, which may carry inaccuracies in the calculation. Using a better termination scheme will improve the accuracy of the calculation. This we may think over in nearest future.

We know that the conductivity expression based on traditional reciprocal-space, that is, based on Bloch's theorem, does not work for disorder systems as they do not enjoy potential periodicity. So in chapter 5, we have obtained an alternative expression where the quantum states are directly labeled by energy and frequency, rather than by the 'band' and 'crystal momentum' indices. We have proposed a modified expression for optical conductivity as a convolution of an energy-frequency dependent transition matrix and energy-resolved JDOS. In order to gain confidence in our new formulation we have applied it to the three alkaline-earth titanates, CaTiO_3 , SrTiO_3 and BaTiO_3 in their paraelectric phases. The results were in good agreement with available experimental data, although there were some discrepancies in the high frequency regions. To improve the results mostly in the high frequency regions, we worked within the improved version of the LMTO (namely NMTO basis) and obtained much better results for ZnIn_2Te_4 . The formulation we obtained so far may be the starting point for a many-body GW formulation for random alloys. This we propose for future work.

In chapter 6 we have presented a formulation, based on TB-LMTO-ASR, for the calculation of the configuration-averaged optical conductivity in random alloys. The disorder scattering renormalizes the averaged current to an effective current term and the average

VCA propagator to a configuration-averaged propagator beyond the CPA approximation. We have shown that the corrections to the transition amplitude are related to the self-energy of the propagators and vertex corrections. Finally, we have set up a computationally feasible program and applied to CuAu and NiPt (50-50) alloys. We have shown that the conductivity occurs because of both intraband and interband transitions. The optical conductivity of CuAu for low photon energies below $\simeq 1$ eV have a Drude like behaviour and this is found to be confined to a very narrow energy range in NiPt alloy. For higher photon energies interband transitions between the occupied d states and the higher unoccupied states begin to take over.

7.2 Future directions

The formulation we described so far started from the Kubo-Greenwood expression, which has two Green functions : one for valence and other for conduction bands [See equation (6.9)]. The block recursion has been used to calculate Green matrix elements via termination of continued fractions, which may carry error in the calculations. Moreover, the termination scheme we used in block recursion was not very accurate one. Now the question is how to minimize the approximation in the calculation. Is it possible to have a formulation in such a way which will involve ordinary recursion to be done only once instead of Block recursion for two Green matrices ? This can be done if we start our formulation from Kubo formula instead of Kubo-Greenwood formula. A brief description of the formulation is given in the following :

Our aim is to study correlation function :

$$S_L(\mathbf{k}, t) = \langle \mathbf{k}L | A(t) A^*(0) | \mathbf{k}L \rangle$$

where $\langle \mathbf{k}L | A(t) = \langle \Psi(t) |$ is governed by :

$$-i \frac{\partial}{\partial t} \langle \Psi(t) | = \langle \Psi(t) | H \quad (7.1)$$

The recursion method involves the following steps :

- Expand the wave function : $\langle \Psi(t) | = \sum_{n=0}^{\infty} D_n^*(t) \langle f_n |$

- Choosing initial condition $\langle f_{-1} | = 0$ and $\langle f_0 | = \langle \mathbf{k}L | A$, we generate the orthogonal basis $\{|f_n\rangle\}$ through recursion :

$$\langle f_{n+1} | = \langle f_n | H - a_n \langle f_n | - b_n^2 \langle f_{n-1} |, \quad n = 0, 1, 2, \dots$$

$$\text{where} \quad a_n = \frac{\langle f_n | H | f_n \rangle}{\langle f_n | f_n \rangle} \quad b_n^2 = \frac{\langle f_n | f_n \rangle}{\langle f_{n-1} | f_{n-1} \rangle}$$

- $D_0^*(t) = \langle \Psi(t) | f_0 \rangle = \langle \mathbf{k}L | A(t) A^*(0) | \mathbf{k}L \rangle = S_L(\mathbf{k}, t)$

It will turn out that the sequence $\{a_n, b_n^2\}$ is sufficient for the reconstruction of the dynamical quantities of interest. If we now substitute the orthogonal expansion into the Schrödinger equation (7.1), the differential operator acts on $D_n^*(t)$ and the Hamiltonian acts on the bras $\langle f_n |$. The result is a set of coupled linear differential equations :

$$-i \frac{\partial D_n^*(t)}{\partial t} = D_{n-1}^*(t) + a_n D_n^*(t) + b_{n+1}^2 D_{n+1}^*(t)$$

$$\text{with} \quad D_{-1}^*(t) = 0, \quad D_n^*(0) = \delta_{n,0}$$

Using Laplace transform : $d_n^*(z) = \int_0^\infty dt e^{-izt} D_n^*(t)$,

$$(z - a_n) d_n^*(z) + i\delta_{n,0} = d_{n-1}^*(z) + b_{n+1}^2 d_{n+1}^*(z), \quad n = 0, 1, 2, \dots$$

which leads :

$$d_0^*(z) = \frac{-i}{z - a_0 - \frac{b_1^2}{z - a_1 - \frac{b_2^2}{z - a_2 \dots}}}$$

The Correlation function :

$$\begin{aligned} S(\omega) &= \text{Tr}_L \int_{\text{BZ}} \frac{d^3\mathbf{k}}{8\pi^3} \int_{-\infty}^{\infty} dt e^{-i\omega t} S_L(\mathbf{k}, t) \\ &= 2 \text{Tr}_L \lim_{\delta \rightarrow 0} \int_{\text{BZ}} \frac{d^3\mathbf{k}}{8\pi^3} \Re e [d_{0L}^*(\mathbf{k}, \omega - i\delta)] \end{aligned}$$

Imaginary part of the generalized susceptibility :

$$\chi''(\omega) = \left(\frac{1 - e^{-\beta\hbar\omega}}{2\hbar} \right) S(\omega)$$

For optical conductivity we choose the operator $A(t)$ to be the current operator $j^\mu(t)$ and then carry out the recursion using the initial state :

$$\begin{aligned} j^\mu(0)|\mathbf{k}L\rangle &= q \sum_{\mathbf{R}} e^{i\mathbf{k}\cdot(\mathbf{r}-\mathbf{R})} v^\mu |\psi_L(\mathbf{r}-\mathbf{R})\rangle \\ &= \sum_{\mathbf{R}} e^{i\mathbf{k}\cdot(\mathbf{r}-\mathbf{R})} \sum_{L'} V_{LL'}^\mu |\psi_{L'}(\mathbf{r}-\mathbf{R})\rangle \\ &= \sum_{L'} V_{LL'}^\mu |\mathbf{k}L'\rangle \end{aligned}$$

the matrix element $V_{LL'}^\mu = W_{LL'} G_{LL'}^\mu$ will be calculated using the method given by Hobbs *et al* 1995.

For disorder calculations :

$$\begin{aligned} H &\longrightarrow \tilde{H} \\ j^\mu &\longrightarrow \tilde{j}^\mu \end{aligned}$$

and initial state will be, $\tilde{j}^\mu(0)|\mathbf{k}L \otimes \{\uparrow_1 \uparrow_2 \dots\}\rangle$

7.2.1 Remarks

- In this method one can directly study correlation function.
- This method is more accurate as the recursion is being done only once.
- Studying of optical conductivity always requires a perfect picture of the band structure of solid. But most of the first principle theories fail to give an accurate information about the excited states which can be further improved using many-body GW approximation. This formulation will now form the starting point for a GW formulation.

A Ph.D. programme is always time bound and a person's thirst for knowledge may not find its fulfillment in this limited span of time. But this endeavor elevates his thirst to a higher realm. I do not know how much of knowledge on disorder physics I have been able to pick up. But I sincerely believe that my achievement as well as any limitation of my work will encourage me to go on working and look for a new goal of satisfaction.

Bibliography

- Annett J F, Matthew W, Foulkes C and Haydock R 1994 *J. Phys.: Condens. Matter* **6** 6455.
- Alam A and Mookerjee A 2004 e-print cond-mat/0407512.
- Alouani M, Koch J M and Khan M A 1986 *J. Phys. F: Met. Phys.* **16** 473.
- Alouani M, Brey L and Christensen N E 1988 *Phys. Rev. B* **37** 1167.
- Andersen O K 1971 *Computational Methods in Band Theory*, edited by P M Marcus, J F Janak and A R Williams (Plenum, New York) p. 178.
- Andersen O K 1975 *Phys. Rev. B* **12** 3060.
- Andersen O K and Jepsen O 1984 *Phys. Rev. Lett.* **53** 2571.
- Andersen O K, Jepsen O and Sob 1984 *Electronic Structure of Metals and Alloys* eds. Kumar V, Andersen O K and Mookerjee A (World Scientific).
- Andersen O K, Saha-Dasgupta T, Tank R, Arcangeli C, Jepsen O and Krier G 1998 *Electronic Structure and Physical Properties of Solids* edited by H Dreysse (Springer, Berlin) pp. 3-84.
- Andersen O K and Saha-Dasgupta T 2000 *Phys. Rev. B* **62**, R16219.
- Aulbur W G, Jonsson L and Wilkins J W 2000 *Quasiparticle Calculations in Solids* p. 1-218 in *Solid State Physics* **54** edited by Ehrenrich, H and Spaepen, S (Academic Press).
- Asano S and Yonezawa F 1980 *J. Phys. F: Met. Phys.* **10** 75.
- Banhart J 1999 *Phys. Rev. Lett.* **82** 2139.
- Battaye F L, Hochst H and Goldmann A 1976 *Solid State Commun.* **19** 269.

- Bäuerle D, Braun W, Saile V, Sprussel G and Koch E E 1978 *Z. Phys.*B **29** 179.
- Beer N and Pettifor D G 1982 *The Electronic Structure of Complex Systems*, ed. P Phariseau and W M Temmerman, NATO ASI Series B, v.113, p 769.
- Biswas P, Sanyal B, Fakhruddin M, Halder A, Mookerjee A and Ahmed M 1995 *J. Phys.: Condens. Matter* **7** 8569.
- Biswas P, Sanyal B, Mookerjee A, Huda A, Chowdhury N, Ahmed M and Halder A 1997 *Int. J. Mod. Phys. B* **11** 3703.
- Boltivets N S, Drobyazko V P, and Mityurev V K 1969 *Sov. Phys. Semicond.* **2** 867.
- Bradley C C, Faber T E, Wilson E G and Ziman J M, 1962 *Philos. Mag.* **7** 865.
- Brouers F and Vedyayev A V 1972 *Phys. Rev. B* **5** 348.
- Butler W H 1985 *Phys. Rev. B* **31** 3260.
- Cardona M 1965 *Phys. Rev.* **146** A651.
- Castet-Mejean L 1986 *J. Phys. C: Solid State Phys.* **19** 1637.
- Chakrabarti A and Mookerjee A 2002 *J. Phys.: Condens. Matter* **14** 3211.
- Cohen R E and Krakauer H 1990 *Phys. Rev. B* **42** 6416 ; 1992 *Ferroelectrics* **136** 65.
- Dasgupta I, Saha T and Mookerjee A 1995 *Phys. Rev. B* **51** 3413:
- Dasgupta I, Saha T and Mookerjee A 1997 *J. Phys.: Condens. Matter* **9** 3529.
- Domain C, and Becquart C S 2001 *Phys. Rev. B* **65** 024103.
- Evans R, Greenwood D A and Lloyd P 1980 *Phys. Lett.* **35A** 57.
- Faber T E and Ziman J M 1965 *Philos. Mag.* **11** 153.
- Gelatt C D Jr and Ehrenreich H 1974 *Phys. Rev. B* **10** 398.
- Georgobiani A N, Radautsan S I and Tiginyanu I M 1985 *Sov. Phys. Semicond.* **19**, 121.
- Ghosh S, Das N and Mookerjee A 1999 *Int. J. Mod. Phys. B* **21** 723.
- Godin T J and Haydock R 1988 *Phys. Rev. B* **38** 5237; 1992 *Phys. Rev. B* **46** 1528.
- Hahn H, Frank G, Klingler W, Störger A D, and Störger G 1995 *Z. Anorg. Allg. Chem.* **279** 241.

Harris R and Plischke M 1972 *Solid State Commun.* **11** 1165.

Harrison W A 1989 *Electronic Structure and the Properties of Solids* (Dover, New York) Ch 19.

Harrison W A 1999 *Elementary Electronic Structure* (Singapore: World Scientific) p 546.

Haydock R 1972 *thesis* University of Cambridge, U.K.

Haydock R, Heine V and Kelly M J 1972 *J. Phys. C: Solid State Phys.* **5** 2845.

Haydock R 1980 *Solid State Physics* vol 35 (Academic Press, New York).

Haydock R 1980 *Solid State Phys.* **35** 216.

Haydock R 1981 *Philos. Mag.* B **43** 203.

Haydock R and Te R L 1994 *Phys. Rev. B* **49** 10845.

Haydock R 2000 *Phys. Rev. B* **61** 7953.

Haydock R, Nex C M M and Wexler G 2004 *J. Phys. A: Math. Gen* **37** 161.

Hobbs D, Piparo E, Girlanda R and Monaca M 1995 *J. Phys.: Condens. Matter* **7** 2541.

Hoshino K and Watabe M 1977 *J. Phys. Soc. Jpn.* **43** 583.

Inoue J and Ohta Y 1987 *J. Phys. C: Solid State Phys.* **20** 1947.

Jepsen O and Andersen O K 1971 *Solid State Commun.* **9** 1763.

Kahn A H and Leyendeker A J 1964 *Phys. Rev.* **135** A1321.

Kaplan T and Gray L J 1977 *Phys. Rev. B* **15** 3260.

Kimura S, Yamaguchi Y, Tsukada M and Watanabe S 1995 *Phys. Rev. B* **51** 11049.

King-Smith R D and Vanderbilt D 1992 *Ferroelectrics* **136** 85 ; 1994 *Phys. Rev. B* **49** 5828.

Leath P L 1970 *Phys. Rev. B* **2** 3078.

Lehmann G and Taut M 1972 *phys. stat. sol. (b)* **54** 469.

Levin K and Ehrenreich H 1971 *Phys. Rev. B* **3** 4172.

MacDonald A H, Voskot S H and Coleridge P T 1979 *J. Phys. C: Solid State Phys.* **12** 2991.

- Madelung O 1985 in *Numerical Data and Functional Relationship in Science and Technology*, ed. by O Madelung, Landolt-Börnstein, New Series, **17h** (Springer, Berlin).
- Manca P, Raga F, and Spiga A 1993 *Phys. Status Solidi A* **16** K105.
- Manca P, Raga F, and Spiga A 1974 *Nuovo Cimento B* **19** 15.
- Marin G, Wasim S M, Rincon C, Sanchez Perez G, Power Ch and Mora A E 1998 *J. Appl. Phys.* **83** 3364.
- Mattheiss L F 1972 *Phys. Rev. B* **6** 4718.
- Matsumoto Y, Ozaki S, and Adachi S 1999 *J. Appl. Phys.* **86** 3705.
- Meloni F, Aymerich F, Mula G, and Baldereschi A 1976 *Phys. Acta.* **49** 687.
- Michel-Calandini M and Mesnard G 1971 *Phys. Status Solidi* **44** K117.
- Michel-Calandini M and Mesnard G 1973 *J. Phys. C: Solid State Phys.* **6** 1709.
- Mo S D, Ching W Y, Chisholm M F and Duscher G 1999 *Phys. Rev. B* **60** 2416.
- Mookerjee A 1973 *J. Phys. C: Solid State Phys.* **6** 1340.
- Mookerjee A 1975 *J. Phys. C: Solid State Phys.* **8** 1524.
- Mookerjee A 1976 *J. Phys. C: Solid State Phys.* **9** 1225.
- Mookerjee A, Thakur P K and Yussouff M 1985 *J. Phys. C: Solid State Phys.* **18** 4677.
- Mookerjee A and Thakur P K 1988 *J. Phys. C: Solid State Phys.* **21** 943.
- Mookerjee A and Prasad R 1993 *Phys. Rev. B* **48** 17724.
- Myers S M, Baskes M I, Birnbaum H K, Corbett J W, DeLeo G G, Estreicher S K, Haller E E, Jena P, Johnson N M, Kirhheim R, Pearton S J and Stavola M J 1992 *Rev. Mod. Phys.* **64** 559.
- Nahm T-U, Kim J-Y, Oh S-J, Chung S-M, Park J-H, Allen J W, Jeong K and Kim S 1996 *Phys. Rev. B* **54** 7807.
- Nauciel-Bloch M and Riedinger R 1974 *J. Phys. F: Met. Phys.* **4** 1032.
- Nelson A J, Horner G S, Sinha K and Bode M H 1994 *Appl. Phys. Lett.* **64** 3600.
- Neumann H, Kissinger W, Lévy F, Sobotta H and Riede V 1990 *Cryst. Res. Technol.* **25** 841.

- Neumann H, Kissinger W, and Lévy F 1990 *Cryst. Res. Technol.* **25** 1189.
- Nex C M M 1989 *Comput. Phys. Commun.* **53** 141.
- Nielsson P O 1970 *Phys. Kondens. Matter* **11** 1.
- Niizeki K 1977 *J. Phys. C: Solid State Phys.* **10** 211 ; **10** 2131 ; **10** 2141.
- Niizeki K and Hoshino K 1977 *J. Phys. C: Solid State Phys.* **10** 3351.
- Ozaki S, and Adachi S, 2001 *Phys. Rev. B* **64** 085208.
- Pertosa P and Michel-Calendini F M 1978 *Phys. Rev.* **17** 2011.
- Perkins P G and Winter D M 1983 *J. Phys. C: Solid State Phys.* **16** 3481.
- Pinski F J, Ginatempo J, Johnson D D, Staunton J B, Stocks G M and Gyorffy B L 1991 *Phys. Rev. Lett.* **66** 766.
- Rhee J Y, Kudryavtsev Y V, Kim K W and Lee Y P, *J. Appl. Phys.* 2000 **87** 5887.
- Rhee J Y, Kudryavtsev Y V and Lee Y P 2003 *Phys. Rev. B* **68** 045104.
- Rincon C, Wasim S M, Marin G, Delgado J M, Huntzinger J R, Zwick A and Galibert J 1998 *Appl. Phys. Lett.* **73** 441.
- Rincon C, Wasim S M, Marin G, Hernandez E, Delgado J M and Galibert J 2000 *J. Appl. Phys.* **88** 3439.
- Rincon C, Wasim S M, Marin G 2002 *Appl. Phys. Lett.* **80** 998.
- Rincon C, Wasim S M, Marin G, Delgado J M and Petroff P M 2003 *J. Phys.: Condens. Matter* **15** 3203.
- Rivory J 1977 *Phys. Rev. B* **15** 3119.
- Roth L 1974 *Phys. Rev. B* **9** 2476.
- Roth L and Singh V A 1980 *J. Phys. (Paris), Colloq.* **C8** 459.
- Saha T, Dasgupta I and Mookerjee A 1994 *J. Phys.: Condens. Matter* **6** L245.
- Saha T, Dasgupta I and Mookerjee A 1996 *J. Phys.: Condens. Matter* **8** 1979.
- Saha T and Mookerjee A 1996 *J. Phys.: Condens. Matter* **8** 2915.
- Saha S, Sinha T P and Mookerjee A 2000 *Phys. Rev. B* **62** 8828.

- Saha S, Sinha T P and Mookerjee A 2000 *J. Phys.: Condens. Matter* **12** 3325.
- Saha S, Sinha T P and Mookerjee A 2000 *Eur. Phys. J. B* **18** 207.
- Saha K K, Saha-Dasgupta T, Mookerjee A, Saha S and Sinha T P 2002 *J. Phys.: Condens. Matter* **14** 3849.
- Saha K K and Mookerjee A 2004 *J. Phys.: Condens. Matter* **16** 1409.
- Saha K K and Mookerjee A 2004 *Phys. Rev. B* **70** 134205.
- Saha K K and Mookerjee A 2004 *J. Phys.: Condens. Matter* (accepted for publication) and e-print cond-mat/0409387.
- Saha K K, Mookerjee A and Jepsen O 2004 *Phys. Rev. B* (accepted for publication) and e-print cond-mat/0405175.
- Schmid D, Ruckh M, Grunwald F and Schock H W 1993 *J. Appl. Phys.* **73** 2902.
- Schultz T D and Shapero D 1973 *Phys. Rev. B* **7** 5090.
- Singh D J and Boyer L L 1992 *Ferroelectrics* **136** 95.
- Singh V A and Roth L 1980 *Bull. Am. Phys. Soc.* **25** 242.
- Skriver H L 1984 *The LMTO Method: Muffin Tin Orbitals and Electronic Structure* (New York: Springer).
- Soules T F, Kelly E J, Vaught D M and Richardson J W 1972 *Phys. Rev. B* **6** 1519.
- Uba L, Uba S, Antonov V N, Yarenko A N and Gontarz R 2001 *Phys. Rev. B* **64** 125105.
- Ueda K, Yanagi H, Hosono H and Kawazoe H 1998 *J. Phys.: Condens. Matter* **10** 3669.
- Ueda K, Yanagi H, Hosono H and Kawazoe H 1999 *J. Phys.: Condens. Matter* **11** 3535.
- Uspenski Yu A, Maksimov E G, Rashkeev S N and Mazin I I 1983 *Z. Phys. B* **53** 263.
- Velický B 1969 *Phys. Rev.* **184** 614.
- von Barth U, and Hedin L 1972 *J. Phys. C: Solid State Phys.* **5** 1629.
- Wasim S M, Marin G, Rincón C and Sánchez Pérez G 1998 *J. Appl. Phys.* **84** 5823.
- Wemple S H 1970 *Phys. Rev. B* **2** 2679.
- Wolfram T and Ellialtıoglu S, 1977 *Phys. Rev. B* **15** 5909 ; 1982 *Phys. Rev. B* **25** 2697.

Yang L C, Ziao H Z and Rockett A 1994 *J. Appl. Phys.* **76** 1503.

Zemach R, Ashkenazi J and Ehrenfreund E 1989 *Phys. Rev. B* **39** 1884.

Zemach R, Ashkenazi J and Ehrenfreund E 1989 *Phys. Rev. B* **39** 1891.

Ziman J M 1961 *Philos. Mag.* **6** 1013.

Zook D J and Casselman T M 1975 *Surf Sci* **27** 244.